Tailoring Surface Properties of Fiber Materials: Novel Opportunities in the Fabrication of Multi-scale Fiber-based Architectures

THÈSE N° 7645 (2017)

PRÉSENTÉE LE 28 AVRIL 2017
À LA FACULTÉ DES SCIENCES ET TECHNIQUES DE L'INGÉNIEUR
LABORATOIRE DES FIBRES ET MATÉRIAUX PHOTONIQUES
PROGRAMME DOCTORAL EN SCIENCE ET GÉNIE DES MATÉRIAUX

ÉCOLE POLYTECHNIQUE FÉDÉRALE DE LAUSANNE

POUR L'OBTENTION DU GRADE DE DOCTEUR ÈS SCIENCES

PAR

Dang Tung NGUYEN

acceptée sur proposition du jury:

Dr S. Mischler, président du jury
Prof. F. Sorin, directeur de thèse
Prof. D. Deng, rapporteur
Prof. R. Rossi, rapporteur
Prof. V. Michaud, rapporteuse

ÉCOLE POLYTECHNIQUE
FÉDÉRALE DE LAUSANNE

Suisse
2017

To my family

Acknowledgements

First, I would like to express my deepest gratitude to Professor Fabien Sorin, who has made this adventure possible. Fabien has always been a great mentor since my master project at MIT. His enthusiasm and vision has been the key factors for the realization of this thesis. More than that, Fabien is a great human being whom I am truly happy and honored to know.

I am very grateful to Prof. Véronique Michaud, Prof. Daosheng Deng, Prof. René Rossi and Dr. Stefano Mischler for accepting to be in my thesis committee and for their valuable comments on the work. Prof. Michaud was also the expert in my candidacy exam committee with Dr. Stefano Mischler as president. I am thankful for their availability and guidance on my work during this thesis.

No man is an island, especially during his PhD. For me, this is particularly true during my time at FIMAP, as a member of a new laboratory. This amazing experience, thanks to Fabien, has shown me the importance of stimulating collaborations and fruitful discussions in research; but none of these would be possible without talented and motivated people surrounding me. In FIMAP, I would like to thank Wei Yan and Alexis Page for being always available and collaborative during the whole time working together. I am also thankful to Dr. Arthur Lebris, Dr. Yunpeng Qu and Dr. Tapajyoti Dasgupta, Ms. Chie Kitano and Dr. Federica Sordo for enlarging my knowledge in their respective expertise. It is also a great pleasure to work with Marco Volpi, Nicola Bartolomei, Shahrzad Shadman, Chaoqun Dong, Louis Martin-Monier and Inès Richard. A big thank to Anne Roy, who is always "Swiss" efficient to all problems, and "Swiss" gentle to everyone. It was also a unique opportunity to see a drawing tower being built from scratch, and to discuss with the one who built it, Dr. Peter Prideaux and his wife Phyllis, to whom I would like to express my sincere gratitude. Above all, since day one, FIMAP has been a big family, each and every member has created a unique working environment, which I have enjoyed very much during my PhD.

It is a great chance for me to work at EPFL during her wonderful growth, and in the Department of Materials Science in particular these recent years, according to many of my respected Professors. And this is exactly how I have been feeling since my first day. I am indebted to Prof. Michel Rappaz and his group LSMX for their warm welcome and for helping me to integrate in EPFL-IMX life, and for wonderful friends such as Jean-Luc Desbiolles, Dr. Jean-Marie Drezet, Dr. Emmanuelle Boehm-Courjault, Dr. Nicolas Chobaut. Many of the experiments in this work were done in the old LTC, or the new LPAC, with help of Prof. Véronique Michaud, Prof. Yves Letterier, Rajasundar Chandran, Dr. Tommaso Nardi, Damiano Salvatori, and Dr. Pierre-Etienne Bourban. A special thanks to Raja for his enthusiastic discussions on 3D printing. In addition, I am thankful to the help of Prof. Esther Amstad and her group SMaL, with Gianluca Etienne, Jui-Chia Chang, Antoine Vian, Huachuan Du and others. I especially appreciate the availability and the insight of Prof. Amstad, to whom I am enormously indebted. I would like also to express my gratitude to Prof. Stephanie Lacour and her group ISBN, especially Dr. Alba De Luca, for the fruitful collaboration and bio-experiments on textured fibers. I would like to thank Dr. Stefano Mischler and Dr. Shoufan Cao for the use of the optical profilometer, and to Prof. Michele Ceriotti and COSMO members Piero Gasparotto, Daniele Giofré, Bingqing Cheng, Venkat Kapil etc. for being very nice and pleasant neighbors. In IMX, I also have chance to discuss with many Professors and staff to whom I am truly grateful: Prof. Heinrich Hofmann for accepting in his group in the beginning and for the organization of the Research Day, Prof. Andreas

Abstract

Many surface properties of materials can be tailored by a proper physical patterning. Such patterned surfaces, commonly fabricated by wafer-based techniques, have been widely exploited for light trapping in advanced photovoltaic systems, for tailoring the hydrophobicity of surface, and for enabling the preferential positioning and growth of biological cells. Nevertheless, wafer-based techniques, despite being versatile and mature, are limited to small, flat and rigid Silicon substrates. There is however an increasing demand for micro and even nanoscale patterns to be deployed over large-area and flexible substrates, over fabrics and textiles, or within confined 3D hollow cavities. Other techniques such as roll-to-roll processes bring some solutions but cannot address the patterning of high curvature surfaces that has resisted scientist and engineers for decades. In this thesis, we propose to exploit the emerging field of multi-material thermal drawing to realize submicrometer scale structure on the surfaces of fibers and ribbons. We then go one step further in the assembly of multi-scale functional architectures by using textured fibers as building blocks in novel additive manufacturing processes. At the heart of the project is the fabrication of potentially kilometers-long polymer fibers with controlled hierarchical surface textures of unprecedented complexity and with feature sizes down to a few hundreds of nanometers. To achieve this result, we first establish a theoretical framework to understand the reflow behavior of the structure during the drawing process, which is identified as the reason behind structure collapsing. From this framework, a strategy is developed to reduce the surface/interfacial tension of textured polymers, thus drastically slowing down the reflow, enabling to create for the first time submicrometer textured fibers. These developments are shown in Chapter II, III and IV of this thesis. In addition, the understanding of reflow during the drawing process, in combination with previous work on capillary break-up, allows us to propose an empirical law, presented in Chapter V, to predict the cross-sectional preservation during a preform-to-fiber deformation, the most important feature for the drawing of functional fibers so far. The law is well verified by successful draws of preforms with freely movable domains, based on which we fabricate micro electro-mechanical fiber devices that can detect and localize multiple pressure points along their length with submillimeter resolution. Finally, in Chapter VI we demonstrate the use of multi-material textured fibers as building blocks for the assembly of advanced 2D and 3D functional constructs. We show two examples of microfluidic

devices and of capacitive-touch sensing panels, highlighting the novel opportunities in the scalable nano-scale fabrication of complex devices enabled by the results of this thesis.

Résumé

De nombreuses propriétés de surface des matériaux peuvent être contrôlées par la texturation. Les surfaces texturées, couramment fabriquées par les techniques basées sur le wafer de silicium, apportent de multiples fonctionnalités innovantes, telles que l'amélioration de l'absorption de lumière dans un système photovoltaïque, l'augmentation de l'hydrophobicité des surfaces, ou l'orientation de la croissance des cellules dans la bio-ingénierie. Ces techniques, bien qu'elles soient extrêmement matures et optimisées, sont limitées dans une large part aux substrats de silicium qui sont à la fois petits, plats et rigides. Il est cependant de plus en plus nécessaire que des surfaces micro et même nano-texturées soient fabriquées sur des substrats grands et flexibles, sur des textiles, et même sur les surfaces internes des cavités confinées. D'autres techniques telle que le « roll-to-roll » apportent parfois des solutions mais ne sont pas applicables aux surfaces à grand rayon de courbure. Dans cette thèse, nous proposons d'exploiter la technique émergente de tirage à chaud des fibres multimatériaux comme méthode alternative pour la fabrication de structures à l'échelle micrométrique et nanométrique. De plus, à partir de ces fibres texturées, nous présentons la réalisation d'architectures multi-échelles et fonctionnalisées via l'adaptation de techniques de fabrication additive aux fibres fonctionnelles. Au cœur de ce projet se trouve la fabrication de fibres polymères de plusieurs kilomètres et dont la surface est recouverte par des structures hiérarchisées d'une complexité sans précédent et de dimension aussi fine que quelques centaines de nanomètres. Pour obtenir ces résultats, nous avons d'abord établi un cadre théorique pour comprendre le comportement du phénomène de reflow de la structure au cours du procédé de tirage, qui est identifié comme la raison principale derrière l'aplatissement des structures. A partir de cette description théorique, une stratégie est développée pour réduire la tension de surface et d'interface des polymères texturés, ce qui entraine un ralentissement drastique du reflow, permettant de créer pour la première fois des fibres texturées à une échelle inférieure au micromètre. Ces développements sont présentés dans les chapitres II, III et IV de ce mémoire de thèse. En outre, cette compréhension sur le reflow, en combinaison avec les travaux précédents sur la rupture capillaire, nous permettent de proposer une loi empirique, présentée au chapitre V, pour estimer la préservation de la section efficace de la fibre lors du fibrage. Cette loi est bien vérifiée lors de la réalisation de fibres comprenant des couches minces, qui servent comme capteurs micro-électromécanique de

plusieurs mètres de longueur capables de détecter et localiser de multiples points de pression avec une résolution sous-millimétrique. Enfin, dans le chapitre VI, l'utilisation de fibres texturées pour leur assemblage en des constructions d'architectures fonctionnelles est présentée. Deux exemples sont notamment discutés, la réalisation de dispositifs de microfluidique et de panneaux tactiles à base des fibres. Ceci met en évidence les nouvelles opportunités pour la fabrication de structures complexes et multi-échelles qu'apportent les résultats de cette thèse.

Mots-clés : Tirage à Chaud ; Fibres Multimatériaux ; Larges Surfaces Fonctionnalisées ; Micro et Nano Fabrication ; Textiles Intelligents ; Capteurs de Pression **;** Microfluidique ; Fabrication Additive ; Science et Ingénierie des polymères ; Science et ingénierie des surfaces et interfaces**.**

List of abbreviations

AFM	Atomatic Force Microscopy
ASCs	Adipose-derived stem cells
DRG	Dorsal Root Ganglion
MEMF	Micro Electro-Mechanical Fiber
OM	Optical Microscope
OP	Optical contactless Profiler
PC	Polycarbonate
cPC	Carbon-black filled polycarbonate
PDMS	Polydimethylsiloxane
PE	Polyethylene
cPE	Carbon-black filled polyethylene
PEI	Polyetherimide
PSu	Polysulfone
SEM	Scanning Electronic Microscopy
T_g	Glass transition temperature

Contents

Chapter I.

Introduction

Applied research in Materials Science and Engineering can be understood as an interdisciplinary process based on three pillars: materials, architecture and processing. The Materials pillar consists of the study of intrinsic materials properties – such as mechanical, electrical, thermal properties– and the design of novel materials with the desired attributes. The Architecture pillar explores how materials structure, from the atomic microstructure to the texture at the micrometer scale and beyond, can be exploited to tailor intrinsic properties. Finally, Processing involves the development of novel techniques to manufacture a system from the best material in the right architecture, to deliver the required functionality. The relationship between the three pillars can be represented as shown in Figure I-1.

The development of the thermal drawing process traditionally used for the fabrication of optical fibers, can be mapped very well on the interplay between these three pillars. Originally applied to one type of materials, with a simple architecture and a well-established process, we will show in this thesis that improving the architecture and processing aspects of thermal drawing can lead to novel functional fibers with intriguing properties. To best assess the evolution with respect to the three pillars, they can be presented qualitatively in a three-axis diagram, as shown in Figure I.2 below. The value near the origin in the Materials axis means a limited number of materials identified as compatible with the process, and poor knowledge on their properties. The Architecture axis goes in the direction of improved control over the microstructure as
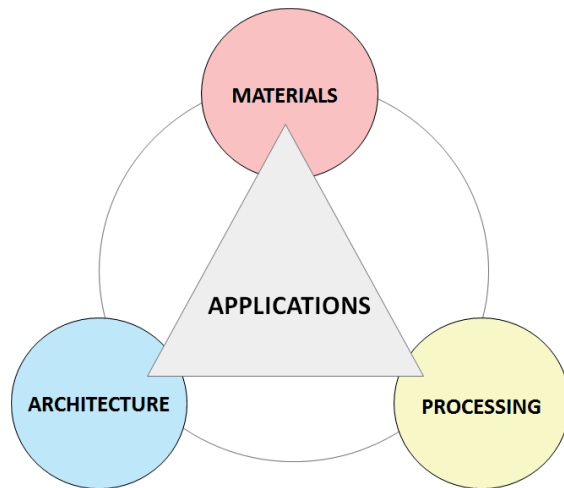
Figure I.1: the three-pillar representation of application-oriented development in Materials Science and Engineering.

well as the shape, scale and achievable morphology. The Processing axis points towards processes that are less expensive, efficient and result in high-quality materials and devices.

In the following paragraphs, after a brief introduction on the thermal drawing technique, we summarize the recent important development in the field by presenting a three-axis evaluation each time a progress was made; and the place where we position the work of this thesis in such diagram.
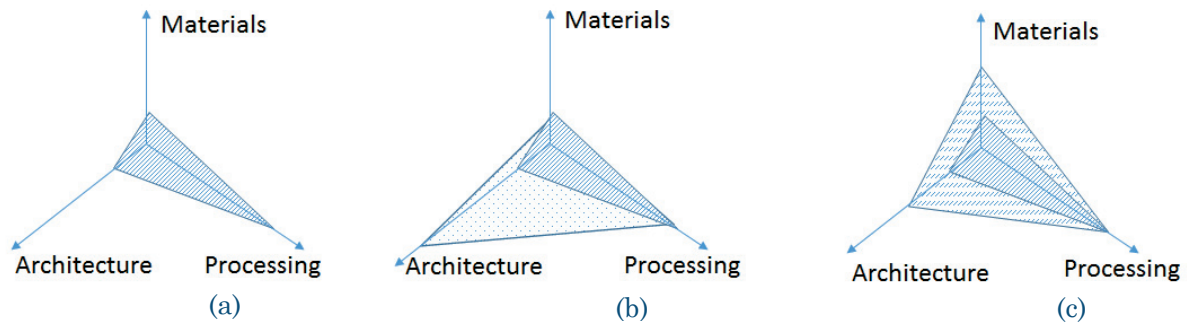
Figure I.2: **Three-axis diagram comparison of techniques to create** (a) first generation of optical fiber (b) photonic-crystal fibers (c) multimaterial fibers.

The thermal drawing technique is a fabrication method that consists of creating a fiber from a glass or polymer preform. The preform is first fed into a closed furnace and is heated above its glass transition temperature. As the viscosity of the material decreases several orders of magnitudes, the preform necks down under its own weight. The lower end of the preform, after coming out of the furnace is rapidly quenched and can be pulled with a constant speed by fixing it to a capstan. Fiber's dimension, shape and internal stress are controlled by a set of drawing parameters, namely down-feed speed (speed at which the perform is fed into the furnace), drawing speed (speed at which the fiber is pulled) and furnace temperature, as explained in Figure I.3. More detailed description of the technique will be given in the Chapter I.

At the beginning, the development of the thermal drawing technique was closely related with the success of optical fibers. Fibers, though being one of the most ancient materials in human history, have remained almost unmodified in term of functionalities for thousands of years. Optical fibers as wave-guide, allowing a large amount of information to be transferred with the speed of light around the globe, were one of the first generation of fibers that massively used outside the conventional textile paradigm. They are today one of the driving forces behind the on-going revolution in telecommunication, starting at the second half of the 20th century [1].

The thermal drawing technique has played a critical role in the widespread of optical fibers, because it enables the fabrication of high-quality waveguides at very large scale and minimum cost; from a single preform, thousands of kilometers of homogeneous fiber could be fabricated in a single draw inside an industrial draw tower. Reciprocally, the drawing technique has benefited from the development of optical fibers and has developed into a subject of intensive research, looking to improve the scaling-down ratio and ease of processing. Nevertheless, because the objective of optical fibers was restricted to low-loss wave guiding, few materials have been employed. The most common is silica, doped and un-doped; polymer-based optical fiber have also been made but only from transparent polymers, from fluoridated polymers to polycarbonate and poly(methyl methacrylate) [2] [3]. The structure of an optical fiber is relatively simple, with a circular cross-section and a step-index architecture that is reproduced homogeneously along its length. In Figure I-2a, the place of this first generation of thermally drawn fiber processes in Materials-Architecture-Processing diagram is represented by a hashed triangle. The values along the Material and Architecture pillars are small because of the few materials used and the simple architectures achieved. The process is however extremely efficient in producing fibers for the desired application.
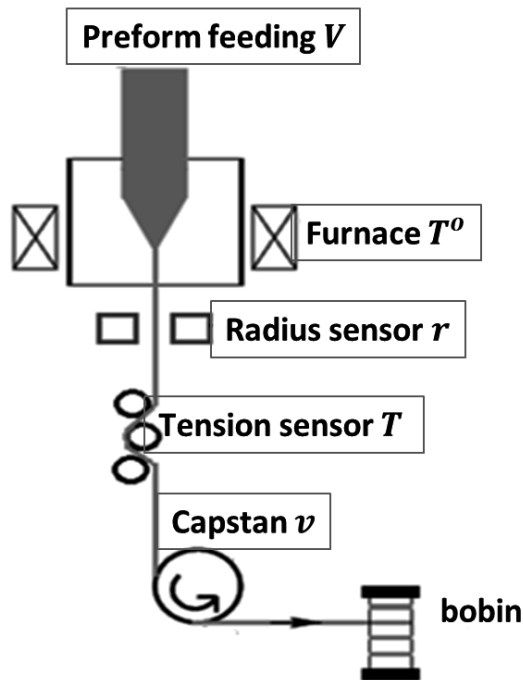
Figure I.3: The schematic of a thermal drawing process.

Recently, new classes of thermally drawn fibers have emerged, taking advantages of the efficient drawing technique. One of them is the photonic-crystal fibers (PCF), first introduced by Prof. Russell and his coworkers in Max Plank Institute, which allow for a novel way of managing the propagation of light. In a PCF, the inner core of the fiber is fabricated with periodic air holes that form a photonic-crystal structure. The size of holes in a PCF are typically of few micrometers, some even can reach 25 nm [4]. The realization of PCFs proved that it is possible to integrate extremely complex structures in fibers using the thermal drawing process. The number of available materials for PCF, however, is still limited to transparent glasses and polymers due to their suitable properties for optical devices. The representation of this generation of fiber in a Materials-Architecture-Processing diagram is shown in Figure I-2b as dotted triangle.

The second class of unconventional fibers is multimaterial fibers, developed mainly at the Massachusetts Institute of Technology (M.I.T) in the group of Prof. Yoel Fink. In this new category of fibers, different materials with disparate thermal and mechanical properties are integrated into a single preform and are thermally co-drawn. The first multimaterial fibers were made by Hart and Temelkuran et al in 2002 [5] [6], which consisted of a 21 alternative bi-layer structure of polymer and chalcogenide glass to create a perfect Bragg mirror inside the fiber core. The next milestone came in 2004 when Bayindir, Sorin and Abbouraddy demonstrated for the first time a Metal-Insulator-Semiconductor structure in fiber [7], and then fabricated a flexible photo-detection fiber device that was sensitive to visible and infra-red light all along its length. A few years later, Sorin and coworkers created a truly functional nanoscale structure in a fiber by integrating 8 photo-detectors in its core [8,9]. The thickness of the semiconducting layers in those thin-film-based photo-detectors were hundreds of nanometers, which increased dramatically the sensitivity of the device. From both Materials and Architecture perspectives, the development of multimaterial fiber generation has extended greatly the frontiers of thermal drawing technique. The M.I.T group went on to invent fibers that acted as heat sensors [10], supercapacitor [11], acoustic sensing [12,13], chemical sensor [14], laser emitting fiber [15,16], etc. We present the multimaterial fiber generation in a Material-Architecture-Processing diagram as in Figure I.2 (c) as the zebra-grilled triangle.

From the examples above, the current development of the fiber field based on the thermal drawing technique can be schematically described using the Material-Architecture-Processing diagram. From a Processing perspective, the improvement comes from modifying the traditional drawing tower, for example, by putting a compressed-air flow to avoid the collapse

of air-hole for PCFs [17,18]. Adding post-drawing steps has also brought additional opportunities and broaden the fabrication approaches, such as using CVD to deposit high quality layers of silicon in an optical fiber core [19,20]; using this technique, fibers with p-n junction or even photo-voltaic structure have been made. Most importantly, the deeper understating developed over the years regarding the physical phenomena at play in the thermal drawing of multi-material assembly has been the main driving force behind expanding the compatible materials and functionalities. In the Materials axis today, a wide variety of materials now is available for thermal drawing, from metals, semiconductors and insulators to piezoelectric micro-domain [12], phase changing materials [21], conducting polymer composite [22] to name a few. Great efforts are currently put in introducing materials with flexibility, biocompatibility or biodegradability in fiber structure. Thermal drawing was also used as a synthesis method, for instance for solid state reaction creating ZnSe from Se and Zn thin-film [23] or making Silicon cores by co-drawing Aluminum in silica fibers [24]. In term of Structure development, other than the device-oriented approach led at M.I.T, there has been an active research direction towards the control of the flow of materials to create micro and nano rods as well as nano and microspheres by exploiting the Taylor-Rayleigh instability [25–27]. The thermal drawing technique becomes a promising fabrication method to make meter-long semiconducting rods, as well as narrowly-disperse nanospheres [28]. In the Materials-Architecture -Processing, those exciting developments in all three axes have truly extended largely the triangle area compared to the initial first-generation of thermally drawn fibers.

Thus far, to realize fibers with innovative functionalities, the field has focused for a large part on the integration of novel materials and structures inside polymers fibers. Surface textures at the micro- and nano-scales are another approach extensively used in materials science to impart materials and devices with improved or novel functionalities. The transfer of this approach to functional fibers has tremendous potential but has been restricted to feature sizes of the order of tens of micrometers, despite intensive efforts in the field. Fundamental limitations associated with fiber processing methods have prevented the integration of small (micrometers and below) surface textures along the fiber length, severely restricting the potential of textured fibers. In this context, the work of this thesis brings novel fundamental understanding to the thermal drawing process, to generate a new class of fibers that get their functionality primarily from their micro- and nano-scale architectures. We hence push further the boundaries of the thermal drawing technique in the Architecture and Processing axis, both

via a deeper scientific understanding of some processes at play during drawing, as well as with the combination of novel fabrication approaches.

More specifically, the important interplay between viscosity and surface tension has been recognized in the fabrication of PCF air holes, or the capillary break-up of embedded thin films or rods inside fibers. Here, we establish a theoretical framework to describe the reflow behavior of surface structures during the drawing process, and demonstrate a novel strategy to design preforms that diminish the reflow effect. This leads, for the first time, to the fabrication of submicrometer patterned fibers that reproduce uniformly along their entire length. In a second time, we also propose an empirical rule to estimate the cross-sectional preservation from the preform to the fiber by considering our reflow deformation framework and the previous work on capillary break-up. We apply this empirical law on the drawing of preforms with freely moving parts as a case study to prove its validity. The obtained fibers constitute the novel Micro Electro-Mechanical Fiber (MEMF) devices, which are used as meters-long multi-touch sensor with submillimeter resolution. Finally, we will further develop an aspect of processing less explored thus far, that patterns to the use of fibers as building block for 2D and 3D functional parts beyond fabrics. This is where the truly nature of the multi-scale aspect of our work is revealed. We demonstrate in particular the fabrication of 3D functional constructs via advanced assembly of textured and multimaterial fibers in microfluidics and in electronic fiber-based system.
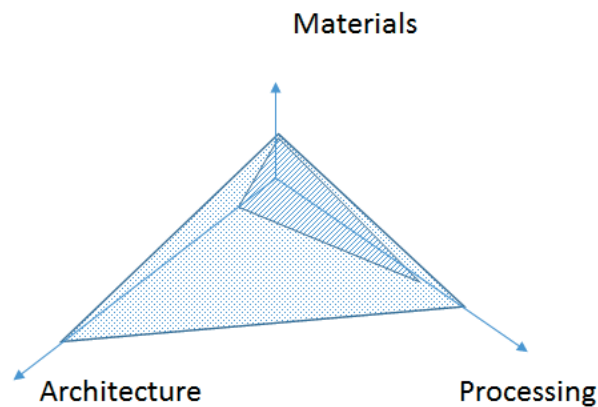
Figure I.4: Schematic the contribution of this thesis work viewed in the Materials-Architecture-Processing diagram.

The thesis is hence organized as follows:

The theoretical and fundamental background onto which this work is based is presented in Chapter II. After emphasizing once again the opportunities that micro- and submicrometer patterned fibers would bring, we describe an analytical development of the preform-to-fiber neck-down deformation using a Navier-Stokes formalism of a Newtonian fluid; and derive a theoretical framework validated by experiments on the thermal reflow of a periodically patterned polymer structure. From these developments, a mathematical description of structure reflow during thermal drawing is presented. The reflow is identified as the fundamental limitation for the fabrication of micro- and nano-structure on fibers' surfaces. During thermal drawing, textured surfaces undergo a thermal reflow driven by the surface tension (Laplace pressure), which can result in the collapse of the surface pattern. Moreover, such reflow happens faster as the pattern size gets smaller. In order to achieve submicrometer patterns size on fiber, as a consequence, we propose a strategy that entails fundamental improvements in terms of preform fabrication and drawing process at the end of this chapter.

The detail of our strategy and its implementation, from preform fabrication to fiber drawing, are presented in Chapter III. It consists of first fabricating the desired structure onto the preform via either mechanical machining or via micro-imprinting. In particular, here we introduce the micro-imprinting as a fast and low cost technique to efficiently create sub-millimeter uniform patterns on the whole preform surface. Subsequently, in order to avoid thermal reflow, we encapsulate the desired texture within a second polymer to properly engineer the surface and interfacial tension, hence enables to achieve submicrometer feature sizes on rectangular ribbons as well as on the outside surface of cylindrical fibers. Such micrometer and submicrometer patterns were also deployed on the inside surface of hollow-core cylindrical fibers, in the way that thermal drawing could be the only efficient approach to realize such structure. The applications of micrometer and submicrometer patterned fibers in surface treatment, in optics and in biology are also demonstrated. These results, illustrated in the Chapter IV, were the subject of a first publication in Advanced Functional Materials [29].

Chapter V deals with the preservation of the cross-sectional structure during a draw. The ability to maintain the architecture design fabricated at the macroscopic scale down to the fiber microscale has been the key feature for the development of functional fibers. Based on the understanding of the reflow and of capillary break-up, we propose a method to estimate the deformation time constant of the cross-section, and hence to estimate the preservation/collapse

of the structure: if the processing time is significantly smaller than this timescale, the cross-section shape would be well preserved from preform to fiber level. This model is well verified with experiments of the drawing of preforms constituted of freely moving polymer thin-films. We also describe briefly in this chapter the features of a novel high resolution cantilever-based touch and pressure sensing fiber, resulting from the draw of such a preform. These result are presented in a Special Issue of the Journal of Physics D: Applied Physics [30].

In Chapter VI, the use of multi-material fibers as building blocks for large-area 2D and 3D constructs is demonstrated. First, flexible and textured fibers are used as templates to fabricate complex microfluidic systems within a PDMS platform. The fiber-template microfluidic device fabrication addresses several challenges encountered by conventional soft-lithography-based approaches, and prove itself as a promising complementary technique to create 3D microfluidic devices with channels of complex structures and shapes. A manuscript is being written on these results. Secondly, we propose the use of a new design of multimaterial fibers for additive manufacturing. In this development, the functionalization and the assembly are decoupled at the fiber level so that the functional part is left intact during the thermal fusion assembly process.

The thesis will be concluded in Chapter VII with discussion on the future development of the work and also of the thermal drawing technique in general, again based on the Materials-Architecture-Processing diagram.

Thermal Drawing for Surface Patterning: Opportunities and Challenges

The use of the thermal drawing technique as a method for surface submicrometer patterning constitutes the main motivation of the thesis. In the first section of this chapter, we discuss the tremendous interest that the technique offers, as well as the difficulties that we need to overcome in order to achieve a truly submicrometer structure. The main obstacle is thermal reflow of the polymer that occurs during the dynamic heating in the drawing process. This phenomenon is examined in the chapter, both theoretically and experimentally. The result obtained in this study not only confirms that reflow is an inherent and severe limitation for the fabrication of micro and nano structures on thermally drawn fiber, and but also brings insight on how to suppress it.

1. Motivation

Micro- and nano-patterns, if appropriately deployed on the surface of materials, can offer unique opportunities for a wide range of applications, from large-scale products such as smart and energy-efficient windows, to specialized devices like artificial tubes for nerve regeneration. However, while the advancement of wafer-based techniques has enabled the fabrication of high quality nanostructures, it remains very challenging to achieve the same level of quality beyond small, flat and rigid Silicon substrates. On the other hand, polymer-based nanoimprinting lithography (NIL) offers a low-cost and effective surface micro/patterning method, especially for roll-to-roll NIL, however, large-scale NIL also comes with complicated set-up and a limited material selection, and cannot be applied on curved surfaces of small radii [31].

The thermal drawing technique represents a promising alternative approach to these conventional methods. As we highlighted in Chapter I, for decades, this simple, low-cost and scalable technique has played an important role behind the success of optical fiber [1] and has become a subject for intensive research. Recently, new generations of thermally drawn fibers

has emerged, such as photonic crystal fibers or multimaterial fibers, that has been described in the previous chapter. With the incorporation of functionalized micro/nanostructured inside the fiber core, fibers now can be deployed in a wide range of applications, from optics [5,6], optoelectronics [7] and chemical sensors [14].

At the moment when this thesis started, surprisingly there had been little interest in deploying structures on the outside surface of the fibers. Nevertheless, thermal drawing is inherently very efficient to generate surface, the total area of a fiber compared to that of the preform is "draw-down ratio" times larger, which is around 20 to 50 in research laboratories, and about 100 to 1000 in a typical industrial procedure. Moreover, the scaling effect that occurs during the drawing hinted a direct 'top-down' fabrication that creates micro- or even nano-scale patterns from a macroscopic easily-machined preform. During the time of the thesis, such direction has been independently developed in different groups [32,33], however, the patterns size has been limited to several tens of micrometers.

The main reason for this limitation is that during the drawing process, the preform is subject to thermal annealing which results in a thermal reflow of the structure, driven by surface tension (Laplace pressure); and the reflow accelerates as the feature size gets smaller (section I.1). Previous work has achieved the functionalization of thermally drawn fibers that integrated patterns but with large sizes, typically around 30 μm, using polyetherimide (PEI), a thermoplastic with a very high mechanical strength that allows a processing at high viscosity that can limit reflow at these dimensions. For many application in optics, opto-electronics, microfluidics, biology or advanced textile however, it is necessary to have smaller – submicrometer – patterns on the surface and within a variety of polymers, which display much weaker mechanical strengths such as polycarbonate (PC), poly(methyl methacrylate) (PMMA), or even soft elastomer such as the widely used poly(dimethyl siloxane) (PDMS).

In the following sections, a mathematical framework of the reflow behavior during thermal drawing process is established, based on the descriptions of the preform-to-fiber evolution and of the reflow on polymer surface under isothermal annealing. From this framework, we propose a strategy to create submicrometer structure on fibers.

2. The Thermal Drawing Technique and Preform-to-Fiber Neck-down Region

Fibers have been among the most important materials in human history. In ancient civilizations, natural fibers such as cotton, silk, wood, were employed as part of textiles, ropes baskets, papers, and so on. The introduction of synthesis fibers in late 19th century was also coincident with the beginning of the modern time. Synthetic fibers not only revolutionized the textile industry but also broadened the application fields for fiber material. Numerous techniques have been employed to create synthetic fibers. Polymer fibers can be manufactured by extrusion, electro-spinning or melt spinning. Such techniques, however, can create mostly single-material fibers, that can only bring functionality after being assembled in some prescribed constructions. Recently, a new approach to create functionalized fiber has been developed using the thermal drawing technique, which then become by far the most popular technique in functionalized-fiber manufacturing. In this section, a technical description of the Thermal Drawing Technique is presented, followed by a mathematical description of the shape along the Preform-to-Fiber neck-down region.

1.1 Technical Description of the Thermal Drawing Technique

As its name suggests, the basic idea of the technique is to draw a macroscopic preform into a long and thin fiber, in most cases without changing its cross-sectional shape. The whole process can be divided into two inter-related steps: preform fabrication and fiber drawing.

A macroscopic preform is made of glassy or polymeric materials. In order to incorporate other materials such as semiconductors, metals, or polymer composites, various techniques have been used early on, for instance preform rolling [34], extrusion [35], or simple mechanical machining [14,22].

Once the preform is made, the fiber drawing can be processed. The preform is placed into an enclosed oven; in general, there are three heating zones in a drawing furnace for a good control of the temperature profile; the first heating zone plays a role of "preheating", the middle zone heats the preform to a temperature over its glass transition temperature, allowing neck-down to occur, and the bottom zone defines the quenching time of the fiber. In the middle zone, the viscosity of the cladding polymer decreases several orders of magnitude, and the preform necks down under its own weight. The lower end of the preform, after coming out and being quenched, is then pulled with a constant speed by a capstan; a high drawing

speed, much superior to preform feeding speed, is the origin of the scaling effect. During the draw, the size of the fiber is measured constantly by a laser sensor, and the pulling tension by a three-wheel sensor. With such measurement, the effective internal stress inside the fiber is hence calculated.
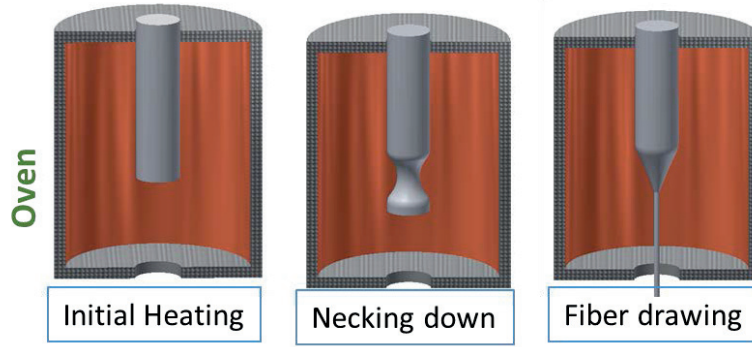
Figure II.2.1: The evolution of a preform during a drawing process, from initial heating through neck-down formation to fiber drawing. Red ring indicates heating zones.

The temperature profile, the feeding speed and drawing speed are the set of parameters that define the shape of the preform-to-fiber neck-down region; and they are also the only parameters directly adjusted in a drawing experiment. The relationship between the preform-to-fiber evolution with those parameters is investigated further in the following section.

1.2   Mathematical Description of the Preform-to-Fiber Neck-down Region

The neck-down region is defined as the zone where the preform starts to deform, shrinking and elongating at the same time, up to the point where the final fiber is shaped. As presented in Figure II.2.2 below, this zone coincides with the heating zone inside the drawing oven where the temperature is above the glass transition temperature of the cladding polymer. The shape of the neck-down region has long been studied [36–39]. The most common analytical approach is to solve the combination of Navier-Stokes equation and constitutive equation with boundary conditions fixed on the free surface of the cladding polymer [36–38] and at the two ends of the neck-down region. This approach will be described later in this section. To achieve the same expression of the preform-to-fiber neck-down region $R(z)$ with $z \in (0, L)$, here we present a much simpler method based on assumptions that are justified perfectly in the experimental conditions of our study. The obtained expression $R(z)$ fits well with an experimental neck-down region of a cylindrical polycarbonate preform drawing.

Our main assumptions are:

i.   The polymer melt is an incompressible and Newtonian fluid.

ii.   The polymer flow is in low Reynold-number, high capillary-number regime

iii.   Compared to the stress generated by the drawing force, the surface tension and gravitational contribution to the shape of the neck-down region is negligible.

Indeed, the first assumption comes from the small flow rate during the draw; the second assumption is verified by the calculation of the Reynold number $Re = \frac{\rho V L}{\eta} \approx 10^{-10}$ and the capillary number $Ca = \frac{\eta V}{\gamma} \approx 10^{4}$; and the third assumption, is justified by comparing the typical drawing stress (in range of 10^{6} Pa) to the Laplace pressure of considering PC fiber γ/R (in range of 10^{2} Pa), and the gravitational contribution $\rho g h$ (in range of 10^{4} Pa). In the steady state, the first assumption leads us to the following equation of a constant flow rate:

$$v_z R^2 = constant$$

<div align="right">[Eq. II.2.1]</div>

with v_z the speed along the z direction, R the radius of the neck-down region at position z.

From the second and the third assumptions, the balance force in a steady flow regime at any position along the z-direction can be written as:

$$F = \sigma_{zz} \pi R^2 = constant$$

<div align="right">[Eq. II.2.2]</div>

with σ_{zz} is the stress tension along the $z-$direction.
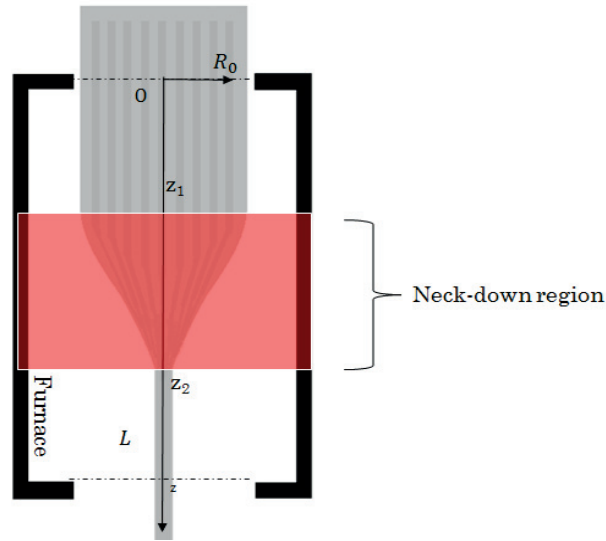
Figure II.2.2: : Schematic of a preform-to-fiber thermal drawing process with the neck-down region is highlighted in red.

Based on the first and the third assumption, the z-direction of the stress tensor can be calculated using Trouton law from the shear viscosity η as:

$$\sigma_{zz} = 3\eta \frac{\partial v_z}{\partial z}$$

[Eq. II.2.3]

Finally, from the three equation [II.1.1] [II.1.2] and [II.1.3], a relation between the velocity along the z-direction and the viscosity profile is deduced:

$$\eta(z) \frac{v'(z)}{v(z)} = constant$$

[Eq. II.2.4]

Considering that the boundary condition at the two ends fixing by the feeding speed V_f and the drawing speed v_d, the velocity profile can be easily obtained from integrating the equation [II.2.4] as following:

$$v(z) = \exp\left(\ln V_f + \frac{\int_0^z \frac{dz}{\eta(z)}}{\int_0^L \frac{dz}{\eta(z)}} \ln \frac{v_d}{V_f} \right)$$

[Eq. II.2.5]

1.3   Experimental Verification

The shape of the neck-down region, $R(z)$, can be easily obtained from the velocity profile $v(z)$ by using [II.2.1] and [II.2.5]. To verify this model, a drawing of a polycarbonate cylindrical preform was conducted.

The dependence of viscosity on temperature of polycarbonate can be expressed according to Arrhenius's law as: $\eta = \eta_{T_0} \exp\left(-\alpha \left(\frac{1}{T+273.15} - \frac{1}{T_0+273.15} \right) \right)$, with T the temperature in degree Celsius ($^o C$). The rheology measurement resulted in the following data: $\alpha^{PC} = 22493$ ($^o C^{-1}$), $T_0 = 200^{oC}$, $\eta_{T_0}^{PC} = 209365$ ($Pa.s$) (conducted with a Rheometer AR2000, TA instrument at the shear rate of $2.5\ s^{-1}$).

The diameter of the preform was $10\ mm$. In such drawing, the preform was fed into the drawing furnace of length $70\ cm$. The temperature of the preform on the surface of the preform was measured with a thermocouple, and could be modeled as a quadratic distribution around the zone where temperature was higher than the glass transition temperature of PC: $T = T_{max} - a\ z^2$, with $T_{max}^{PC} = 190^o C$ (conditioned by the setting temperature of the furnace) at

$z = 0\ cm$, and $a = 14300\ (^oC.m^{-2})$. The considered zone was from $-10\ cm$ to $10\ cm$; outside this zone, the temperature is lower than T_g of PC, hence played negligible role in the shaping of the neck-down region. The feeding speed was fixed at $1\ mm/min$ and the drawing speed was fixed at $100\ mm/min$.

(a)   (b)
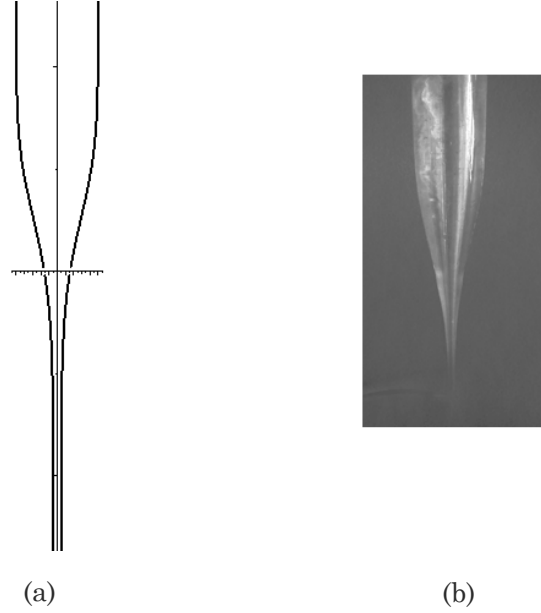
Figure II.2.3: The shape of the neck-down region obtained from (a) simulation and (b) experiment. The vertical dash line in (a) represents the center of the preform, while the vertical line corresponds to the position where $T = T_{max}$.

In Figure II.2.3, an isometric scale graph of the calculated neck-down shape is shown next to a picture of a preform-to-fiber neck-down region obtained experimentally. It can be seen that two shapes match well with each other, which validate our model.

1.4 Formal Mathematical Development

In this section, we derive the equation [II.2.5] from a more formal way based on the Cauchy momentum and constitutive equations with appropriate boundary conditions.

The Cauchy momentum equation in a steady flow is written as:

$$\rho \left(v_r \frac{\partial v_r}{\partial r} + v_z \frac{\partial v_r}{\partial z} \right) = \frac{\partial (\sigma_{rr})}{\partial r} + \frac{\partial \sigma_{zr}}{\partial z} + \frac{\sigma_{rr} - \sigma_{\theta\theta}}{r}$$

[Eq. II.2.6]

$$\rho \left(v_r \frac{\partial v_z}{\partial r} + v_z \frac{\partial v_z}{\partial z} \right) = \frac{\partial \sigma_{zz}}{\partial z} + \frac{1}{r} \frac{\partial (r\sigma_{rz})}{\partial r} + \rho g$$

[Eq. II.2.7]

With σ_{ij} the components of the stress tensor. Since the flow is in low Reynold number, the inertia term on the left-hand side of equations above are neglected; the gravitational is also neglected in a typical draw. In such condition, the z-direction of the equation above becomes:

$$\frac{\partial \sigma_{zz}}{\partial z} + \frac{1}{r} \frac{\partial (r\sigma_{rz})}{\partial r} = 0$$

[Eq. II.2.8]

By multiplying the equation above with rdr and integrating from 0 to R, we get:

$$\int_0^R r \frac{\partial \sigma_{zz}}{\partial z} dr + R\sigma_{rz}(R) = 0$$

[Eq. II.2.9]

In order to express $\sigma_{rz}(R)$, we consider the boundary condition at the free interface of the preform: $\sigma_{ij}.\vec{n} = 0$ with $\vec{n}$ the unit vector of the surface, $\vec{n} = (n_r, n_z) = \left(\frac{1}{(1+R'^2)^{\frac{1}{2}}} , \frac{-R'}{(1+R'^2)^{\frac{1}{2}}} \right)$. Note that the Laplace pressure is negligible.

$$\sigma_{rz}n_r + \sigma_{zz}n_z = 0$$

[Eq. II.2.10]

Or

$$\sigma_{rz}(R) = \sigma_{zz}(R) \, R'$$

[Eq. II.2.11]

Replacing this expression into the integral before, we obtain:

$$\frac{\partial}{\partial z}(R^2 \sigma_{zz}) = 0$$

[Eq. II.2.12]

which is our equation [II.2.2].

The total stress component σ_{ij} can be written as the sum of the thermodynamic pressure p and the viscosity stress τ_{ij} :

$$\sigma_{ij} = -p\delta_{ij} + \tau_{ij}$$

[Eq. II.2.13]

From the constitutive equation, the full form of viscous stress tensor is given as:

$$\bar{\bar{\tau}} = \begin{pmatrix} \tau_{rr} & \tau_{r\theta} & \tau_{rz} \\ \tau_{\theta r} & \tau_{\theta\theta} & \tau_{\theta z} \\ \tau_{zr} & \tau_{z\theta} & \tau_{zz} \end{pmatrix} = \eta \begin{pmatrix} 2\dfrac{\partial v_r}{\partial r} & r\dfrac{\partial}{\partial r}\left(\dfrac{v_\theta}{r}\right) + \dfrac{1}{r}\dfrac{\partial v_r}{\partial \theta} & \dfrac{\partial v_r}{\partial z} + \dfrac{\partial v_z}{\partial r} \\ r\dfrac{\partial}{\partial r}\left(\dfrac{v_\theta}{r}\right) + \dfrac{1}{r}\dfrac{\partial v_r}{\partial \theta} & 2\left(\dfrac{1}{r}\dfrac{\partial v_\theta}{\partial \theta} + \dfrac{v_r}{r}\right) & \dfrac{1}{r}\dfrac{\partial v_z}{\partial \theta} + \dfrac{\partial v_\theta}{\partial z} \\ \dfrac{\partial v_r}{\partial z} + \dfrac{\partial v_z}{\partial r} & \dfrac{1}{r}\dfrac{\partial v_z}{\partial \theta} + \dfrac{\partial v_\theta}{\partial z} & 2\dfrac{\partial v_z}{dz} \end{pmatrix}$$

[Eq. II.2.14]

The symmetry of the system helps to eliminate the terms $\tau_{r\theta}$ and $\tau_{z\theta}$. The viscous stress tensor is simplified as:

$$\bar{\bar{\tau}} = \eta \begin{pmatrix} 2\dfrac{\partial v_r}{\partial r} & 0 & \dfrac{\partial v_r}{\partial z} + \dfrac{\partial v_z}{\partial r} \\ 0 & 2\dfrac{v_r}{r} & 0 \\ \dfrac{\partial v_r}{\partial z} + \dfrac{\partial v_z}{\partial r} & 0 & 2\dfrac{\partial v_z}{dz} \end{pmatrix}$$

[Eq. II.2.15]

The continuity equation gives us the link between the velocity components in the r-direction and the z-direction:

$$\frac{1}{r}\frac{\partial(rv_r)}{\partial r} + \frac{\partial v_z}{\partial z} = 0$$

[Eq. II.2.16]

Integrating the equation above from 0 to r we get:

$$v_r = -\frac{1}{2}r\frac{\partial v_z}{\partial z}$$

[Eq. II.2.17]

We can rewrite the total tensor as:

$$\bar{\bar{\sigma}} = \begin{pmatrix} -p - \eta\dfrac{\partial v_z}{\partial z} & 0 & \tau_{rz} \\ 0 & -p - \eta\dfrac{\partial v_z}{\partial z} & 0 \\ \tau_{rz} & 0 & -p + 2\eta\dfrac{\partial v_z}{\partial z} \end{pmatrix}$$

[Eq. II.2.18]

Since the flow is in a high capillary number regime, the surface tension contribution is negligible, then $\sigma_{rr} = \sigma_{\theta\theta} \approx 0$, which gives:

$$\sigma_{zz} = 3\eta\frac{\partial v_z}{\partial z}$$

[Eq. II.2.19]

The equation below is well-known under the name of Trouton law with extensional viscosity $\eta_e = 3\eta$, which is also our equation [II.2.3]

The last piece needed to finish the puzzle is finding the relation between the speed component v_z and the diameter R. Such relation is called the constant flow rate in a steady flow, our equation [II.2.1].

$$v_z R^2 = constant$$

[Eq. II.2.20]

We have come to the same system of equations as in the previous section. Although an identical result is obtained, this approach starts with a full description of the system, as well as explicit boundary conditions; then approximations are made along the way to reach a simplified equation; whereas in previous subsection, the assumptions are considered immediately at the beginning, which could be less rigorous for some readers. However, a simplified description could be useful for readers who are not fully familiar with fluid mechanics, because it is only based on the intuitive volume conservation, a force balance, and the less trivial Trouton law.

1.5   Discussion on the Flow Field

All approaches mentioned above accept some assumptions that are not completely satisfied under strict considerations. One of which is the assumption that the temperature of a cross-section is uniform on Oxy plan; or $\frac{\partial T(r,\theta,z)}{\partial r} = 0$ and $\frac{\partial T(r,\theta,z)}{\partial \theta} = 0$. The approximation allows us to construct a shape of the preform-to-fiber matching well with experiment (Figure II.2.3).

However, in order to create a more precise model, a non-uniform velocity flow inside the fiber along the z-direction should be taken into account. The construction of a simple flow field entirely analytically would give us more insight on the shear stress at each point of the preform-to-fiber, hence to deeper understanding of the related properties such as alignment of polymer chains or the filler distribution for polymer nanocomposites.

In simulation, a strategy to find the temperature distribution is to include the thermal term into the energy balance equation [40]. However, it is not easy to verify experimentally such simulation, because it is extremely difficult to measure in-situ the temperature at each point in the preform during a draw. Any method using thermocouple would change the temperature profile, whereas an infra-red camera could only give the information of the temperature of the surface emission. As a consequence, the only way to verify the exactitude of such simulation is to compare the shape of the preform-to-fiber region. We believe, however, that if a reflow field can be constructed from the temperature profile, then measuring the electrical conductivity profile of a preform made of conducting polymer composites would give indirectly information about the temperature profile. The impact of this calculation does not just limit to a better understanding of the process, but it could immediately pave the way to important development in the field of multimaterial fiber drawing, for instance a controlled way of creating conducting and transparent composite layers in a fiber.

3. Reflow of Polymer Surface Under Isothermal Annealing

Reflow is the phenomenon in which the roughness of a polymer surface, mostly intentionally created as an ordered pattern, is smoothen out under annealing. The driving force of reflow is the minimization of surface area, and the counter deformation terms are inertia and viscosity. The reflow behavior of a structure material has been studied previously in different contexts, either to prevent such deformation [41], or to use the reflow to reduce surface roughness [42], or even to take advantage of it to create active structure such as micro-lenses [43].

In this subsection, a mathematical description of the reflow on polymer surface is presented. We consider the reflow of a sinusoidal surface with a single harmonic mode; then we extend such description to any periodical structure using Fourier transformation. It is noted that all considered surface structures are periodic only in one direction, and infinite in the other one (1D structure).

Let us consider the surface with a 1D sinusoidal structure, with the structure period being λ and the amplitude being h (Figure II.3.1). The depth d of the material is much larger than the period and the amplitude. The surface wave takes the following form:

$$y = h\cos\left(\frac{2\pi}{\lambda}x\right)$$

<div align="right">[Eq. II.3.1]</div>
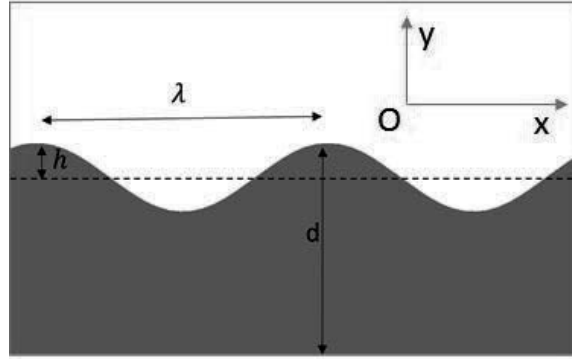
Figure II.3.1: A schematic of a sinusoidal polymer surface with surface wavelength λ, amplitude h and the bulk thickness d.

At the speed of deformation, the polymer can be considered as incompressible. As a consequence, the continuity equation is given as:

$$\nabla\vec{u} = \vec{0}$$

<div align="right">[Eq. II.3.2]</div>

where u is the flow velocity.

At the same time, at low Reynolds number, the flow is irrotational, therefore the velocity field needs to satisfy following equation:

$$\nabla\times\vec{u} = \vec{0}$$

<div align="right">[Eq. II.3.3]</div>

The equation [II.3.3] implies that there exists a scalar potential ϕ so that $v = \nabla\phi$. Considering the equation [II.3.2], this potential need to satisfy the Laplace equation:

$$\nabla^2\phi = 0$$

<div align="right">[Eq. II.3.4]</div>

By defining $u^s = \frac{\partial h}{\partial t}$, the following velocity potential and velocity field beneath the surface fulfills equation [II.3.2] and [II.3.3]:

$$\phi(x, y) = u^s \exp\left(\frac{2\pi}{\lambda} y\right) \cos\left(\frac{2\pi}{\lambda} x\right)$$

$$\vec{u}(x, y) = \sin\left(\frac{2\pi}{\lambda} x\right) \exp\left(\frac{2\pi}{\lambda} y\right) u^s \, \hat{x} + \cos\left(\frac{2\pi}{\lambda} x\right) \exp\left(\frac{2\pi}{\lambda} y\right) u^s \, \hat{y}$$

[Eq. II.3.5]

Note that y takes negative values in the expression [II.3.4], corresponding to a decay of the velocity field inside the bulk with a characteristic length of $2\pi/\lambda$.

The velocity field in the equation results in a shear stress tensor, following a constitutive equation given by:

$$\bar{\bar{\tau}} = \eta \begin{pmatrix} 2\dfrac{\partial v_x}{\partial x} & \dfrac{\partial v_x}{\partial y} + \dfrac{\partial v_y}{\partial x} \\ \dfrac{\partial v_x}{\partial y} + \dfrac{\partial v_y}{\partial x} & 2\dfrac{\partial v_y}{\partial y} \end{pmatrix}$$

[Eq. II.3.6]

In the equation above, η is the viscosity of the material, and is a constant for a Newtonian fluid, independent of the stress. A polymer can be considered as a Newtonian fluid when the shear rate is small, such as in our case.

We now consider the boundary condition at the surface:

$$\bar{\bar{\sigma}} \cdot \hat{n} = \gamma \kappa \, \hat{n}$$

[Eq. II.3.7]

where the total stress $\bar{\bar{\sigma}} = -p \, \bar{\bar{I}} + \bar{\bar{\tau}}$ is equal to the Laplace pressure $p^s = \gamma \kappa$. In considered regime, neglecting the external pressure and the gravitational force, the internal pressure p is zero everywhere underneath the surface. Hence, at the surface, the total stress becomes:

$$\sigma_{yy}^s = -2\eta \frac{2\pi}{\lambda} u^s = -\frac{4\eta\pi}{\lambda} \frac{\partial h}{\partial t}$$

[Eq. II.3.8]

In the right term of the equation II.3.6, κ is the surface curvature and is given by:

$$\kappa = \frac{\dfrac{d^2 y}{dx^2}}{\left[1 + \left(\dfrac{dy}{dx}\right)^2\right]^{-\frac{3}{2}}}$$

[Eq. II.3.9]

The unit vector of the surface $\hat{n} = (n_x, n_y)$ is composed of the following components:

$$n_x = -\frac{\frac{\partial y}{\partial x}}{\left[1 + \left(\frac{dy}{dx}\right)^2\right]^{-\frac{3}{2}}}$$

[Eq. II.3.10]

$$n_y = -\frac{1}{\left[1 + \left(\frac{dy}{dx}\right)^2\right]^{-\frac{3}{2}}}$$

[Eq. II.3.11]

We now consider that the curve has a relatively small slope everywhere, which results in $\frac{\partial y}{\partial x} \ll 1$, and the variation along the y-direction can be neglected. We will evaluate the validity of this approximation in the discussion section.

With such approximation, the right hand side of equation [II.3.6] at the surface is $\gamma\kappa = \gamma\frac{\partial^2 y}{\partial x^2} = \gamma h \left(\frac{2\pi}{\lambda}\right)^2$. The equation [II.3.6] is rewritten as:

$$-\frac{4\eta\pi}{\lambda}\frac{\partial h}{\partial t} = \gamma\, h \left(\frac{2\pi}{\lambda}\right)^2$$

[Eq. II.3.12]

Or:

$$\frac{\partial h}{\partial t} = -\frac{\pi\gamma}{\eta\lambda}\, h$$

[Eq. II.3.13]

The amplitude of the surface wave is the solution of the equation above, which is:

$$h(t) = h_{t=0} \exp\left(-\frac{\pi\gamma}{\eta\lambda}\, t\right)$$

[Eq. II.3.14]

The equation 2.6 describes the evolution of the amplitude of a surface wave over time. The wavelength of such wave is a constant since at the position $y = 0$ the curvature is zero, corresponding to a null driving force of the deformation.

We consider again the boundary condition [II.2.6]; which can be written explicitly under the considered regime as:

$$-\frac{4\eta\pi}{\lambda}\frac{\partial y}{\partial t} = \gamma\frac{\partial^2 y}{\partial x^2}$$

[Eq. II.3.15]

22

The equation [II.3.14] above that describes the surface wave is linear, hence can be expressed as a Fourier series. In consequence, we are able to decompose a surface wave of arbitrary shape into harmonic modes; moreover, the temporal evolution of the sum of all modes at any instant t gives the temporal evolution of the surface wave. For instance, let us consider the surface with a square wave $y(x, t)$ of period λ and amplitude h, and its Fourier term $y^n(x, t)$:

$$y(x, t) = \sum_{n=0}^{N} y^n(x, t)$$

[Eq. II.3.16]

Figure II.3.2 shows a period of such square wave and its Fourier series with N varying from 1 to 10. As the sum reaches the higher harmonic order, the shape of Fourier transform gets closer to the initial function. The Fourier series for a square wave is written as:

$$y(x, 0) = \sum_{n=1}^{N} \frac{4}{(2n - 1)} h(0) \cos\left((2n - 1)\frac{2\pi}{\lambda} x\right)$$

[Eq. II.3.17]
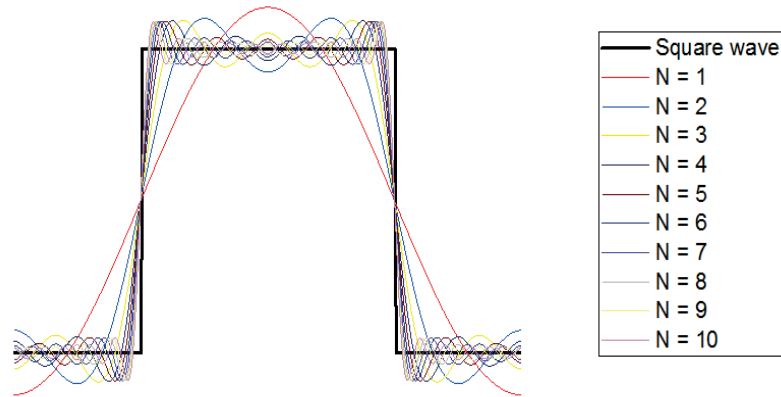
Figure II.3.2: A square wave and its Fourier series with progressive N

With the temporal evolution of each harmonic mode in equation [II.2.16], the temporal evolution of the square wave can be described as the following function:

$$h(t) = \sum_{n=1}^{N} \frac{4}{(2n - 1)} h(0) \exp\left(-(2n - 1)\frac{\pi\gamma}{\eta\lambda} t\right)$$
$$= \sum_{n=1}^{N} \frac{4}{(2n - 1)} h(0) \exp\left(-(2n - 1)\frac{t}{\tau}\right)$$

[Eq. II.3.18]

In this equation, a characteristic time is defined as following:

$$\tau = \frac{\eta\lambda}{\pi\gamma}$$

[Eq. II.3.19]
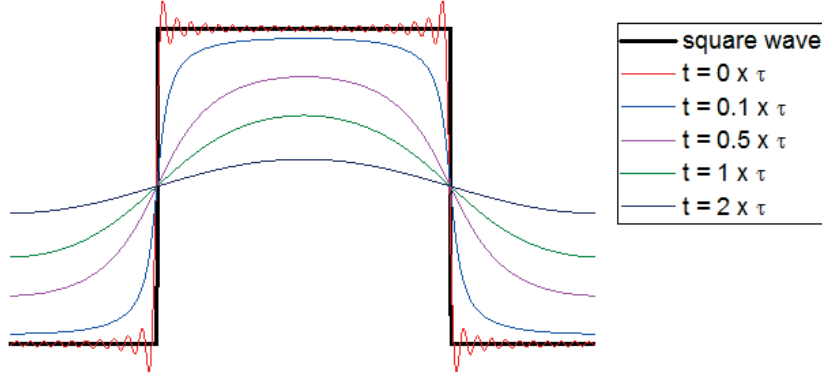
Figure II.3.3: the decay of a Fourier reconstructed square structure over time with N = 21

Note that in Figure II.3.2 above there is an overshoot at the discontinuity of the square function. However, it can be seen that such overshoot comes from the harmonic components of higher orders which disappear rapidly at a fraction of τ. Figure II.3.3 shows the simulation of a decay of a Fourier-reconstructed square structure over time with N= 21, and it can see that at $t = 0.1\,\tau$ all the wrinkles vanish and the reconstructed surface becomes smooth. It is also seen that at longer time ($t = 1\times\tau$ or $2\times\tau$), all harmonic modes except the first order disappear. In other words, after annealing long enough, the reflow behavior of a square wave would be similar to that of the first harmonic mode. This statement is indeed confirmed by both simulation result, and experimental results, shown in Figure II.3.4. In particular, from the decay of the Fourier-reconstructed surface, with N = 1 (dash red line) and with N = 21 (black line), it can be seen that above $t \approx 2\times\tau$ two decay rates are identical, while at shorter time $\tau \ll \tau$, the high order modes slow down the reflow. The image of an initial square PMMA structure after 10 hours of annealing at $170^o C$ clearly indicates a single harmonic mode with the same wavelength. Additional experiment data that back our calculation can be found in an on-going work, that will be submitted in 2017.
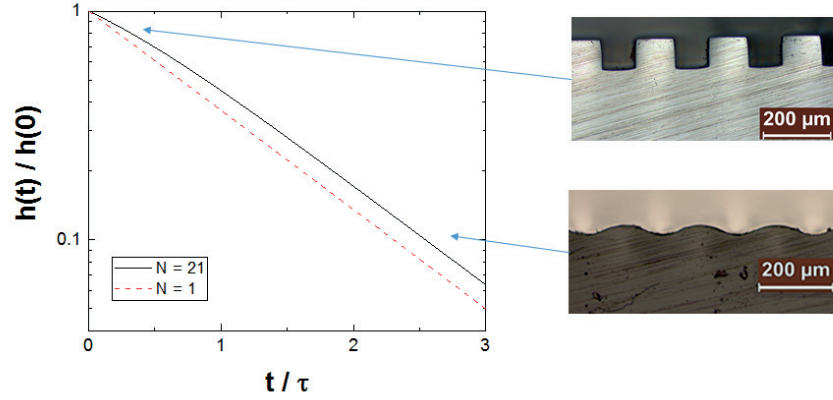
Figure II.3.4: the decay of Fourier-reconstructed of a square wave structure over time, with N = 1 (dash red line), and N = 21 (black line), and corresponding images for PMMA under annealing at $170^{o}C$ for (top) 15 minutes, (bottom) 600 minutes.

4. Reflow Behavior During Thermal Drawing Process

4.1   Mathematical Development

One key message from the previous section is that the reflow behavior of a polymer surface can be described with linear equations. As a consequence, any arbitrary periodical surface wave can be fully analytically examined as a Fourier series if their corresponding harmonic modes are known. Hence without loss of generality, we consider a sinusoidal surface wave of only one harmonic, with wave amplitude is denoted as h, and its wavelength as λ, as shown in Figure II.4.1.

The full deformation of the structure during a preform-to-fiber drawing can be decoupled into two mechanisms: the scaling deformation and the thermal deformation. The scaling deformation is due to the shrinking of the whole cross-section; while the thermal deformation is caused by the reflow behavior of the amorphous materials being heated above their glass transition temperature. It can be seen that the scaling deformation is related to an elongation in the drawing direction, the $z-$direction, and the thermal "reflow" relates to a flow solely in the $xy-$direction, perpendicular to the draw direction in the fiber cross-section. Both mechanisms induce a velocity field and contribute independently to the size reduction of a texture height.
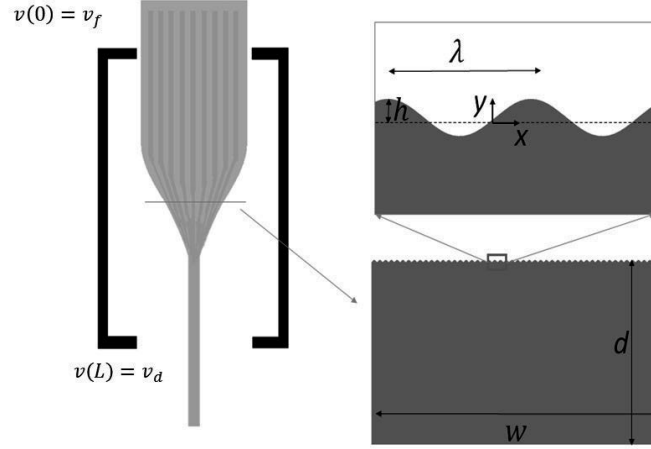
Figure II.4.1: schematic of a textured-preform-to-fiber drawing process; (bottom right) schematic of a cross-section of the preform with thickness d and width w ; (top right) schematic of a sinusoidal surface on the preform with the relevant parameters: the periodicity of the texture (λ), its amplitude (h).

Let us then consider a structure of height h at a position z along the drawing axis. At position $z + dz$, the structure has now a height $h + dh$ with $dh < 0$, and $dh = dh_{sc} + dh_{re}$, where dh_{sc} and dh_{re} are the contribution of scaling deformation and of thermal reflow deformation respectively. The scaling deformation at a given cross-section z is calculated from mass conservation, by assuming that the polymer is incompressible:

$$dh_{sc} = -\frac{1}{2}\frac{h}{v}\,dv$$

[Eq. II.4.1]

where $h = h(z)$ and $v = v(z)$ are the local height of the structure and the local speed along the drawing direction of the fiber respectively.

The thermal deformation, or "reflow", has been studied in previous section (see section I.2). In order to obtain the expression of the reflow deformation, we solve the Navier-Stokes equation for the polymer flow during the preform-to-fiber drawing process, by considering it as a Newtonian fluid in a low Reynold number regime. Indeed, for the flow of a textured polycarbonate fiber, the structure height is $h \approx 10^{-4}\,m$ at preform level, the drawing speed is $v \approx 10^{-2}\,m/s$, the lowest viscosity of polycarbonate during the draw is about $10^{5}\,Pa.s$, and its density $\rho \approx 10^{3}\,kg/m^{3}$, which gives a Reynolds number $Re = \rho v h/\eta \approx 10^{-7}$. Note that the

speed of thermal deformation u is smaller than the drawing speed v, and the height of the structure in the fiber is smaller than that of the preform, hence the Reynolds number of the flow at any positing along the drawing direction is smaller than the value estimated above. The flow is also considered as incompressible and irrotational.

In such regimes, the thermal deformation is given by:

$$dh_{re} = -\frac{\pi \gamma h}{\eta \lambda} \, dt = -\frac{\pi \gamma h}{\eta \lambda} \frac{dz}{v}$$

[Eq. II.4.2]

Note that in this configuration, only the height of the texture is changed but not its periodicity that is only subjected to the scaling effect.

The total deformation is the sum of the scaling deformation dh_{sc} expressed in II.4.1 and the thermal deformation expressed in II.3.2:

$$dh = dh_{sc} + dh_{re} = -\frac{1}{2} \frac{h}{v} \, dv - \frac{\pi \gamma h}{\eta \lambda v} \, dz$$

[Eq. II.4.3]

where γ is the surface tension of the polymer and η its viscosity.

The equation [II.3.3] gives us:

$$\frac{dh}{h} = -\frac{1}{2} \frac{dv}{v} - \frac{\pi \gamma}{\eta \lambda v} \, dz$$

[Eq. II.4.4]

The primitive integrals of left and right hand side of the equation II.4.4 is written as:

$$\ln h = -\frac{1}{2} \ln v - \frac{\pi \gamma}{\eta \lambda v} z + C$$

[Eq. II.4.5]

with C a constant.

If now we consider a preform-to-fiber process with a furnace of length L as shown in Figure II.3.1, with a structure at the preform of height h_0 at the entrance of the furnace $z = 0$, and the initial feeding speed V_0, the height of the structure at the output of the furnace where the final fiber is formed and the drawing speed is v_f becomes:

$$h(L) = h_0 \left(\frac{v_f}{V_0}\right)^{-\frac{1}{2}} exp \left(\int_0^L -\pi \frac{\gamma}{\eta \lambda} \frac{1}{v} \, dz)\right)$$

[Eq. II.4.6]

The equation [II.3.6] describes the final amplitude of the structure at fiber level and provides intriguing insights in the deformation of the structure during the thermal drawing process that we discuss in the following section.

4.2   Discussion on Reflow Factor

We rewrite the equation [II.3.6] as a dimensionless form:

$$\frac{h(L)}{h_0} = \left(\frac{v_f}{V_0}\right)^{-\frac{1}{2}} exp\left(\int_0^L -\pi\frac{\gamma}{\eta\lambda}\frac{1}{v}\, dz\right)$$

In the equation above, two factors are identified. The first factor corresponds to the draw-down ratio:

$$f_{sc} = \left(\frac{v_f}{V_0}\right)^{1/2}$$

[Eq. II.4.7]

associated with any thermal drawing, that results from mass conservation as the preform is pulled into a fiber. This factor corresponds to the mechanism behind the miniaturization using fiber thermal drawing proposed in this thesis. If the thermal reflow did not occur, then the miniaturization would be done by simply increase the drawing speed v_f up to the desired value of scaling factor.

The second factor represented by the exponential term accounts for the contribution of the Laplace pressure induced thermal reflow during drawing.

We define the shape factor as:

$$f_{sh} = exp(-\int_0^L \pi\frac{\gamma}{\eta\lambda}\frac{1}{v}dz)$$

[Eq. II.4.8]

and the reflow factor:

$$f_{re} = (1 - f_{sh}) = 1 - exp(-\int_0^L \pi\frac{\gamma}{\eta\lambda}\frac{1}{v}dz)$$

[Eq. II.4.9]

The shape factor f_{sh} varies from 1 and 0 and f_{re} from 0 to 1; $f_{sh} = 1$ and $f_{re} = 0$, correspond to the scenario where the structure is perfectly conserved (no reflow), while $f_{sh} = 0$ and $f_{re} = 1$ correspond to a structure that has completely collapsed. It is worth noting upfront that the shape factor f_{sh} tends to 0 exponentially faster as the structure size λ gets smaller, which is at the heart of the challenge we are addressing in this work.
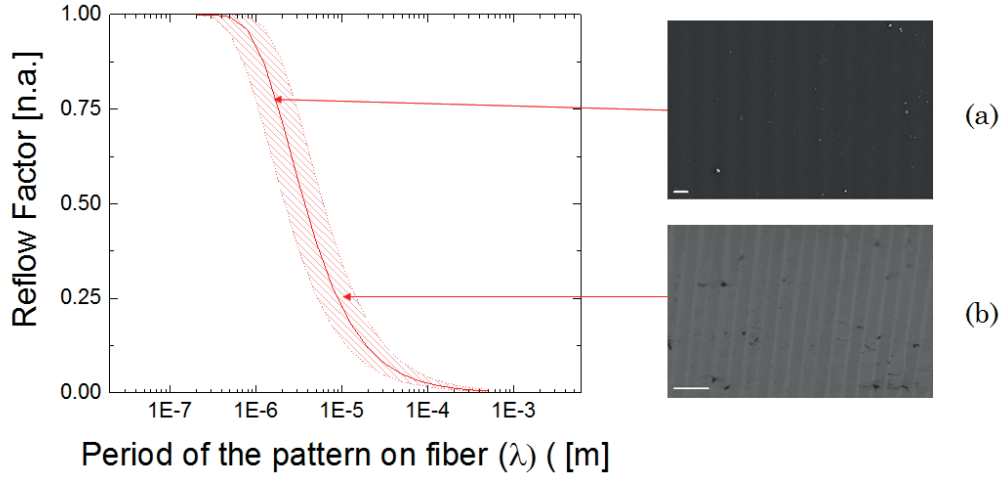
Figure II.4.2: Reflow factor versus the targeted periodicity of the texture at the fiber level and SEM pictures of PC fiber drawn at corresponding conditions.

In Figure II.4.2 we plot this reflow factor of a PC preform drawing with respect to the targeted periodicity of the structure at the fiber level for a scaling factor $f_{sc} = 20$. The velocity profile $v(z)$ was obtained from the analysis in section II.2. The viscosity profile $\eta(z)$ and the surface tension profile $\gamma(z)$ were calculated based on the temperature profile $T(z)$, also stated in the previous section II.2 as well as in Appendix A. In this analysis, the error was associated for the most part with the assessment of the temperature profile; hence in Figure II.3.2 we plotted the reflow factor including a surrounding dashed region that accounts for the error in this measurement that can be estimated to be $\pm 5^o C$. Even with this error, the reflow factor represents well for the physics behind the observed experimental results: f_{re} is indeed estimated to be around 0.8 for the 2 μm structure, and around 0.5 for the 10 μm structure as indicated on the graph by the red arrows. These values correspond to large deformations of initial shape, which were observed in the corresponding SEM pictures.

It can be seen that there is a severe deformation when the target size reaches about several micrometers for PC fiber. This limitation is inherent not only for the thermal drawing process, but for a wide range of polymer processing where heating is necessary to reduce the viscosity of polymer, such as for extrusion or injection molding. However, in thermal drawing, the viscosity of polymer is still relatively high compared to other common processing techniques, and it is also possible to engineer the surface/interface tension with multimaterial configuration, it can allow to to control the flow during the draw and diminish the reflow.

Let us consider more closely the expression of reflow factor:

$$f_{re} = 1 - \exp\left(-\int_0^L \pi \frac{\gamma}{\eta\lambda} \frac{1}{v} dz\right)$$

This expression provides intriguing guidance to reduce the reflow deformation, in other words, to get the value f_{re} as small as possible. There are three tunable parameters, with two depend on intrinsic materials properties, namely the viscosity and the surface tension and one processing parameter, the velocity profile. To have small f_{re}, we could either increase the viscosity, decrease the surface tension or increase the velocity profile. The materials of high mechanical strength such as PEI that can be pulled at high viscosity are less likely to reflow. Thermoplastics with low surface tension such as fluorinated polymers could also be used decrease the value of f_{re}. Even with these extreme cases, our calculations show that textures below a few micrometers could not be maintained even for PEI without severe deformation at the fiber level, corresponding to a reflow factor of about 0.25. This route has been taken, as reported in previous publication [33],[32], however the feature size could not reached below $10\ \mu m$, as predicted. The other way is to play with external parameters such as drawing at higher speed. This requires however to increase the furnace temperature to avoid raising the stress up to fiber breakage, which in turn can lower significantly the viscosity for some polymers and accelerate reflow. The effect of external parameters would be an interesting subject for future work, but is not studied in this thesis because our approach makes them irrelevant as it enables to suppress reflow regardless of material, structure and drawing parameters.

To alleviate the limitation associated with the drawing of a single material, we propose to exploit the thermal drawing of multi-material preforms. By co-drawing two textured polymers in intimate contact, we can drastically reduce the interfacial tension of the textured polymers (in Appendix A), which results in a drop of the reflow factor. For instant, while the surface tension of polycarbonate is $35.1\ \frac{mN}{m}$ and of polyethylene is $28.8\frac{mN}{m}$ at 140^oC [44], their interfacial tension is one order of magnitude smaller, being $4.8\frac{mN}{m}$. Replacing this value into the expression [II.3.9], we obtain significantly lower reflow factor for the same targeted feature-size on fiber. This is demonstrated in Figure II.3.3, where we plot in the same graph the reflow factor for a PC draw with two value of γ, one for PC and the other for the interface PC/PE.

We also put the reflow for a typical PEI draw to show that the multimaterial approach would surpass largely the single-material approach, even for the extreme case. In particular, it can be seen from the graph that even at submicrometer scale targeted feature size, the PC/PE interface allows a relatively small reflow factor. For the interface with even smaller tension, such as between PC and PMMA, theoretically it would even possible to reach $10\ nm$ structure size. The multimaterial approach hence constitutes the ideal strategy for nanofabrication based on thermal drawing.
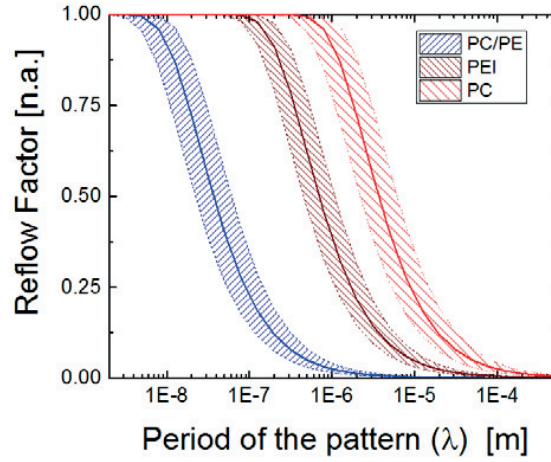
Figure II.4.3: Reflow factor versus targeted feature-size of the pattern on fiber for different configurations. Red: single-material preform made of PC, brown: single-material preform made of PEI, blue: multimaterial preform from PC/cPE. The lines in the center correspond to the empirical drawing temperature for each preform, while the striped zones indicate the deviation of the temperature measurement.

5. Summary

In this chapter, a technical description of the thermal drawing technique was presented, following by a mathematical description of the shape of the preform-to-fiber neck-down region. We employed a simple analytical development by considering that the preform deformed as a Newtonian incompressible flow in low Reynold number regimes, and obtained a formula for the shape of the neck-down region that matched well with experiment. Then, the notion of reflow of polymer surface under isothermal annealing was introduced. By solving Navier-Stokes equation for the flow of polymer at surface level, it was shown that the amplitude of a harmonic surface decayed over time, with a characteristic time proportional to

the viscosity of the polymer and to the period of the wave, also inversely proportional to the polymer surface tension. In addition, it was demonstrated that the reflow behavior could be described with linear equation systems, allowing the use of Fourier series for more complex cases when an arbitrary surface was considered. Finally, the dynamic thermal reflow during thermal drawing process was studied, from which it was clearly shown that this reflow behavior was the main obstacle for the fabrication of micro and nano-scale structure on fiber surfaces. We identified and examined several key parameters that would enable the suppression of this deformation; among which the engineering of surface/interfacial tension emerged as the ideal route to follow. This strategy and its implementation are elaborated in greater detail in the following chapter.

Chapter III.

Fabrication of Submicrometer Patterned Fibers

In the previous section, the reflow deformation was identified as the main challenge to thermal drawing for micro- and nano-fabrication. It was also shown that this deformation could be diminished by reducing surface/interface tension of the textured polymers. In consequence, we proposed a strategy based on the multimaterial drawing approach, aiming to engineer the surface/interface tension. In this section, the detail of this approach and its implementation are presented. We begin with the description of the preform patterning techniques. Beside the conventional drilling, we report here a novel method to create patterned preforms based on micro-imprinting that allows us to achieve sub-millimeter textured rectangular and cylindrical preforms. Then in section III.2, the choice for the constituent materials of a textured preform is discussed, followed by a brief description of the preform finalization by thermal welding. Finally, the drawing of immiscible polymers is highlighted in section III.3.

1. Patterning methods of Preform Surface

1.1.1 Patterning via mechanical machining

The mechanical machining is easy-to-use, versatile and low-cost and has been used extensively in preform fabrication for making internal structure [8,14,22,45] or even on the surface of the preform [32,33].

The technique works extremely well to create millimeter-size patterns and even can reach as small as 250-μm-size square structures on the surface of the preform. The technique was employed to pattern both rectangular or even cylindrical preform. In this thesis, two types of milling were used to create square patterns on the surface of rectangular preforms: a horizontal-axis rotational end mill and a more conventional vertical axis end mill. Figure III.1.2 (a) and (b) show the milling machines (FLOT SB30V) and a horizontal axis end mill, and Figure III.1.2 (c) showed the cross-section of a milled preform with 5 different square structures: 4 mm, 2 mm, 1 mm, 0.5 mm and 0.25 mm.

<div align="center">(a)   (b)   (c)</div>
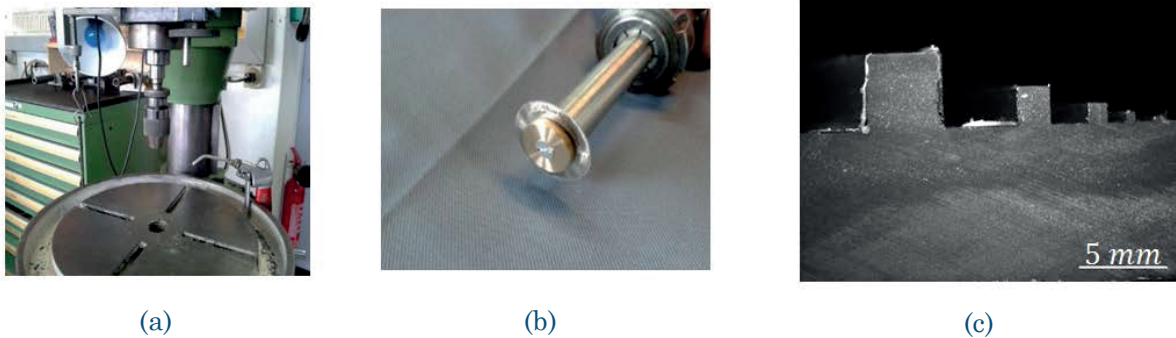
Figure III.1.1: Milling machines for preform patterning. (a) mechanical milling machine (FLOT SB30V), (b) rotational end-mil to create $250\ \mu m$ grooves on preforms, (c) cross-section of a preform with different square structures.

The main drawback of patterning via mechanical milling is the low resolution of patterns and machining time depends linearly on the number of grooves, hence the technique is not suitable for high-resolution patterning required to achieve submicrometer structure on fiber. In this work, with help from the Machine Shop of the Material Science Department (ATMX), the highest resolution patterns were of $250\ \mu m$-size on a preform of cross-section $5\ mm \times 25\ mm$. To reach $500\ nm$-size structure on fiber, the draw-down ratio would become 500 and the size of the resulted fiber cross-section would be $10\ \mu m \times 50\ \mu m$. These values are extremely difficult to obtain with a lab-size drawing tower. Although it is possible to draw a preform several time to reach this draw-down ration, the final fiber is too small to handle properly.

1.1.2   Patterning via thermal imprinting

Limitation of the milling technique resulted in a need for a texturing technique that could fabricate uniform sub-millimeter patterns on a centimeter-square area to cover the preform surface. Hot-embossing/micro-imprinting, a rapid, easy-to-use and high-throughput technique fulfilled these requirements and was used for the first time as a preform making method in this thesis. The technique consists of the replication of a pre-structure stamp on a polymer surface by pressing the stamp onto a molten polymer until it fully flows inside the stamp structure. A typical embossing process takes less than half an hour to create a patterned preform, including the heating and cooling time, and a stamp can be reused many times. The highest cost of the whole process lies therefore on the stamp fabrication. Such stamps can be made from different materials, among which the two most common are metals and silicon. Metal stamps are usually

created by electrodeposition or laser cutting, which are time-consuming and expensive. In consequence, silicon was the material of choice for stamp making in the beginning of this project.

Hot embossing of Si stamps on thermoplastics was however limited by a difficult demolding step. Such difficulty came from the difference of thermal expansion coefficient between Si and polymers, and also from the fragility of Silicon. Figure III.1.2 shows a stamped polymer surface with a Si master stuck on to its surface, even when the wafer was totally destroyed. Therefore, we turned into soft-imprinting by adding additional step of making soft stamps from a Si-stamp. The process of soft-embossing is described in the following section.

Figure III.1.2: Demolding of Si mold was challenging, as illustrated by the Si mold on a PC preform.

Compared to the hot-embossing presented in the section above, the term "soft-imprinting" is used to emphasize the fact that the stamp in this process is made of a soft material, especially polydimethylsiloxane (PDMS), instead of a hard material such as Si or metal. Otherwise, the two techniques remain identical.

Due to the capacity of replication from a single Si master, PDMS is an attractive material for mold fabrication due to the low fabrication cost and short processing times. Its thermal stability is up to $250^{o}C$, largely above the glass transition of common thermoplastics such as PMMA, PC, PSu. In addition, its flexibility and low adhesion to hot-pressed polymers render the demolding effortless [46].

Figure III.1.3 shows the process of making a PDMS mold from a Si master. First, a mixed and degassed PDMS pre-polymer was made from mixing base and cross-linker with a ratio of 10:1 (Dow Corning Sylgard 184). The mixture was then poured on the Si-wafer before being baked for at least 2 hours inside an oven at $80^{o}C$ for polymerization. After baking, the PDMS mold replicating the feature of the Si master was delaminated and was used as mold for soft embossing.

Figure III.1.3: The imprinting process for the preform patterning

For an imprinting process, the mold and polymer substrate were preheated up to the processing temperature, then a pressure was applied so that the molten polymer flew covering patterned. Pressing time was calibrated so that the pattern was fully transferred without destroying the polymer substrate. Then the whole system was cooled down to room temperature before being demolded. The processing temperature, pressure and pressing duration of several polymers are shown in the table III.1.1.

Thermoplastics	Temperature (°C)	Pressure (MPa)	Duration (min)
PC	175	0.1	5
PMMA	150	0.1	5
PSu	215	0.1	5

The imprinting technique allowed to create a uniform pattern covering the whole surface of polymer plates, which were used directly as preform. Figure III.1.4 shows the cross-section of patterned polymer plate created via soft-embossing.

(a) (b) (c)
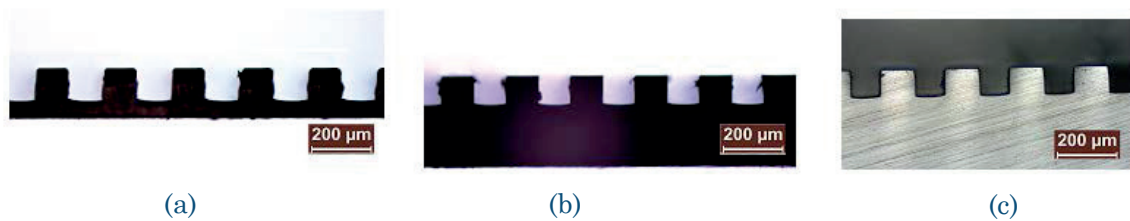
Figure III.1.4: Cross-section image of embossed polymers (a) PSu film (b) cPC and (c) PC.

Making of cylindrical patterned preform

The thermal imprinting technique was used to make patterned cylindrical preform. First, the pattern was created on a polymer film, which was then rolled tightly around a cylindrical tube made of the same polymer. Consequently, the whole structure was put in a vacuum oven set at a temperature specific to the constituting polymer. An empirical rule was established during this thesis that the temperature for consolidation was about $30^{o}C$ higher than the glass transition temperature of the polymer; for example, $T_{consolidation}(PMMA, PC, PSu, PEI) = (150^{o}C, 190^{o}C, 225^{o}C, 250^{o}C)$, with the consolidation time of 10 minutes. When the consolidation finished, a cylindrical preform with its whole surface being pattered was created.

2. Material Selection and Preform Consolidation

Our strategy presented in Chapter II was to use multimaterial preform design in order to reduce the reflow factor, since the interfacial tension between polymers could be engineered to be significantly lower than the surface tension of each component. As a consequence, the textured surface of the imprinted polymer, called "main polymer", was then encapsulated by a second polymer, which is called "sacrificial", because it would be removed after the draw, leaving the final fiber with a free textured surface. In this section, we present the criteria to choose the main and the sacrificial material and their properties.

2.1   Main Materials

The textured fibers in this thesis were mainly made of PC and PMMA. PC and PMMA were chosen because of their availability with the commercial name Makrolon© and Plexiglass©, they have been employed before in thermal drawing [11] and their optical transparency in a large spectrum. It is proven that PC is biocompatible [47], therefore the PC textured fiber was directly employed in biology experiments without further treatment. Nevertheless, the method developed herein was also applied to other soft materials, and in principle can be extended to other kind of thermoplastics. To some extent, even the "sacrificial polymer" could also be used, because it was equally textured after the draw.

The surface tension of PC and PMMA are shown in the following table (data from [44,48]):

Material	γ [mN/m] (at 20^{oC})	$-d\gamma/dT$ [mN/(m.deg)]
PC	49.2	0.060
PMMA	41.1	0.076

The variation of surface tension versus temperature is negligible. In some further calculations, we consider the value of the surface tension is independent from temperature.

The rheological properties of PC and PMMA were measured with a rheometer (TA AR2000, with shear rate of $2.5\ s^{-1}$), and the flow viscosity of the two materials is shown in Figure III.2.1. The dependence of viscosity on temperature followed approximatively Arrhenius's law, and can be modeled as:

$$\eta_{PC} = \exp\left(\frac{22493}{T + 273.15} - 35.287\right)$$

[Eq. III.2.1]

$$\eta_{PMMA} = \exp\left(\frac{13018}{T + 273.15} - 15.423\right)$$

[Eq. III.2.2]
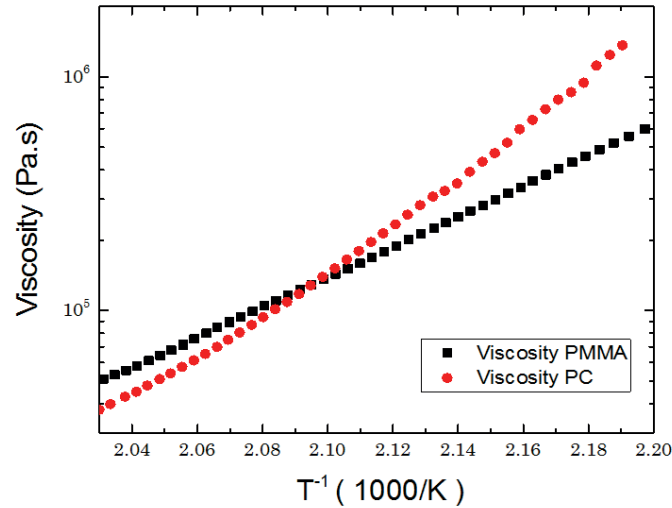
Figure III.2.1: Experimental data of viscosity of PC and PMMA as a function of temperature (measured with a Rheometer AR2000 TA instrument with shear rate of $2.5\ s^{-1}$).

2.2   Sacrificial Material

The sacrificial material that is used to cover the main polymer textured surface satisfies the following requirements:

- Its rheology property need to be suitable for co-drawing with the cladding material.
- It has a low interfacial tension with the cladding material in order to reduce the reflow.
- In order to be removed easily after drawing, either it needs to have a low adhesion energy with the cladding material or there must be an orthogonal dissolving solvent for selective etching.
- Its thermal conductivity should be high to reduce the drawing temperature at the interface with the cladding material.

For our cladding materials, PC and PMMA, an ideal candidate that satisfies all the above requirements was found to be the carbon-loaded polyethylene (cPE). cPE was already used in the thermal drawing technique with PC and PMMA [11,16]. The interfacial tensions of cPE/PC and cPE/PMMA are much lower than that of PC and PMMA, as shown in the following table [44,48,49]:

Material	γ [mN/m] (at 20^{oC})	$-d\gamma/dT$ [mN/(m.deg)]
PC/PE	6.9	0.018
PMMA/PE	9.7	0.018

In addition, PE is immiscible with both PC and PMMA [49,50], although the shear strength of the interface between PC and cPE is strong enough to be co-drawn. Finally, the carbon-loaded composite has a higher thermal conductivity than the pure polymer, allowing a decrease of temperature at the interface.

2.3   Preform Consolidation

A typical rectangular preform consisted of two main polymer textured plates, sandwiching a sacrificial layer (Figure III.2.2). The ribbons were only textured on 1 side so that in subsequent experiments, we could compare the effect of the textured surface to the smooth surface of the same fiber. This particular design allowed to achieve two textured ribbons in a single draw as well. The three layers were consolidated using thermal welding (with the same machine as for patterning previously) at $140^{o}C$ for PC and $120^{o}C$ for PMMA. At this respective temperature, the texture on the main polymer plates was not deformed, while PE flew easily to create intimate contact. After 30 minutes, the preform was taken out of the thermal imprinter and was ready to be drawn.
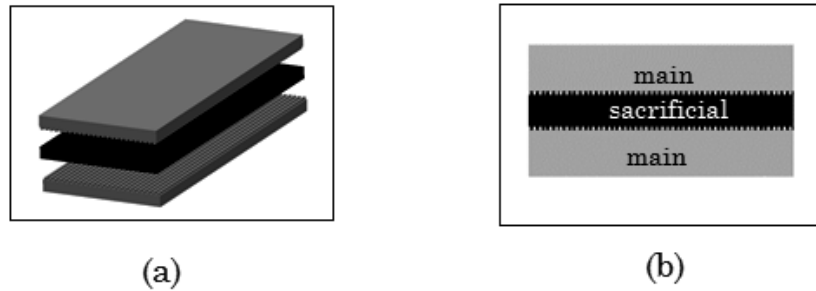
Figure III.2.2: schematic of the preform before and after consolidation.

3. Drawing of Immiscible Polymer Preforms

3.1   General Setting

In Chapter II, the mathematical considerations on the thermal drawing technique showed that the most influencing three parameters in a drawing experiment, a "draw" for short, were the profile temperature in the furnace, the feeding speed and the drawing speed. These parameters are active parameters because one can directly modify them during the draw. There are also two important but indirect parameters: the fiber size and its tension, related to the three active parameters. They are also monitored in real time during the drawing process.

Figure III.3.1 shows a picture of the drawing tower employed in this thesis. From the top to the bottom, the main components of the tower are the feeding system, where the preform is attached through a preform-holder, the furnace with different heating zones, the

Figure III.3.1: the drawing tower at FIMAP with its main components. From P.H. Prideaux.

monitoring systems that measure the fiber diameter and tension, and the capstan that pulls the fiber with a controlled speed. In addition, a spooler can be used to collect long fiber by rolling it around a drum.

All fibers in this thesis were drawn with a feeding speed fixed at $1\ mm/min$. The drawing speed, in consequence, was fixed at $100\ mm/min$ for a draw-down ratio of 10 and at $400\ mm/min$ for a draw-down ratio of 20. By doing so, the influence of external parameters on the reflow factor was eliminated (see equation [II.3.6]). In addition, the drawing speed also defines the pre-

heating time of the preform in the fiber, whereas the drawing speed defines the quenching time of the fiber.

Regarding the temperature of a draw, it is desirable that the furnace has different heating zones for a better control of the temperature profile. In the FIMAP furnace, there are three heating zones: the top zone, or preheating zone, the middle zone, or annealing zone, and the bottom zone, or quenching zone. The temperature of each zone is controlled in real time by computer and monitored by a thermocouple that measures the temperature of the heating wall.

A typical setting temperature for a draw of PMMA and PC is shown in the following table:

Furnace	Top zone	Middle zone	Bottom zone
PMMA	120°C	250 °C	85 °C
PC	150 °C	270 °C	85 °C

Note that in an experiment, the set temperature was not the real temperature that the preform experiences during the drawing due to heat transfer by convection or diffusion. In order to know the temperature on the preform surface, a calibration was performed. A thermocouple was pasted at the preform-to-fiber neck-down position, and was put at different positions along the z-direction of the furnace to measure the temperature profile. The measured temperature

Figure III.3.2: Calibration of the drawing temperature for PC and PMMA preforms

was almost 100°C lower than the set temperature; such a low temperature might come from the low stabilization of the thermocouple, it took almost two hours to reach a stabilization point, and during the calibration, the iris at the bottom of the furnace could not be fully closed. Nevertheless, the shape 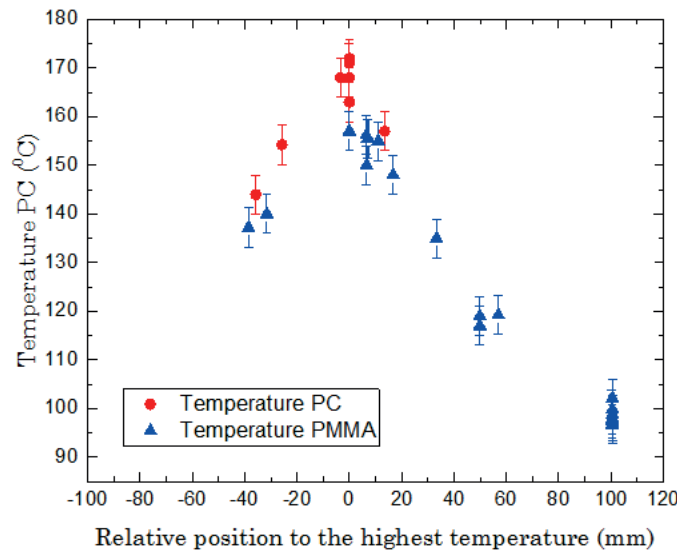of the temperature profile around the highest temperature remained almost identical for different setting temperatures. Moreover, the measured temperature was higher than the T_g only in the zone ±10 cm around the maximal temperature point. Taking into account these reasons, the drawing temperature profile along the preform-to-fiber can be modelled empirically as:

$$T(z) = T_{max} - a \, z^2$$

[Eq. III.3.1]

with $T_{max} = T_{setting} - 75 \pm 5 \, {}^oC$, and $a = 0.143 \, (\frac{deg}{mm^2})$

3.2   Drawing of Multimaterial Preforms:

The multimaterial preforms fabricated with the methods described in the previous section were drawn into fiber. Schematics of the draw of multimaterial preforms are shown in Figure III.3.3 (a), (b) and (c). In these schematic, the black parts are sacrificial material, and in Figure III.3.3 (c) the post-drawing separation of the sacrificial to the main part was highlighted. The sacrificial material cPE had a significantly lower viscosity than that of the main materials, PC and PMMA; the drawing parameters remained the same as previously stated. With a draw-down ratio of 20, 40 m- fiber was drawn from a preform of length 10 cm. The extended length of a multimaterial fiber is shown in Figure III.3.3 (b). Finally, the sacrificial layer was separated by a simple mechanical pulling, leaving the two patterned surface ribbons of the main material. The low interfacial tension reduced significantly the thermal reflow deformation, as predicted mathematically in the previous section, and confirmed by the SEM images of a textured fiber and its cross-section in Figure III.3.3. Our approach was equally applied to a variety of preform geometries; fibers obtained from these draws are presented in the next section.

Note that the mechanical peeling-off presented here worked if the main and the sacrificial material were immiscible. In case where they were miscible, the separation was done by chemical selective etching in a solvent orthogonally dissolving the sacrificial while leaving the main material intact. For instance, in a fiber where PC was the main material and PMMA was

the sacrificial, acetic acid was employed. However, this chemical separation was time consuming, and clearly less efficient than the mechanical separation.
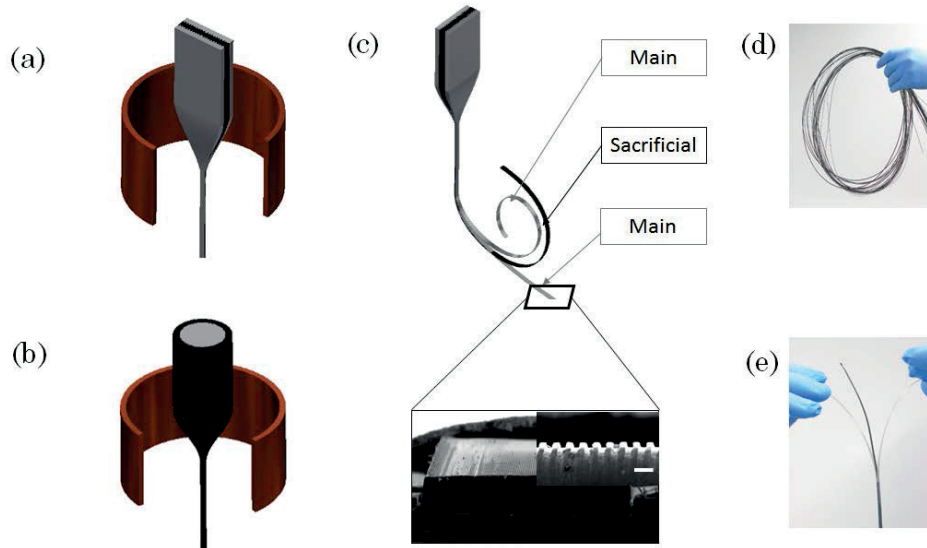
Figure III.3.3: Schematics of the drawing of multi-immiscible-material preform in (a) rectangular configuration and (b) circular configuration. (c) schematic highlights the post drawing separation, with an SEM image of the cross-section of the main material. (c) extended length of fibers could be fabricated in a single draw and (d) components could be easily separated to create free patterned surface on fiber.

Discussion on the temperature drop at the interface between main/sacrificial layers

One of the criteria to choose cPE was its high thermal conductivity, which would lead to a drop of temperature at the interface between the main and the sacrificial layers, and subsequently to an increase of local viscosity. However, in this section, we show that this effect played a minor role in reducing the thermal reflow factor.

In order to evaluate the temperature at the interface of different layers in a multimaterial preform, we performed a finite element simulation (COMSOL ®) of its temperature profile during the preheating process. The result of the simulation is shown in Figure III.3.4. In this model, the preform consisted of three layers comprising a high thermal conductivity layer,

corresponding to the sacrificial cPE layer, and two layers of PMMA. All the physical parameters of the middle layer were those of pure PE, except its thermal conductivity which was varied from the value of pure PE to the value of 15% volume carbon-black-filled PE. The effective thermal conductivity of the composite was estimated by considering a weight fraction effect, using the equation $k_{eff} = (1 - \phi)k_{matrix} + \phi \, k_{filler}$. Here the matrix was the pure PE and the filler was the carbon black. The temperature was set at three zones during the draw, and all boundaries were considered perfectly isolating. The preform holder was made of PMMA, of which one end was in contact with room temperature. Convection was not considered in this simulation.
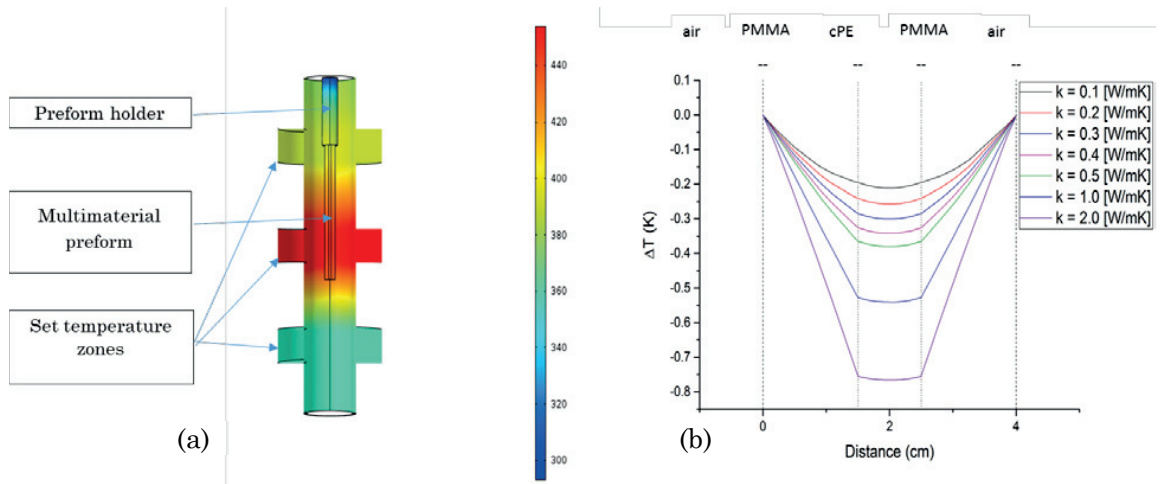
Figure III.3.4: Finite element simulation of temperature distribution in a preform (a) schematic of the system and its temperature distribution at equilibrium; (b) temperature along the line going through the preform center at the neck-down position, dash lines represent the air/PMMA interface, dot lines represent PMMA/cPE interface, k is the thermal conductivity of the sacrificial layer.

Figure III.3.4(b) shows the different temperature profiles between the PMMA/air interface and PMMA/sacrificing layer (cPE) interface, where the pattern was located, for different thermal conductivity of the sacrificing layer. The temperature profile was taken through the center of the preform at the neck-down position. The lower temperature was observed in the cPE layer that acted as a heat sink. The effect is however not significant since even for a ΔT of 2^oC, the change on viscosity and of the reflow factor r_{re} is around 0.2%. In conclusion, the main reason for a small reflow factor in a multimaterial preform draw was the small interfacial tension between the main and the sacrificial layers.

3.3 Subtlety of Drawing Immiscible Polymers

The low adhesion between the sacrificial layer and the main layers, originating from their immiscibility, allowed an easy and fast mechanical removal. At the same time, the interlayer adhesion remained high enough so that the layers did not delaminate during the draw. In this section, we discuss the strength of the interface of the immiscible polymers, and how the drawing parameter should be adjusted to ensure the realization of a fiber composed of immiscible layers.

In fact, for post drawing separation, it was the tensile strength of the interface that needed to be overcome, while during the fiber drawing process, it was the shear strength of the interface that enabled the co-drawing of different layers. The tensile and shear directions regarding the interface are illustrated in the schematic III.3.5(a). Graph III.3.5(b) shows the experimental results of interfacial PC/cPE tensile and shear strength versus welding time at $150^o C$ under pressure of 0.1 MPa, and it is clearly seen that the tensile strength is significantly smaller than the shear strength.

(a)   (b)
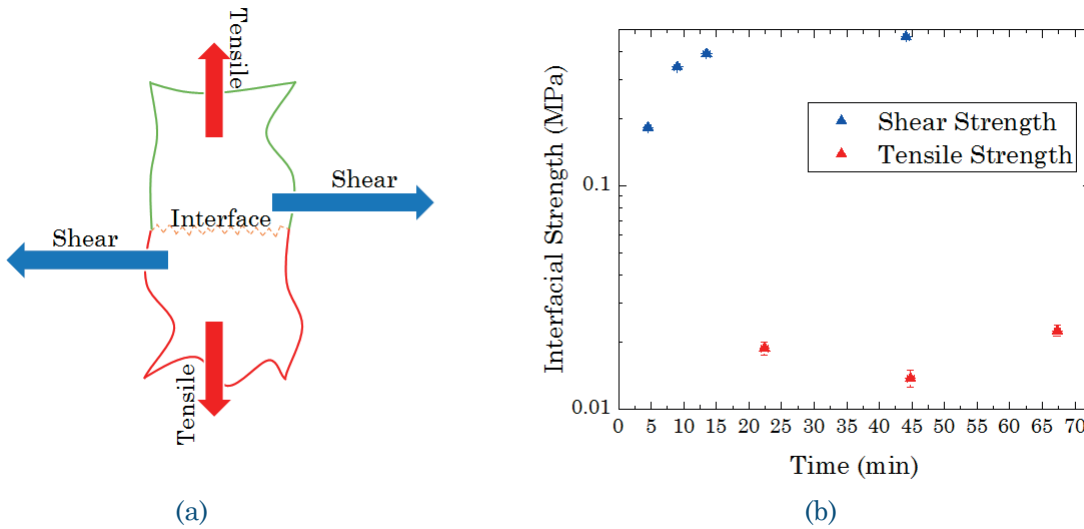
Figure III.3.5: (a) schematic of tensile and shear directions at polymer interface (b) experimental data of tensile and shear strength of PC/cPE interface after thermal welding at $150^o C$.

The large difference between shear and tensile strength was mainly due to the roughness of the interface, as depicted in the schematic III.3.5(a). Intuitively, to break the interface along the

direction parallel to it (shear), it is necessary to overcome not only the possible chain entanglement, but also the physical resistance from bumps and holes of the rough surface; whereas to break the interface along the direction perpendicular to it (tensile), only chain entanglement needs to be taken into account. In our case of textured interface between immiscible polymers, although the entanglement can be negligible, surface roughness increases substantially due to the presence of micro patterns, hence the shear strength increases to keep immiscible layers undergoing the drawing without delaminating.

The delamination of immiscible layers during the drawing process could come, however, from the low tensile strength of their interface. Indeed, it can be shown mathematically that there is a separating force that acts on preform constituent layers in the neck-down region, which detaches them if it becomes stronger than the tensile strength (see Figure III.3.6 (a)). Let us consider a typical neck-down shape in Figure III.3.6 (b), with a velocity profile can be obtained analytically with equation II.2.1. The acceleration of one element in the neck-down region is the sum of two components, the normal and tangential acceleration:

$$\vec{a} = \vec{a_n} + \vec{a_t}$$

[Eq. III.3.2]

The tangential acceleration is the derivation of speed along the speed line:

$$\vec{a_t} = \frac{\partial v}{\partial t}\ \vec{e_z} \approx\ v.\frac{\partial v_z}{\partial z}\ \vec{e_z}$$

[Eq. III.3.3]

The normal acceleration is the centrifugal acceleration which is proportional to the curvature κ of the speed line:

$$\vec{a_n} = v^2 \cdot \kappa\ \vec{e_n} \approx v^2 \frac{\partial^2 r(z)}{\partial z^2}\ \vec{e_n}$$

[Eq. III.3.4]

In the two equations above, we assume that $v_z \gg v_r$ and $\frac{\partial r(z)}{\partial z} \ll 1$, which is valid here because the neck-down region is much longer than the width and thickness of the preform.

Without loss of generality we may consider the element on surface where $r(z) = R(z)$ to estimate the sign and magnitude of the two force components. While the tangential component is always positive because both v_R and $\partial v_R/\partial z$ are positive at every z, which means that all surface elements accelerate during the preform-to-fiber deformation, the sign of the normal

component $\overrightarrow{a_n}$ is the same as the curvature of the function $R(z)$. Since the curvature κ changes sign at the inflation point (Figure III.3.6 (b), red line), there is a separating force the part of the neck-down region after the inflation point, pointing outward the bulk material, applied the surface elements; while above the inflation point, the total force points inward to bulk material. However, the value of $v_R^2(z)$ increase significantly at the inflation point, the acceleration being a product of κ and $v_R^2(z)$ is significantly higher below the inflation point than above (Figure III.3.6(b) bottom shows the normal acceleration in the considered segment, and the small graph on the right corner represents normal acceleration just before the inflation point).

(a)   (b)
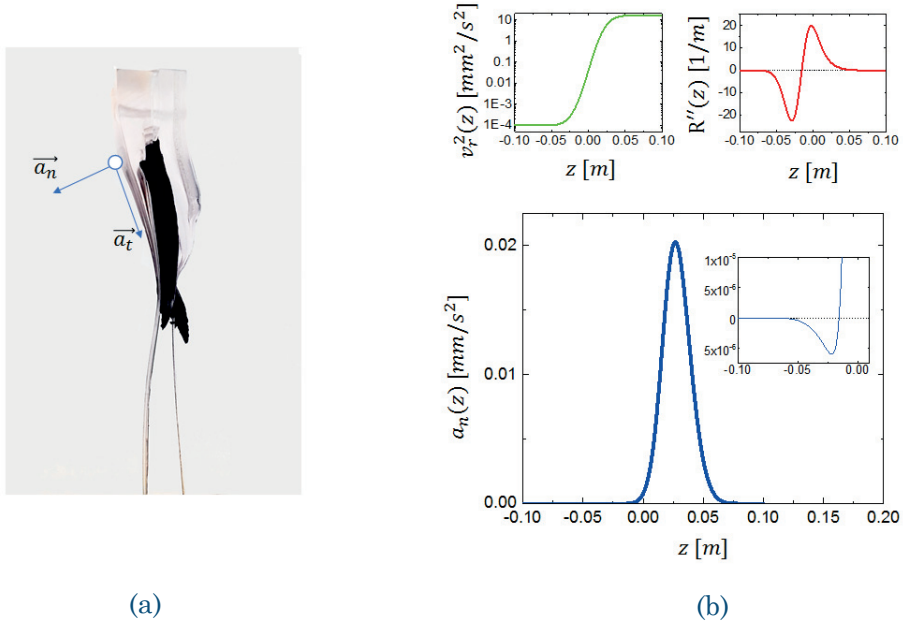
Figure III.3.6: (a) a preform with immiscible layers that separated from each other while being drawn, and schematic of tangential and normal acceleration of a surface element in the neck-down region. (b) the simulated value of tangential acceleration (blue line), being proportional to the square of speed (green line) and the second derivative of the function $R(z)$ (red line).

In conclusion, the difference between shear and tensile strength of the interface between immiscible polymers allows the co-drawing of a preform constituted of immiscible layers, at the same time allows an easy and fast separation of these layers at the fiber level to expose the textured surface. A separating force was taken into account in our process, and the drawing parameters were set to prevent the delamination of immiscible layers.

Microstructured Fibers and their Applications

In this chapter, we present a wide range of micrometer- and submicrometer-patterned fibers obtained in this thesis in order to highlight the ability and versatility of the novel approach described in the previous section. The challenge of characterization of submicrometer is also discussed. Finally, selected applications of textured fibers are shown to demonstrate the unique opportunities that our work brings.

1. Micrometer and Submicrometer Patterned Fibers

Patterned fiber with a variety of shapes and structures were created during this thesis. The textures on fibers can range from tens of micrometers down to a few hundreds of nanometer, and can be organized in any configuration as initially selected in the macroscopic preform (periodic, aperiodic etc.) A textured PC preform created by mechanical machining (Figure IV.1.1 (left), also shown in Figure III.1.1 (c)) was drawn into a ribbon with five square-shape structures on its surface, which are $20\,\mu m$, $10\,\mu m$, $5\,\mu m$, $2\,\mu m$, $1\,\mu m$ in width and depth from the left respectively. The preform was drawn twice, meaning that the fiber obtained after first draw was served as part of the preform in the second draw, enable a draw-down ratio of around 200 times. From this image, it is clearly seen that the low interfacial tension between the cladding and the
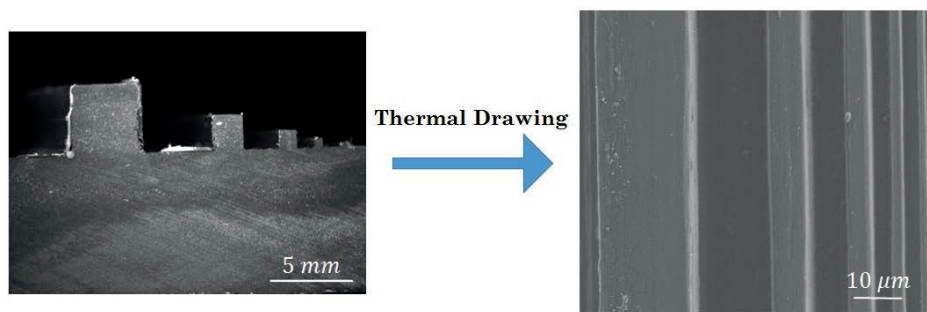

Figure IV.1.1: SEM pictures of preform with different feature size and b the patterned covers the whole surface

sacrificial materials reduced significantly the thermal reflow deformation, as predicted mathematically in the previous section.

Using the imprinting technique for preform patterning, it is possible to fully cover the desired texture on fiber surface in much shorter time than using mechanical machining. Moreover, with the imprinted structures can easily vary from 100 μm to 10 μm, a micrometer and submicrometer pattered fiber could be achieved in a single draw, instead of multiple draws. Figure IV.1.2 shows the SEM images of a typical PC fiber, drawn from a 100 μm mold, with a periodically square-shape patterns over its surface and its cross-section. In particular, by showing a sharp texture of less than 10 μm in the image of the fiber cross-section (on the right), we emphasize again the low reflow deformation during the draw of this fiber. Next, Figure IV.1.3 demonstrates the SEM top-view picture of a submicrometer patterned fiber, with the feature size of 300 nm. The initial pattern was created on a PC plate by thermal imprinting of a 10 μm PDMS mold, and the draw-down ratio was set to be from 20 times to 50 times. This structure is the smallest pattern ever reported fabricated with thermal drawing technique.
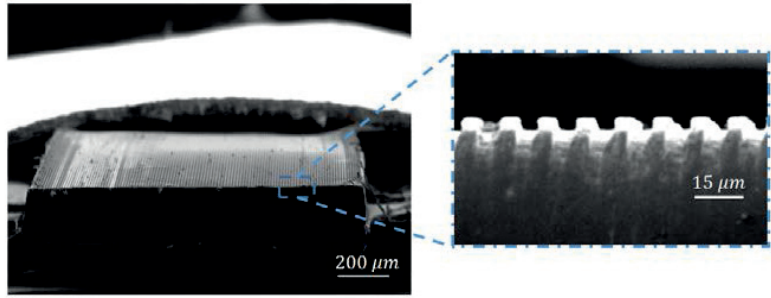

Figure IV.1.2: SEM image of a textured PC fibers and its cross-section. The pattern is clearly seen to cover the whole fiber surface.
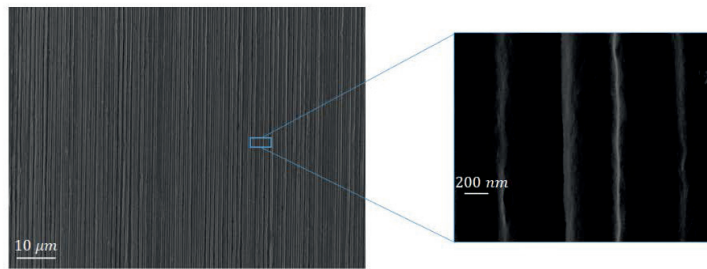

Figure IV.1.3: SEM top-view image of a submicrometer patterned PC fiber, and the zoom-in image of its 300 nm structure.

Furthermore, we combined the milling and hot-embossing techniques to create a hierarchical structure, illustrated in Figure IV.1.4. Specifically, Figure IV.1.4 (a) presents the schematic of the hierarchical structure, with one level on top of the other. Application wise, the larger structure could be used for surface treatment in biology, whereas the smaller structures can be used in optic visible domain. SEM pictures in Figure IV.1.4 (b) show different levels of the structures, from left to right being on fiber level of $1\,mm$ (fiber width), the first pattern level of $20\,\mu m$, and the second level of $5\,\mu m$ was fabricated. Moreover, this structure is reproduced uniformly over hundreds of meters of fiber length, highlighting the simplicity of our approach to fabricate hierarchical architectures that are difficult to realize with traditional lithographic methods.

(a)

(b)
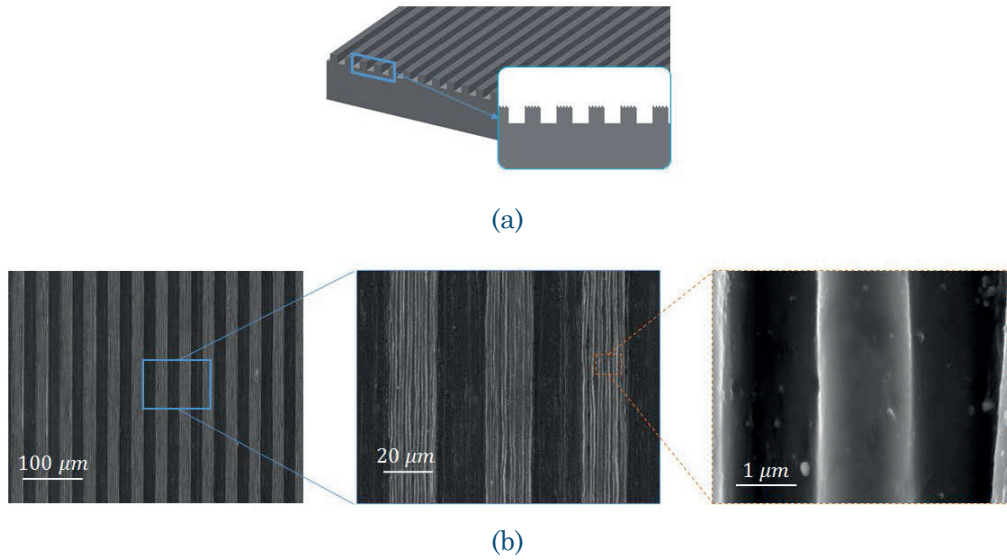
Figure IV.1.4: (a) Schematic of a double-texture ribbon and
(b) SEM image of such structure with different zoom-in levels.

Our approach can be equally applied to any fiber geometry, including the circular fibers, and not only on the outer surface but also on the inner surface of hollow core fibers. This is illustrated in Figure IV.1.5. The left figure is an optical microscope images taken on a PC fiber with a textured outside surface of $5\,\mu m$ in feature size, while the right is micrographs of a hollow core PC fiber with an $8\,\mu m$ feature size patterns on the inside. Circular fibers were also fabricated with micrometer and submicrometer patterns on their outer surface as well as on their inner surface. Note that we show textures with such scale so that it could clearly illustrate the high curvature; submicrometer textures could be achieved on the surface of circular fiber as easily as on the surface of flat ribbons.
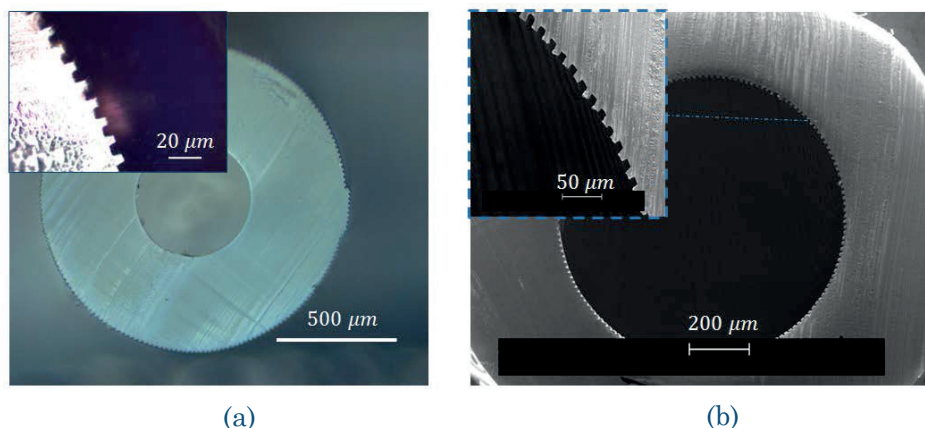
Figure IV.1.5: circular fiber with textured (a) on the outside surface and (b) on the inside surface.

To expose the patterned inner surface of a hollow core fiber, both dissolution approach and mechanical approach were used, and showed that one can achieve such a fiber of centimeter length. To get even longer textured fibers, addition work on removal would be necessary, for example, by finding a better solvent to dissolve the sacrificial layer, or by generating delamination of the sacrificial layer and the patterned surface before mechanical removal.

Finally, we demonstrate the use of PC and PMMA fibers as mold to create patterns on flat or large curvature surfaces of other materials. A material of choice for the proof-of-concept is poly dimethyl siloxane (PDMS), a silicone elastomer widely used in microfluidics and in bioengineering to realize soft micro-structured objects. In Figure IV.1.5 (a), the schematic of the fabrication process for both flat and circular configurations is presented. A PDMS precursor was first casted over polymer textured fibers. After PDMS curing, the PMMA was removed either by mechanically pulling out from PDMS, or by dissolving in appropriate solvent (for instance in acetone for PMMA fibers). This simple process results in textured PDMS films and more strikingly in PDMS micro-channels with textured inner surface as shown in Figure IV.1.5 (b). The inner diameter and pattern geometry can be simply tuned to dimension that is impossible to achieve with other existing technique so far. A further application of this microchannel texturing on microfluidic systems will be discussed further in section VI.1.

(a)   (b)
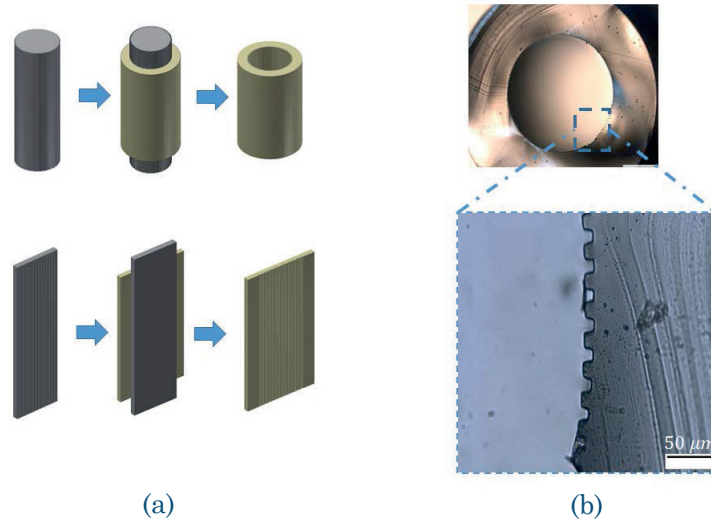
Figure IV.1.6: Fabrication of textured PDMS flat films and microchannels, (a) Schematic of fabrication procedure; (b) optical images of PDMS channe with a textured inner wall.

2. Characterization of Submicrometer Patterned Fibers

In the previous section, various SEM top-view pictures of patterned fibers were presented, as well as the cross-section of a 10 μm textured fiber. From these images, detail on the height and width of the final structure can be extracted. However, it turned out that it was much more challenging to do the same for the polymer structures with feature size of few micrometers or submicrometer. In order to characterize the surface of the fiber, several methods were employed during this thesis, which can be sorted into two categories: cross-sectional imaging, and 3D surface mapping. In this section, the principle and limit of each the techniques are discussed. The discussion, although being desirable to be as complete as possible, concerns mainly the techniques at our disposal during the thesis.

2.1   Cross-section Imaging

The choice of imaging method was naturally imposed by the limited resolution of our optical microscope, SEM (MERLIN and XLF30-FEG at CMI) was an obvious choice given its high resolution. Nevertheless, we faced many difficulties during our quest for a good cross-section preparation. The simplest method to create a fiber cross-section was to cut a fiber segment with a sharp razor blade. This method was practical, easy and the least time-consuming, and was

suitable when a lot of samples were characterized. On the other hand, it is not suitable for brittle materials, such as PMMA or in some regard PC, because the cut always left traces larger than several micrometers. Figure IV.2.1 shows a damaged cross-section created by cutting a PC fiber with a new razor. Although better image of the 5 micrometer-textured fiber was eventually achieved (Figure IV.1.2) by cutting the fiber in low temperature liquid nitrogen, we did not success to have the same resolution for submicrometer fibers.
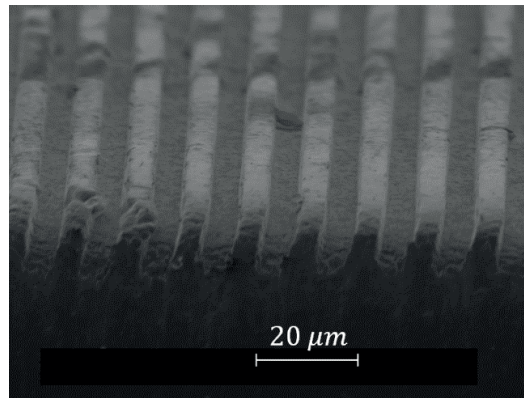
Figure IV.2.1: SEM image of a Cross-section of a textured fiber cut with a new rasor blade.

The second preparation method we considered was epoxy-assisted cutting. A textured fiber was dipped fully into a liquid epoxy, which cured into a solid form after a certain time, and was expected to protect the structure. There were however two main problems we encountered. First, the epoxy did not fill the structure before being cured, either because its viscosity was too high, or because its surface tension was too high to go deep in the submicrometer holes. Second, the contrast in SEM of the epoxy and the fiber was too faint for a high-quality image to be obtained.
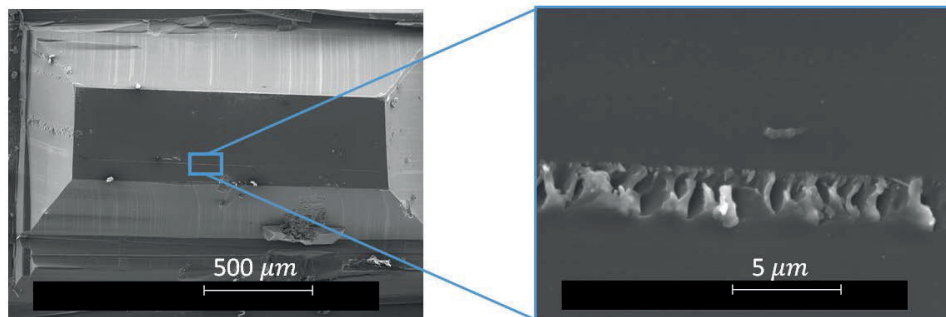
Figure IV.2.2: (left) SEM image of a fiber immersed in epoxy. The epoxy-fiber sample was cut into pyramidal shape. (right) zoom-in of the textured surface, deformed by the preparation

These two difficulties are highlighted in Figure IV.2.2, with a sample cut by a diamond microtome knife. For the future work, employing a low-viscous epoxy, and better configuring the SEM during imaging would possibly improve the quality of cross-section imaging.

Finally, the ion-beam polishing technique was employed. It consisted of cutting fibers extremely slowly by a power-tunable ion beam. A typical result is shown in Figure IV.2.3, with a cross-section of a patterned fiber with feature size less than $500\ nm$ prepared by ion-polishing overnight. Even in this long time configuration, the whole fiber was destroyed after the polishing at $-100^o C$ and with a beam voltage of $6\ kV$, and the image was taken on some section that remained. The feature of the cross-section clearly corresponded to a reflow, however, it was not possible to say if it came from the annealing during the draw or from the heating during polishing especially, considering the deformation of the baseline. Compared to other challenges previously stated, this difficulty was more fundamental and less technically-related, although it would eventually be possible to maximize the polishing parameters to remove the influence of the cutting technique.
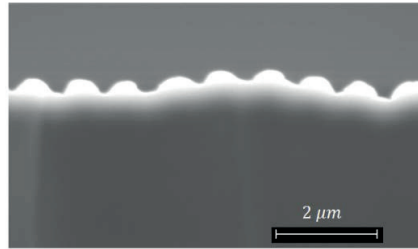
Figure IV.2.3: SEM image of a cross-section of a
sub-micrometer textured fiber cut by ion-polishing

2.2   3D Surface Mapping

In this approach, the idea was to map the 3D surface of the textured fibers, then extract the 1D profile to measure information such as the height and width of the structure. We consider two sub-categories, probe-based and contactless techniques.

Atomic force microscopy (AFM) is a probe-based technique based on the physical contact between a cantilever probe and the surface that is scanned over an area varying from few micrometers to several hundreds of micrometers. This very accurate and intuitive method, is much more suitable for low aspect-ratio structures, but not for our square-shape patterns. The main limitation was the pyramidal shape of the AFM probe, which was too big to fully scan the bottom of the structures, and which resulted in the sharp cone in Figure IV.2.4 of an AFM scan on a 5 μm textured fiber. A small and sharp AFM tip might give better image, but if the reflow was completely diminished, AFM is not an adequate technique for textured fiber surface characterization.

(a)   (b)
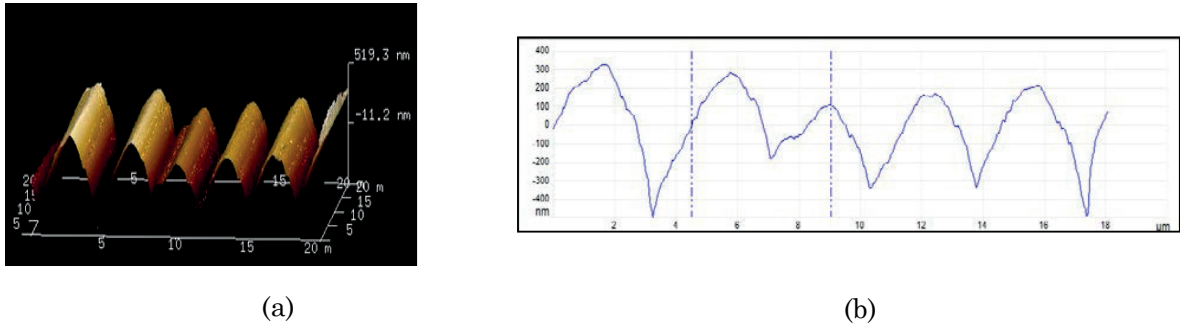
Figure IV.2.4: the result of an AFM measurement conducted on a textured fiber, with (a) a 3D reconstruction of the fiber surface and (b) an extracted profile.

The 3D mapping was also conducted by optical focus variation contactless profiler. In a scanning procedure, a textured fiber was fixed, and a microscope lens was set to have the best focus on its surface. Then the lens was moved up and down with regard to the fiber surface, and images were taken constantly as the focus was varied. Each image corresponded to a distance between the lens and the surface, and on an image, only sharp features, which were on focus, were kept to reconstruct a 3D scan of the textured surface. Figure IV.2.5 (a) and (b) shows the 3D reconstruction and the extracted profiles for two fibers with feature size of 10 μm and 1 μm respectively. While the 3D image of the 10 μm patterend fiber can be used to measured the depth and width of the periodic structure, such information was not available on the image of the 1 μm patterned fiber. In this method, the resolution on the xy-plan was limited, and the sharp edges

of fiber patterns could create considerable noise. As a consequence, this method is not completely adapted to characterize the surface of the submicrometer textured fibers.

(a)

(b)
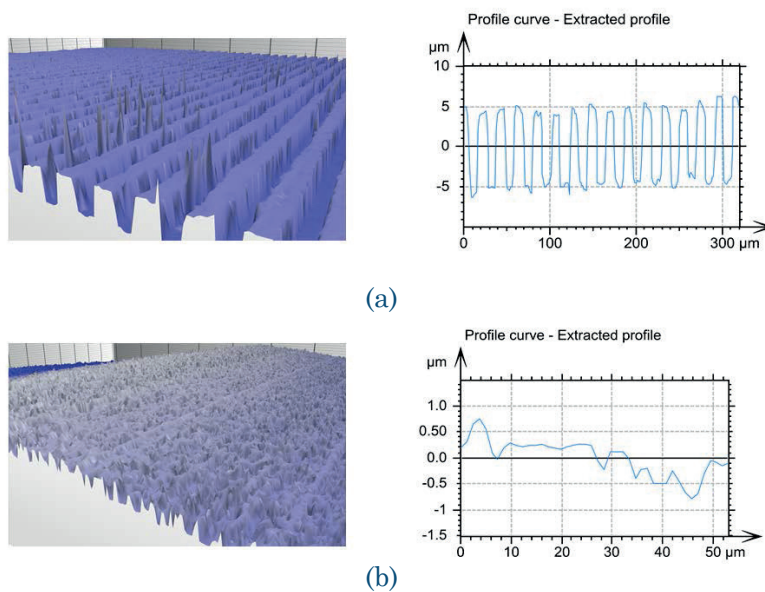
Figure IV.2.5: 3D reconstructed image and extracted profile
of (a) a 10 μm patterned fiber and (b) a 1 μm textured fiber.

In conclusion, characterization of the submicrometer surface textured has been challenging, and the optimal technique is still to be determined. Nevertheless, it is a positive challenge because it directly confirms the success of our technique to create sharp patterns on polymer surface at micrometer and submicrometer scale.

3. Applications of Patterned Fibers

The approach we propose constitutes a novel way to impart large area flexible surfaces with sub-micrometer scale controlled textures. It is also the first time that circular fibers and hence fabrics can be textured with such a high scalability and precision. In more general term, it is a unique technique to provide textures onto surfaces with very high curvatures. Such patterns are particularly interesting for a wide range of applications; for instance, tens of micrometers correspond to the size of biology cells, whereas the hundreds of nanometers correspond to typical visible wavelength. Thus, the realization of such patterns on fiber surface, both internal and external, could pave the way to novel utilization of fiber and textile beyond conventional usages. To highlight and discuss the potential of this technique, we demonstrate the opportunities that the textured fibers bring, we present in this section four applications where textured fibers and soft channels could be highly relevant.

3.1 Hydrophobicity Tailoring

Textures have a well-known effect on the hydrophobic properties of surfaces [51]. To study this effect on fibers and ribbons, we assembled together PC ribbons with a 5 μm texture on one side, and a smooth surface on the other. The comparison between water droplet deposited on each side of the same assembly is shown in Figure III.4.1. This approach enables us to rule out any effect of the roughness induced by non-perfect alignment between the fibers, as it is the same in

(a)

(b)
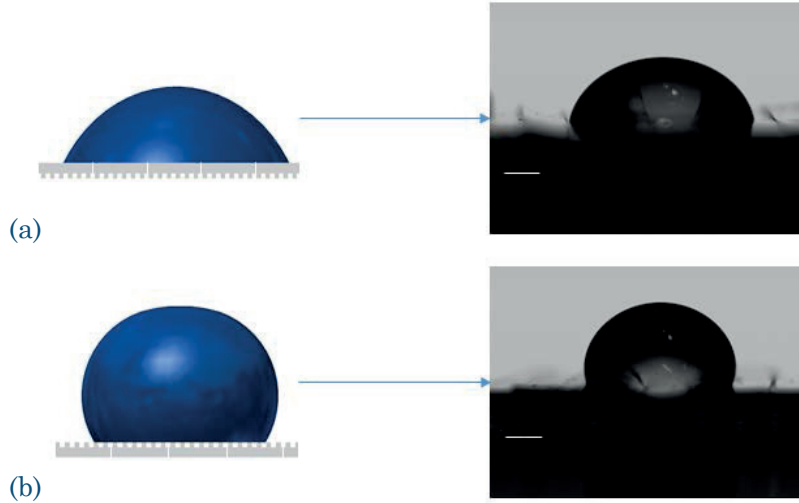
Figure IV.3.1: : Schematics and images of a water droplet on (a) flat fiber assembly and (b) on patterned fiber assembly.

both configurations. Contact angles, extracted using an OCA 34 Dataphysics Instruments with distilled water droplet, were 78° for the smooth side and 105° for textured surface fibers. Fibers and fabrics with controlled corrugated textures extending along their entire length could hence bring interesting and tunable hydrophobic properties.

3.2 Optical Grating

Here we investigate the diffraction pattern generated in transmission by ribbons with various texture sizes. Each ribbon was positioned at the center of a rotating stage and illuminated by a monochromatic beam from a supercontinuum source (Supreme K from NTK Phonics). A detector was positioned at the periphery of the stage and measured the optical intensity in far field at every degree between -60° and 60°. The angular distribution of the diffracted pattern was established (Figure IV.3.2) and the angle of the first-order peak was extracted. In the graph of Figure IV.3.2 we plotted the measured first-order angle versus texture size of four different textured fibers at illuminating wavelength of $600\ nm$, with the simulated value obtained from a FDTD code (Lumerical Solution) in red. The experimental values matched well with simulations, which reveals that the textures down to $500\ nm$ are well maintained and exhibit the expected optical properties.

(a)   (b)
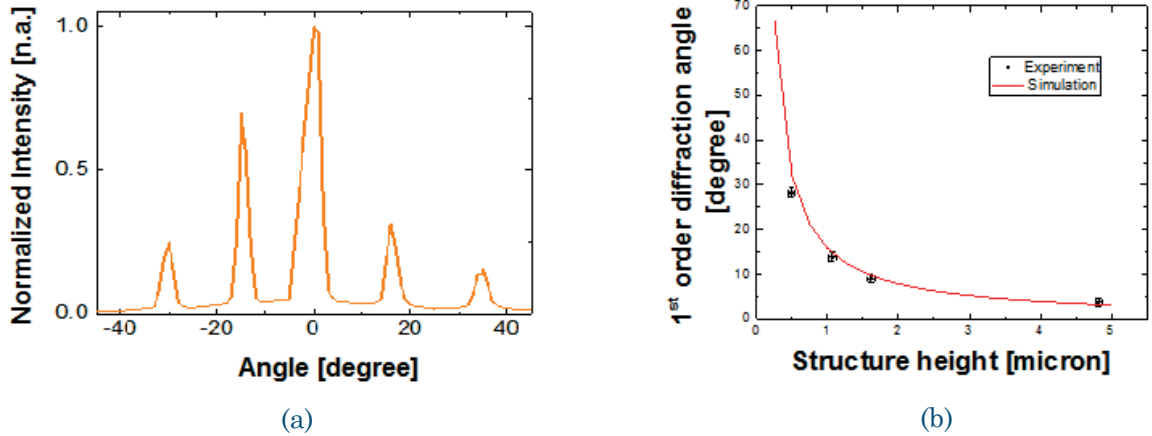
Figure IV.3.2: (a) a typical angle dependent diffraction pattern for a 600 nm coherent light on $1\mu m$ textured PMMA fiber. (b) graph of the first order diffraction angle versus the squared texture periodicity of a textured ribbon. The points represent experimental data with an error bar associated with the error on the angle measurement and the orientation of the ribbon with respect to the source.

In Figure IV.3.3, we show the reflection of an incandescent light beam on a fiber array with 500 nm texture. The left and middle images were taken on the same assembly with a different angle of illumination, while the right image shows the reflection on a woven array. This highlights the potential of submicrometer textured fibers and ribbons to tailor optical properties of large-area and flexible surfaces and textiles.
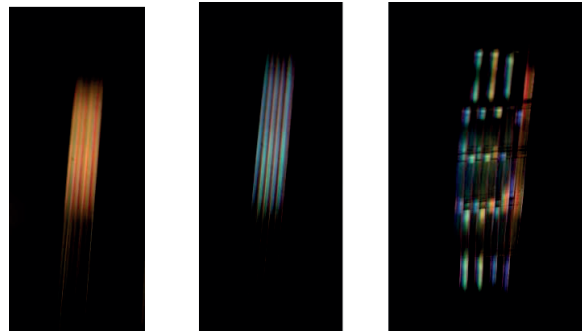

Figure IV.3.3: incandescent-light reflection on 0.5 µm surface-patterned assembled fibers with different angles (left and middle) and on a woven fiber arrays (right).

3.3   Cellular Alignment on Textured Surfaces

Substrate topography can also be used to control cell behavior[52,53]. To date, photolithographic techniques borrowed from the microelectronics industry allowed for the fabrication of patterned surfaces. Using patterned PC fibers, we prepared a range of surfaces with parallel square grooves with the period being twice as large as the width of each groove. Four groove sizes were considered: 10 μm, 5 μm, 1 μm and 0.5 μm; in addition, a flat PC fiber was used as reference substrate, on which adipose-derived stem cells were growth. As shown in Figure IV.3.5, the cell behavior was remarkably affected by the surface patterns. On the control flat substrates, the cells adhere to the surface through several focal adhesion points distributed homogenously across the cell, without any orientation (Figure IV.3.5 (a)). Grooved patterns in the range of 5-10 μm resulted in alignment of the cells along the pattern's direction (Figure IV.3.5 (b)), with the cell nuclei elongating into the groove. Small pattern-size substrates (0.5 μm and 1 μm grooves) induced an alignment of cell features, such as focal adhesion and actin fibers (Figure IV.3.5 (c)) as the cells were able to stretch along the pattern's direction. Moreover, a disparate characteristic in terms of cell area was observed: cells grown on a large-groove arrays were significantly smaller than cells grown on narrow-grooves array (***p<0.001) and displayed a more homogeneous size distribution.
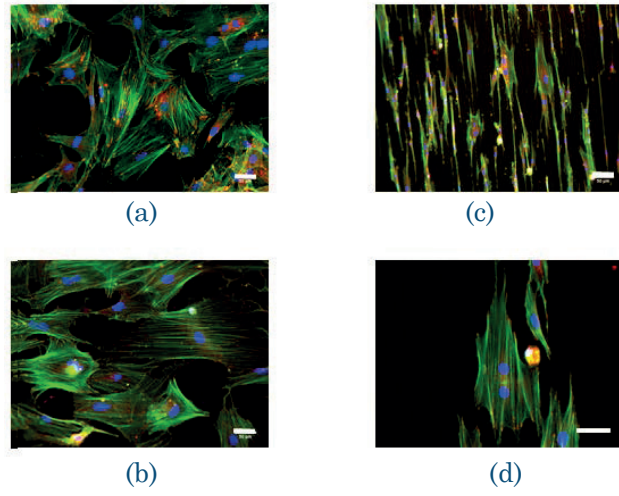
Figure IV.3.4: a–c) confocal images of adipose-derived stem cells cultured for 3 d on PC substrates (green, phalloidin; red, focal adhesions; blue, DAPI) (scale bar: 50 µm) (a) flat fiber, (b) 1 μm patterned fibers and (c) 10 μm patterned fiber; (d) Cell division along a 10 µm groove-size substrate (scale bar: 25 µm).
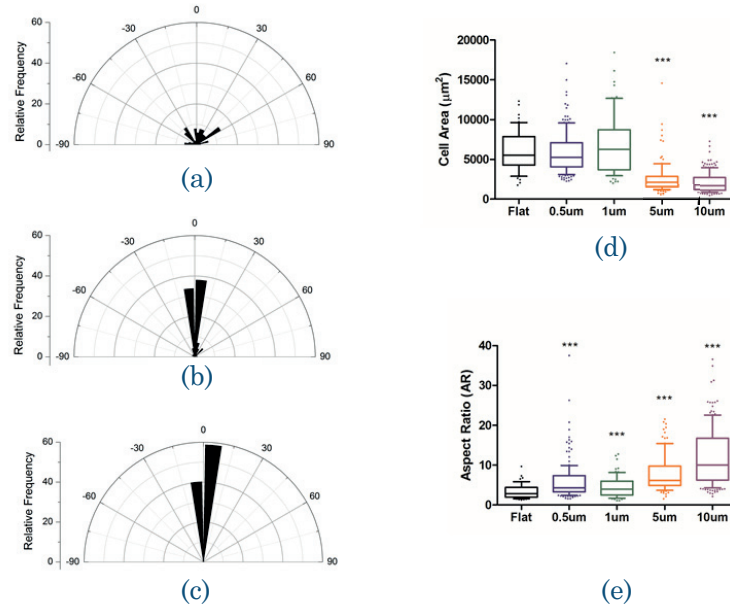
Figure IV.3.5: **Statistics of shape and orientation of cells grown on different fibers.** (a) (b) (c) Relative frequency of cell orientation grown on flat fiber, 1 μm patterned fiber and 10 μm patterned fiber respectively. (d)(e) distribution of surface area and aspect-ratio of nuclei on fibers of different feature-size pattern.

Similar effects were also seen for cell nuclei, as shown in Appendix 3, with more remarkably distinction between small and large textured fibers. On fibers with 10 μm patterned fibers there was clear preferred orientation of nuclei, which was hardly seen with 1 μm patterned fibers. The nuclei size was sharply smaller and their distribution was more homogeneous on large patterned fibers, while only a slight influence of pattern's size on aspect ratio was observed, as the larger the pattern's size, the more cells elongated. The micrometer and submicrometer patterning technique presented in this work can extend easily to other biocompatible and even biodegradable polymers, which brings great opportunities in cell culturing or even smart textiles with advanced biology functions.

3.4   Axonal Guidance in Dorsal Root Ganglia Explant

Patterned surface could also exhibit guidance effect for axonal growth in DRG explant. To access this feature, we cultured dorsal root ganglia (DRG) explants up to 6 days on sheets of textured PDMS membranes. The latter were first molded against parallel PC fibers with groove dimension of 0.5 μm and 5 μm bonded together to form a large surface area of several cm^2. As expected, neurites sprouting from dorsal root aligned along the grooves, independently on their depth and pitch.

Next we formed a hollow cylinder with a textured inner surface using a patterned PC fiber. A DRG was seeded at the entrance of the cylinder and we monitored neurites' sprouting from a DRG explant within the tube. Neurites grew orderly within the fiber and along the grooves. The effect of patterned substrates on cell behavior has been previously reported [33,54] but our drawing process allows the production of substrates and tubes textures with high reproducibility and resolution, over extended lengths of fibers and ribbons. We can also reach submicrometer feature sizes that could be associated with beneficial effects on cell growth and regeneration. Furthermore, as stated previously, our process may be extended to a wide range of polymers, from transparent to stretchable or biodegradable materials, enabling novel opportunities for imaging, or studying the effect of the substrate's mechanical properties. We therefore anticipate this technique will offer unique opportunities in bio- and neural engineering, both in the context of *in-vitro* studies and *in-vivo* regenerative strategies.
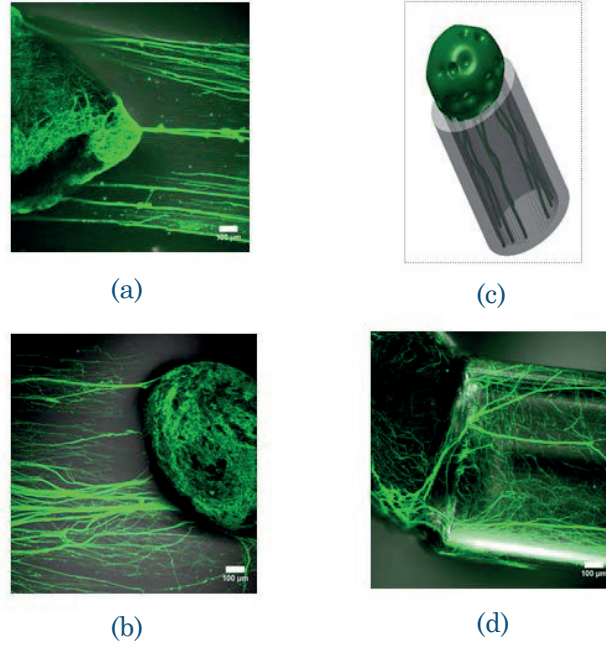
Figure IV.3.6: Growth of dorsal root ganglions (DRG) on flat and textured substrates. (a) and (b) Confocal images of DRG explants PDMS patterned substrates casted on thermally drawn patterned ribbons (green = ß -tubulin), scale bar: 100 µm : b) 0.5 µm groove-size pattern, c) 5 µm groove-size pattern; (c) schematic of DRG explants growing through a textured hollow conduit (1 mm diameter); (d) DRG growing through a hollow-core PC conduit with internal patterned surface of 5 µm (scale bar: 100 µm).

4. Summary

We reported in this chapter the straightforward and scalable fabrication of submicrometer structures on 2D surfaces or 3D structures such as hollow channels, made of different polymer fibers and ribbons using the preform-to-fiber thermal drawing technique. We combined for the first time soft lithography approaches at the preform level to create patterns at the tens of micrometers scale, with the thermal drawing process to scale down these initial patterns into submicrometer corrugated textures that extend over kilometers of fiber length. To overcome the thermal reflow responsible for the collapse of smaller scale patterns, we covered the structured polymer by a sacrificial layer in order to drastically reduce the interfacial tension that drives the reflow. Patterns down to a few hundreds of nanometers feature size were for the first time

obtained on ribbons and fibers, two orders of magnitude below what has been previously demonstrated in literature. To highlight the effect and opportunities of our approach, textured fibers were deployed to create enhanced hydrophobicity surfaces, to make fiber assemblies with optical effects, or used as templates for the growth of biological cells where a clear effect of the periodic pattern was observed in their alignment and growth. Textured fibers were also used as molds to fabricate PDMS constructs with hollow channels having textures on their inner surfaces. This represents an original and unique approach to fabricate submicrometer textures onto surfaces with very high curvatures for which current patterning techniques are not adapted. Such patterned micro-channels can be used in a myriad of applications in the physical and life sciences. We have shown how the neurites from a DRG explants could grow orderly, paving the way towards novel nerves or neurons regeneration scaffolds, bio-sensing and tissue engineering opportunities. Other applications can be envisioned for example in microfluidics, where channels with textures can mold the flow of liquid or nanoparticles in novel ways. New fiber probes with advanced microfluidic architectures can also impact current diagnosis and treatment strategies. Our approach hence enables the manufacturing of complex submicrometer textures within unconventional fibers, ribbons and micro-channels, at the simplicity, scalability and cost traditionally associated with optical fibers.

Cross-sectional Preservation and Case Study on Touch-Sensing Fiber Devices

1. Introduction

The preservation of cross-sectional architecture has been the key attribute and the main challenge in the fabrication of photonic crystal fibers and multimaterial fibers via the thermal drawing technique. With a perfect cross-sectional preservation, the functionality of the drawn fibers is designed at the macroscopic level within easily-made preform. With a judicious choice of drawing parameters, the functionality is then achieved when the diameter of the fiber reaches micro- or nano-dimension. Striking examples for this strategy are the fabrication of photonic crystal waveguide fiber with air hole of 25 nm [4], and the fabrication of photo-detecting fiber with 8 distinguished nanoscale devices integrated in a single fiber [8]. This strategy is also found in a variety of photonic crystal fibers [55–58], or in thermal sensing, chemical sensing and acoustic sensing multimaterial fibers [10,13,14] . This remarkable attribute comes from the interplay between the viscosity and surface tension during the draw. Depending on materials and architectures of the preform, this interplay would be limited in a window of drawing parameters in which the initial cross-section would be preserved, and outside of which hole collapse, structure reflow, and even capillary breaking up would happen. The extreme cases of non-preservation have received a great deal of attention so far, with experimental and theoretical studies being developed in great details [59] [60] [29]. Remarkably, the breaking up of sheets and filaments due to Plateau-Rayleigh instability has been so well-known that it becomes a mechanism of the fabrication of nanowires, nanorods and nanospheres [28,61,62].

Although these works treated the deformation of fiber structure in widely disparate configuration, a common time constant emerges, proportional to the viscosity and fiber feature size, and inversely proportional to the surface tension of preform material:

$$\tau \sim \frac{\eta \times \lambda}{\gamma}$$

This time constant gives an idea of the breaking up or reflow time scale of the cross-sectional structure. It is also suggested that if the drawing time is significantly smaller than this time constant, the cross-sectional structure would most likely be preserved. In this chapter, we present first a quantitative discussion on the cross-sectional deformation time scale and on how to obtain it experimentally. In the second section, we present as case study the making of cantilever-like touch-sensing fibers with a free moving functional domain. This work resulted in the publication "Multi-Material Micro-Electromechanical Fibers with bendable functional domains", published in Journal of Physics D, 2017 [30].

2. Cross-sectional Deformation and its Time Scale

In this discussion of cross-sectional deformation, we consider two main mechanisms associated to the deformation of the fiber cross-section: the breaking up of sheets and filaments due to Plateau-Rayleigh capillary breakup, and thermal reflow deformation. While the latter is treated for the first time in detail in this thesis (Chapter III), the former has been the subject of stimulating research for years. The Plateau-Rayleigh breaking up in fiber was observed when researchers at M.I.T wanted to achieve thin chalcogenide glass layers. Instead of having continuous films in the fiber, they only obtained arrays of filament; and a following in-depth study on the phenomena showed that the capillary break-up was a fundamental challenge for such purpose [61]. In a remarkable turn of events, this study laid a strong foundation for the fabrication of nanostructure of metals, semiconductors and polymers using thermal drawing technique, one of the most exciting topics in the field recently. The Plateau-Rayleigh instability in drawing process is in some respect similar to the breakup of a water jet from a tap. As a fluid gets thinner, there is an enhancing effect of perturbations due to the Young-Laplace pressure that would eventually break the continuous streams or filaments into droplets. The energy of such perturbations however could be dissipated by damping effect of the viscosity, which would lead to a slowing down, or even suppression of the breakup. Beyond this too simplistic reasoning,

mathematical development showed that there was a breakup time scale depending on viscosity and surface tension of the drawing material, and if the dwelling time of fiber drawn is smaller than this time scale, the capillary breakup would not happen. This time scale can be written simply as:

$$\tau_{capillary} = C_{capillary} \frac{\eta \lambda}{\gamma}$$

with η the viscosity and γ the surface tension of materials, λ a geometry parameter associated with fiber's feature size and $C_{capillary}$ a constant. The full expression of $C_{capillary}$ and its mathematical development can be found in the reference [61].

Similar to capillary breakup, the reflow deformation presented in the Chapter III is also driven by the surface tension of polymers, and slowed down by their viscosity. Moreover, reflow happens faster as the feature size on fiber gets smaller. In a simple manner, the timescale for such deformation is written as:

$$\tau_{reflow} = C_{reflow} \frac{\eta \lambda}{\gamma}$$

The constant associated with the reflow deformation obtained previously is $C_{reflow} = \frac{1}{\pi}$.

Since the interplay between viscosity and surface tension in both situations above is expressed in similar relation, we suggest a universal time scale τ as a characteristic time of a general deformation for a quantitative analysis of cross-sectional preservation/deformation of a drawing process. If the drawing time is significantly longer than this characteristic time, the structure will likely subject to deformation; on the other hand, if the drawing time is much smaller than the characteristic time, there would be likely a preservation of the cross-section from the preform to the fiber.

Before presenting the calculation of the deformation time scale, we consider several examples of extreme deformation and perfect preservation of the cross-section during fiber drawing. Figure V.1.1 illustrates a "perfect" deformation for a draw of a soft matter. This particular material has a very low viscosity at the drawing temperature, which result in a low characteristic time. Four images of V.1.1 show the evolution of the cross-section during the draw. The initial preform had a rectangular cross-section with a hole in the middle (image V.1.1 (a)). The hole got smaller along the drawing direction ((b) and (c)) and completely disappeared in the fiber (d). Moreover, the rectangular shape also got more and more rounded, and this rectangular

preform became finally almost a circular fiber at the end of the draw. Another example for the cross-sectional deformation could be seen in the reflow of textured PC fiber in Figure II.4.2., or the intended breakups for nanofabrication purpose in the reference [28]. On the other hand, it is a lot easier to find examples of a perfect preservation because nearly only fiber-based devices with quasi perfect preservation of the cross-section get published. It is the case for instance of photo-detecting fibers [63], chemical sensing fiber [14], fiber capacitors and the micrometer textures fibers [29].

Figure V.2.1: The evolution of a hollow-core rectangular preform into circular solid fiber when the processing time is higher than the deformation time constant: (a) image of one corner of the preform with a circular hole in its center, (b) and (c) cross-section of the neck-down near the preform and near the fiber respectively, (d) the final circular and solid core fiber.
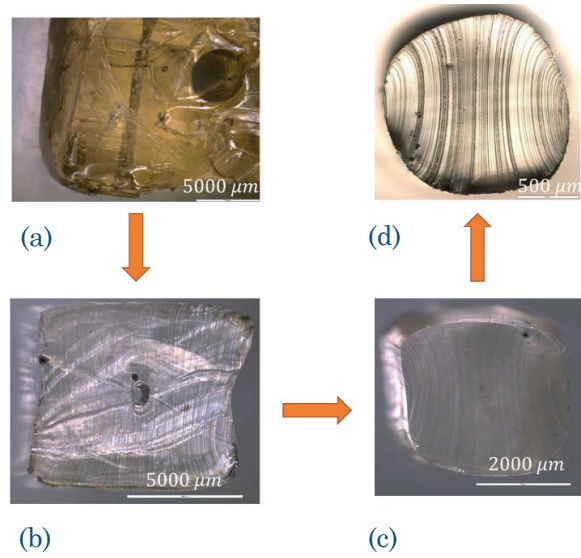
The neck-down deformation is a dynamic process where the viscosity, surface tension and fiber feature size change constantly along the z-direction: $\eta = \eta(z)$, $\sigma = \sigma(z)$ and $\lambda = \lambda(z)$. Hence the deformation time constant is also a dynamic variable $\tau = \tau(z)$. As the time constant is well defined at each local position in the z-direction, we propose a method to estimate the average time constant for a whole drawing process.

Let us consider again the schematic of a draw in Figure IV.1.2 with the neck-down region highlighted in red. Although the structure goes from the top of the furnace ($z = 0$) to its end ($z = L$), it is only in the neck-down region that the deformation is significant, as the temperature is higher than the glass transition temperature of the preform. In the z-direction, this region extends from the position $z = z_1$ to the position $z = z_2$. The processing time, defined as the time it takes for one point in the preform to go from z_1 to z_2, is calculated directly as:

$$t_{processing} = \int dt = \int_{z_1}^{z_2} \frac{dz}{v_z(z)}$$

[Eq. V.2.1]

where $v_z(z)$ is the velocity of the preform along the drawing direction.
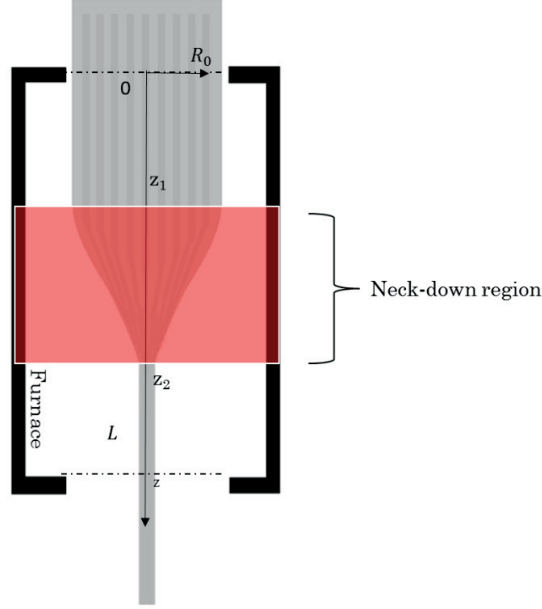
Figure V.2.2: Schematic of the drawing with neck-down region highlighted in red.

The deformation time constant of the whole process τ_{tot}, on the other hand, is defined as a weighing function of local deformation time constant along (z_1, z_2):

$$\tau_{deformation} = \frac{\int \tau(z)\,dt}{\int dt} = \frac{\int_{z_1}^{z_2} \tau(z)\dfrac{dz}{v_z(z)}}{\int_{z_1}^{z_2}\dfrac{dz}{v_z(z)}}$$

[Eq. V.2.2]

With an analytical expression of the velocity profile $v_z(z)$ that can be obtained semi-empirically (see section II.2), both the processing time $t_{processing}$ and the total deformation time constant $\tau_{deformation}$ can be calculated using expression [V.2.1] and [V.2.2]. However, the velocity profile is not always accessible in a formal expression, since it might require heavy calculation. Fortunately, there is an empirical method to go around such difficulty simply based on the assumption of volume conservation. The latter states that the flux of material is a constant along the drawing direction, or the product of velocity of a cross-section and its surface is a constant:

$$v_z(z) \times S_z(z) = constant$$

[Eq. V.2.3]

Let us define $R(z)$ the diameter of the fiber, then $S(z) \sim R(z)^2$, which leads to:

$$v_z(z) \times R(z)^2 = constant$$

[Eq. V.2.4]

At $z = 0$, $v_z(0)$ is value of feeding speed v_f and $R(0)$ is the initial size of the preform It is hence possible to extract the velocity profile from the experimental shape of the neck-down region as following:

$$v_z(z) = v_f \left(\frac{R(0)}{R_z(z)} \right)^2$$

[Eq. V.2.5]

Moreover, the integral IV.1.4 and IV.1.5 can also be written in discrete form. By dividing the zone (z_1, z_2) into N segments, these integrals become:

$$t_{processing} = \sum_i t_i = \sum_i^N \frac{\Delta z_i}{v(z_i)}$$

[Eq. V.2.6]

$$\tau_{deformation} = \frac{\sum_i \tau_i \, t_i}{\sum_i t_i} = \frac{\sum_i^N \frac{\eta(z_i) \lambda(z_i)}{\gamma(z_i)} \frac{\Delta z_i}{v(z_i)}}{\sum_i^N \frac{\Delta z_i}{v(z_i)}}$$

[Eq. V.2.7]

The equations V.2.6 and V.2.7 enable to estimate the processing time and deformation time constant from the experimental shapes of the neck-down region, the rheology measurement of viscosity, the dependence of surface tension on temperature, and a precise calibration of the temperature inside the drawing furnace. By comparing these empirical value of $t_{processing}$ and $\tau_{deformation}$, one could evaluate the possibility of creating new structures from known materials, or the possibility of maintaining the cross-section while drawing new materials.

It is important to note that the values of processing time $t_{processing}$ and deformation time scale $\tau_{deformation}$ in V.2.6 and V.2.7 depend on the arbitrary choice of the neck-down region (z_1, z_2) and also on the real temperature profile of this region. For this reason, the model is valid when two values differ by at least one order of magnitude. If on the other hand the values of $t_{processing}$ and $\tau_{deformation}$ are too similar, it is not possible to confirm the cross-sectional preservation.

Nevertheless, the analysis described above provides a simple and intuitive insight on the deformation of the fiber cross-section during thermal drawing process. To prove the validity of this theory, in the next section, we show an example of a fiber with a novel cross-sectional structure that integrates a movable domain.

3. Micro-Electromechanical Fibers for Pressure-sensing Device

Thus far, all novel fiber designs of the emerging multimaterial fiber platform have relied on materials organized in intimate contact to deliver a specific functionality. The concept of electromechanical transduction from freely moving functional domains within multi-material fibers has not yet been exploited. This approach is used in a myriad of configurations in micro electromechanical system (MEMS) technology such as cantilever-based devices for micro-sensors and actuators. The ability to integrate such advanced systems within extended length of flexible fibers can bring a breath of novel opportunities for functional fibers and fabrics. Here, we demonstrate for the first time a micro-electromechanical fiber (MEMF) that exploits the bending of a freestanding electrically conductive polymer sheet. Using the analysis of cross-sectional preservation presented in the previous section, we show that the drawing time is one order of magnitude smaller than the deformation time scale, assuring that the freely moving part of the device would not be collapsed during the draw. Once successfully made, the MEMF device demonstrated the capacity of detecting and localizing a pressure point along the entire fiber length with sub-millimeter resolution. Beyond the simplicity and scalability of the fabrication process, MEMF devices are the first one-dimensional piezo-resistive systems that can sense pressure and touch without the need for 2D grids, at very low energetic consumption, and with such a high resolution. This paves the way towards novel advanced fibers and fabrics capable of functionalizing large area surfaces and textiles with pressure mapping capabilities.

3.1 Fiber fabrication of a MEMF device

The fabrication process of a MEMF device and the cross-section of a fiber are shown in Figure V.3.1. First, a thermoplastic plate, here polysulfone (PSu) was machined in a L-shape cross-sectional structure (Figure V.2.1(a-i)). For the conducting material that will deliver the desired electronic function, we chose a carbon black loaded polycarbonate composite (cPC). cPC has been utilized for its electrical conductivity and, in particular, its linear resistance, as well as for its compatibility with the thermal drawing process [22]. Indeed, the thermoplastic matrix of polycarbonate ensures the compatibility with the thermal drawing process, while carbon black fillers provide percolated paths for sufficient electrical conductivity. A cPC bus was placed on the long edge of the L-shape PSu, while a thin cPC sheet is positioned above it on the short edge as shown in Figure V.2.1 (a-ii) and a Teflon plate was put in under the top cPC plate to prevent it from touching the bottom part. The whole structure was hot-pressed to consolidate all parts. After the preform was consolidated, the poorly adhered Teflon was mechanically removed, leaving the final preform, shown in Figure V.2.1 (a-iii).
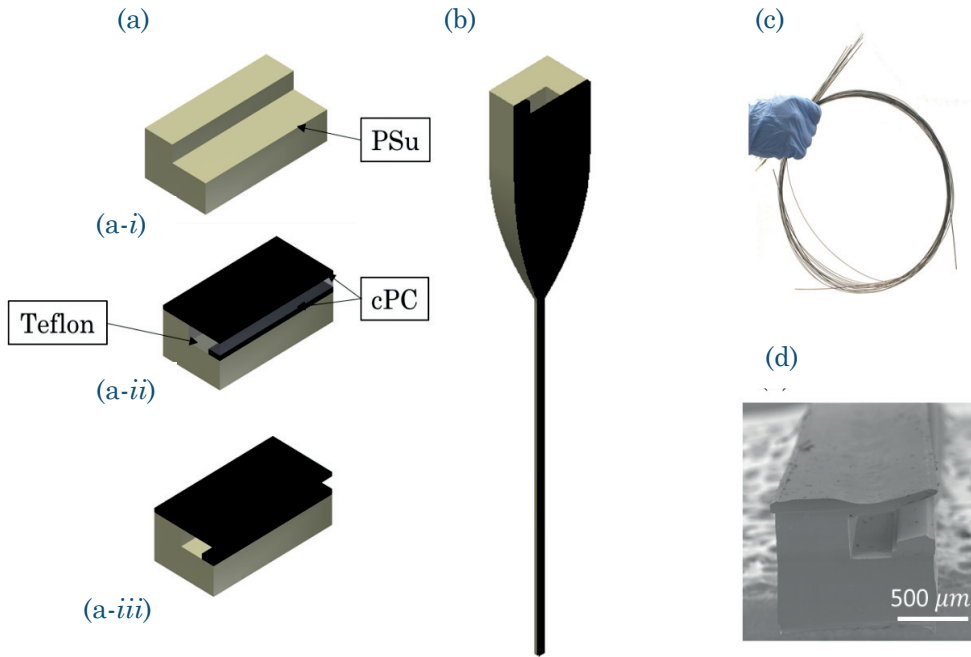
Figure V.3.1: Fabrication of a MEMF device: (a) Preform fabrication steps: *i)* machining of a PSu plate in a L-shape block, *ii)* assemble of cPC sheet and bus using thermal welding, a Teflon plate was inserted to keep the sheet from deforming, *iii)* removal of the Teflon plate; (b) Schematic of the preform-to-fiber thermal drawing; (c) photo highlighting the length of the fibers; (d) SEM image of the cross-section of a touch-sensing fiber

The preform was subsequently thermally drawn into fiber, illustrated in Figure V.2.1 (b). The drawing temperature of the middle zone was set at 260^oC that insured the co-drawing of both PSu and cPC; feeding speed was set at $1\ mm/min$ and drawing speed was set between $0.1\ m/min$ and $1\ m/min$. The drawing resulted in extended length of flexible thin ribbons, that maintained the shape of the initial preform cross-section, as shown in Figure V.2.1 (c) and (d). The SEM image was taken with a Zeiss Merlin field emission SEM (Zeiss, Gottingen, Germany).

3.2   Cross-sectional preservation analysis

We calculate in this section the processing time and the deformation time scale for a MEMF preform-to-fiber drawing. Figure IV.2.2 shows a picture of a preform-to-fiber, obtained by interrupting the draw. The neck-down region can be easily identified as the zone between $5\ cm$ and $11.5\ cm$ on mark the ruler (highlighted in red); the tip of the structure is slightly bent due to an elastic bounce back when the fiber was cut.

The discrete expression of the processing time and the deformation time constant in equation V.2.6 and V.2.7 can be written with all measurable parameters:

$$T_{processing} \quad = \sum_i t_i = \sum_i^N \left(\frac{R(0)}{R_z(z)}\right)^2 \frac{\Delta z_i}{v_f}$$

[Eq. V.3.1]

$$\tau_{deformation} = \frac{\sum_i \tau_i\, t_i}{\sum_i t_i} = \frac{\Sigma_i^N \frac{\eta(z_i)\lambda(z_i)}{\gamma(z_i)}\left(\frac{R(0)}{R_z(z)}\right)^2 \frac{\Delta z_i}{v_f}}{\Sigma_i^N \left(\frac{R(0)}{R_z(z)}\right)^2 \frac{\Delta z_i}{v_f}}$$

[Eq. V.3.2]

Image IV.2.2 was taken in high-resolution camera Canon Kiss X3, and the ruler next to the preform served as scale-bar. A grid was added into the picture in order to measure the size of the preform along its length to extract the function $R(z)$, which was done using the software ImageJ.
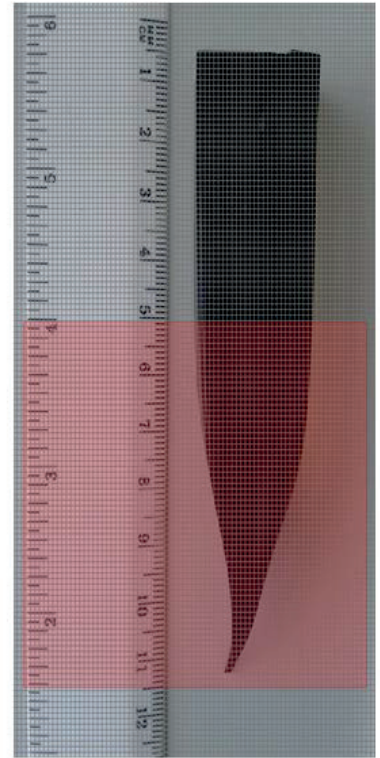

Figure V.3.2: Image of the preform-to-fiber region in the drawing of the MEMF device.

With the $R(z)$ obtained with this method, we estimated the drawing time:

$$t_{processing} \approx 10^3 \ (s)$$

[Eq. V.3.3]

For the analysis of the deformation time constant, we considered the deformation of cPC top plate with an initial thickness $\lambda(0) = 2 \ mm$, while its viscosity was obtained from rheology measurement with a Rheometer AR2000 (TA Instrument) using a flow procedure with shear rate being set at $2.5 \ s^{-1}$ and temperature varying from $220^o C$ to $280^o C$. The rheology measurement resulted in the following empirical expression of viscosity as: $\eta_{cPC}(T) =$ $\exp\left(\frac{13681}{T+273.15} - 15.69\right)$, with T is the temperature in degree Celsius. The surface tension of cPC was set at $41.2 \ N.m$ as of pure PC and its dependence on temperature was neglected. The temperature profile was $T(z) = 230 - 14300 \ z^2$ around the maximum temperature, with z is the distance in $meter$.

Insert these functions into the expression above, we obtained a deformation time constant:

$$\tau_{deformation} \approx 10^4 \ (s)$$

[Eq. V.3.4]

The deformation time constant is one order of magnitude higher than the processing time, in other words, the time scale associated with any reflow and break-up of cPC domain is greater than the time it takes to go from the preform into the fiber. It means that reflow and capillary break-up do not have time to occur, insuring that at these length-scales the cross-sectional architecture was maintained. Combining with the successful draw of the MEMF device, this brings a strong proof of validation for the analysis presented in the previous chapter.

3.3   Features of the MEMF device

The working mechanism of the MEMF device is shown in the schematic V.3.3 (a). In the MEMF device, the two cPC domains are clearly visible, separated by a micro-cavity that allows the thin upper cPC sheet to bend when a pressure is applied, then recover its initial horizontal position upon removal of the mechanical excitation. As the cPC layer touches the cPC bus underneath, an electrical connection is created and a current can flow from one cPC domain to the other, signaling the local pressure. The electrical current generated depend on the position when the pressure is applied, since the cPC film and bus act as linear resistors, and the further

away from the applied potential, the higher the equivalent resistance of the circuit. Indeed, for an equivalent circuit of the MEMF presented in Figure IV.3.5 (b), corresponding to a potential applied V_0 at a position $x = 0$, the pressure located at point x, we have the following expression:

$$\frac{V_0}{i_0} = x\, \rho_{cPC} \left(\frac{1}{S_f} + \frac{1}{S_b} \right)$$

[Eq. V.3.5]

with S_f and S_b are the cross-sectional surface of the cPC film and bus respectively.

(a) (b)
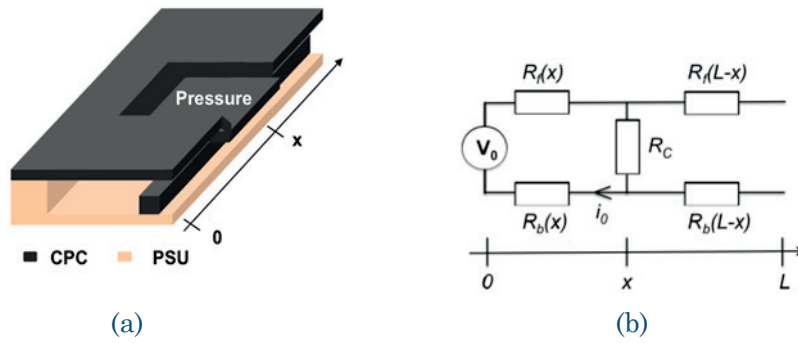
Figure V.3.3: Pressure detection and localisation. (a) schematic of a pressure sensing ribbon with a local pressure bending the top cPC film at position x; (b) schematic of the equivalent circuit when a potential is applied at one fiber end and a pressure is applied at a position x along the fiber length.

In order to have more precise detection and localization of the pressure, another voltage is applied on the other end of the fiber $x = L$. With this setup, the MEMF can detect and localize a pressure with a resolution lower than $1\ mm$. Moreover, the device showed no drift, change of respond nor damage after $10^4\ cycles$, and can detect multiple pressure points without being integrated in a 2D grid system. In addition, the MEMF is a highly energy efficient device because it only consumes energy at the presence of a mechanical exciton.

4. Summary

The preservation of the fiber cross-sectional architecture has been studied in this chapter. Based on previous works on capillary break-up and reflow deformation, we propose a universal time constant associated with the cross-sectional collapse, which is proportional to the feature size of the structure and the viscosity and inversely proportional to its surface tension. If the preform is drawn in a time much smaller than its proper deformation time constant, the cross-section of the preform would be likely to be preserved into fiber level. This simple rule of thumb could provide useful insight for further works in the future dealing with drawing of a new materials or creating complex structures in fibers. The work done in this chapter is then a direct continuation of the studies exposed in previous chapters, where the tailoring of the interfacial tension was to slow down the reflow time constant to a value much smaller than the dwelling time, and consequently allowed small texture to be preserved.

To validate this analysis, we studied the deformation time constant of a preform with freely moving domains in a specific drawing condition, and found that the analysis predicted the preservation of its cross-section, which matched with experiment result. From this preform, a novel micro-electromechanical fiber device (MEMF) was fabricated. We showed that the MEMF device could recognize and localize two pressure points with sub-millimeter resolution, was unaltered after 10^4 loading cycles at 200 Hz, and exhibited a respond bandwidth of close to 20 kHz. This highly flexible, robust and sensitive fibers represent significant opportunities for smart textiles and wearable electronics.

Chapter VI.

Microstructured Multimaterial Fibers as Building Block for Additive Manufacturing

Until recently, fibers have been used more for their collective effects rather than for their individual functionalities. The best examples of such assemblies can be found in the daily uses of textile where a large quantity of threads are woven into fabrics, or in polymer reinforcement where networks of fibers are immersed in a polymer matrix [64]. In these examples, the assembling techniques play an important role in adding new features beyond the fiber attributes, hence widen their range of applications. This leads to believe that functionalization via advanced assembling of previously functionalized multimaterial fibers would extend even further their scope of applications. This motivation is at the heart of the work presented in this chapter. Here, we introduce two new assembling methods based on additive manufacturing of thermally drawn fibers. In the first section, textured fibers are used as templates to construct complex microfluidic devices. In the second section, multimaterial fibers are employed as building block for a 3D printing-inspired process to create electronic touch-sensing panel. In each section, we will present the background of the work, the most recent results and the perspective for future developments.

1. Fiber-Template Fabrication for Microfluidic Systems

Microfluidics have attracted tremendous attention from both the academic and industrial communities for the last couple of decades. A microfluidic system relies on the precise manipulation of fluids in channels with dimensions ranging from tens to hundreds of micrometers. Numerous applications resulting from these features have been demonstrated, like fast medical diagnosis[65], high-throughput genetic scanning [66] and chemical micro-reactors [67]. It is believed that microfluidics still has not reached its full potential, and much more stimulating developments are waiting ahead [68].

So far, however, most of microfluidic devices are made with soft-lithography and PDMS-line. In a fabrication process, the channels are first created on a Silicon master, on which a liquid PDSM pre-polymer is poured to replicate the structure of the master. After curing, the polymer is peeled off and bonded on a flat surface, usually of glass, or PDMS itself to create a microfluidic device. Although, this technique enables the fabrication of complex structures and multiple channels in one device, its limitations are still numerous. First, although the replication of PDMS mold is easy and low-cost, the fabrication of Si masters requires expensive photo-lithography equipment; secondly, the size of Si master is restraint by the size of a typical Si wafer which is in range of tens of centimeters; and lastly, it is particularly complicated to apply this soft-lithography technique to fabricate 3D structure microfluidic systems. As a consequence, there is a need for a versatile and easy-to-make fabrication technique which bring complemental features to the current technology to overcome such limits.

In this thesis, we proposed to use micro-structured thermally drawn fibers, that seemingly have nothing to do with microfluidic systems, to address the challenge described above. The idea is to use smooth and patterned fibers as templates to construct a desired network within a casted PDMS matrix. The fiber-template network is subsequently dissolved in a suitable solvent to create a channel network for microfluidic devices. Compared to photo-lithography, the fiber-template fabrication requires significantly less equipment and less time, without limitation on channel length, cross-sectional complexity and dimensions.

Here, we first present the fabrication process of fiber-template microfluidic systems and various devices in the VI.1.1. In the following section, we remind the reader of the challenge in mixing for microfluidics, associated with a low Reynold number regime; and demonstrate the mixing enhancement in our devices. Finally, perspective for future development is discussed in the section VI.1.3.

1.1 Device making and Result

In general, the fabrication process can be separated into three steps: network fabrication, PDMS casting and fiber demolding. Depending on the desired applications, specific fibers were used to construct a network; the fibers could be rectangular or circular, flat or patterned, which could in turn be easily tuned by the drawing process described in the Chapter II. If junctions are needed, different segments of fibers were cut and glued by chemical joining; Figure VI.1.1 shows the schematic of two typical junctions that were employed in the subsequent experiment present in section VI.1.2., namely T-junction (a), Y-junction (b).

(a)   (b)
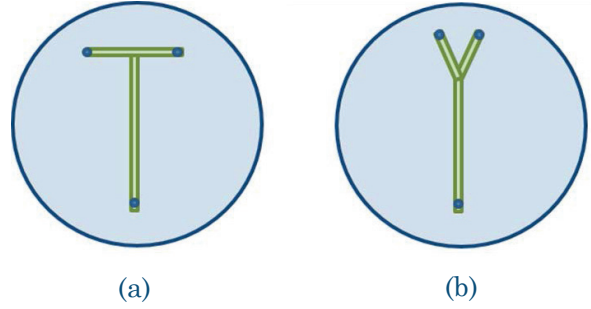
Figure VI.1.1: Schematics of junctions made from different fiber segments: (a) T-junction and (b) Y-junction.

Once the network was created, PDMS solution was cast covering the whole network. The PDMS is a mixture of a base polymer epoxy and a curing agent with a weight ratio 10:1. This non-crosslinked PDMS mixture was of low viscosity and flowed covering the fiber assembly, replicating exactly the shape of the fiber network. PDMS was then cured by heating in an oven at $80^o C$ for more than two hours, after which the PDMS became rubber-like solid, with an immersed polymer fiber network.

The demolding of PMMA fiber out of PDMS can be done either by mechanical removal or by chemical dissolution. In case of dissolution, small holes were punched in order to let the solution attack the fiber network; while with mechanical removal, a single opening end of the network was created, then each fiber segments were removed with a gentle force.

Figure VI.1.3 shows a typical fabrication process of a fiber-template microfluidic channel from a textured circular fiber. In this example, the mechanical removal was employed. It can be seen that not only the channel size was the same as the initial fiber size, but also the micro-pattern on the fiber was well replicated into PDMS.
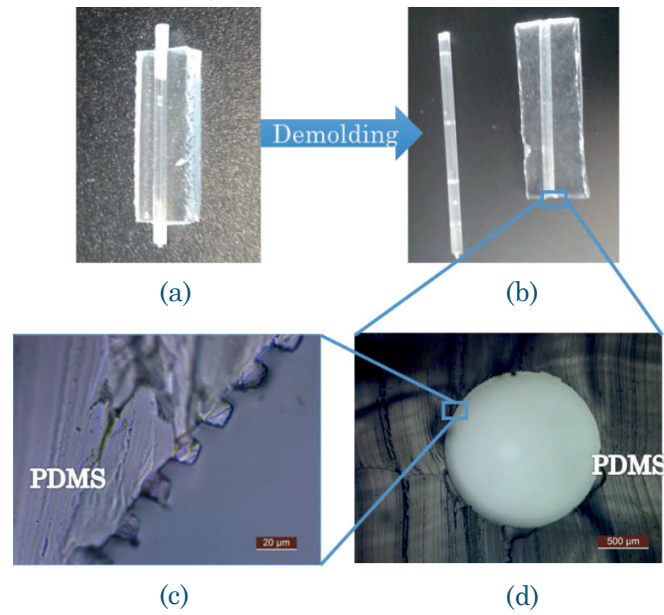
Figure VI.1.2: A typical process of making fiber-template fiber (a) PDMS casting around a patterned fiber, (b) demolding by mechanical removal (c) cross-section of the channel in PDMS (scale bar 500 μm) and (d) the zoom-in of the textured (scale bar 20 μm)

The cross-sections of rectangular channels in PDMS are showed in Figure VI.1.3. The initial fibers were made of PMMA, and the chemical removal was performed in acetone. Note that the swelling ratio of PDMS in acetone is only 1.06 [69], which allowed both big and small patterns to be replicated directly from the initial fibers. A dissolution in THF for example would result in a severe swelling of PDMS.
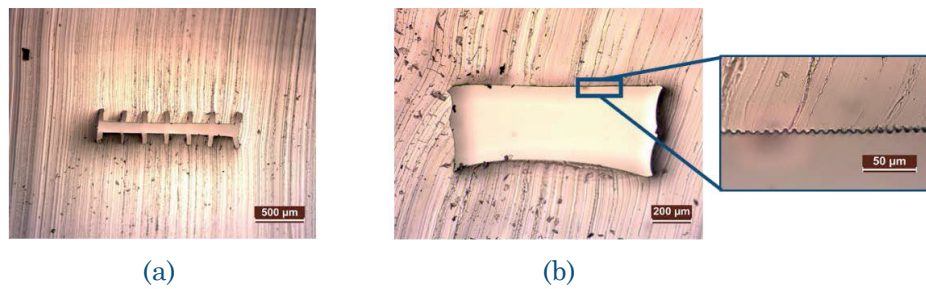
Figure VI.1.3: Cross-section of fiber-template microfluidic channels obtained from dissolution in acetone of patterned PMMA fibers (a) from large patterned fiber (scale bar 500 μm) (b) from small patterned fiber (scale bar 50 μm).

To prove the ability of our method to address the challenges previously discussed, microfluidic devices with more complex structures were created and are shown in Figure VI.1.4. Specifically, Figure VI.1.4. (a) demonstrates a twisted channel, filled with colored water, inside a microfluidic device; Figure VI.1.4 (b) presents a helix structure of a fiber (filled with blue water) surrounding a straight channel (filled with orange water); and Figure VI.14 (c) shows a device with 7 inputs and 1 output in a channel network that had the shape of EPFL logo. While the helix structure clearly demonstrates the potential of the fiber-template fabrication for 3D microfluidics, the EPFL device prove that the fiber-template technique is suitable to fabricate complex multi-input-output systems. In particular, we study in detail in the following section VI.1.3 the use of the twisted channel in mixing enhancement. Note that while rectangular textured channels can still be obtained by current soft-lithography technique through several additional steps, so far there has not been any report on the fabrication the circular textured channels, twisted channels or helix structures with the conventional method.

(a)

(b)   (c)
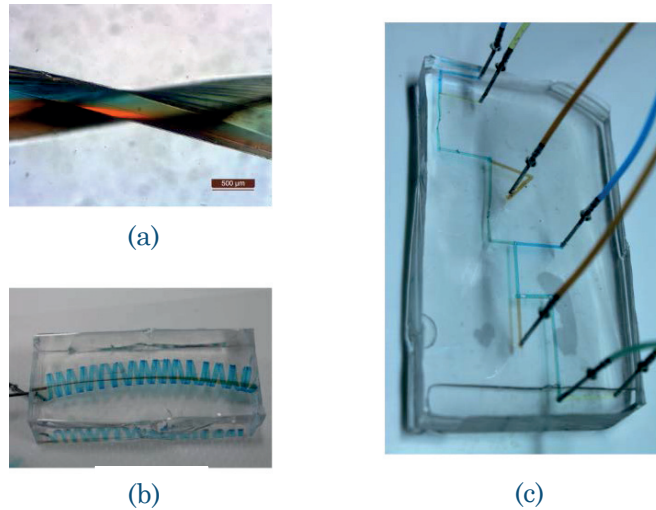
Figure VI.1.4: Several Microfluidic devices obtained by fiber-template fabrication (a) twisted channel, (b) 3D helix structure, (c) EPFL-shape with 7 inputs and 1 output.

1.2   Mixing Enhancement based on the Fiber-Template Twisted Channels

1.2.1   Challenge in Mixing for Microfluidic Systems

The Navier-Stokes equation for incompressible fluid is written as:

$$\rho \left(\frac{\partial v}{\partial t} + (v.\nabla)v \right) = -\nabla p + \eta \nabla^2 v + \rho g + \rho_{el} E$$

[Eq. VI.1.1]

where ρ the density of the fluid, ρ_{el} its charge density, η its viscosity.

The left hand side is the derivative of the speed with respect to time $\frac{Dv(r(t),t)}{Dt} = \frac{\partial v}{\partial t} + (v.\nabla)v$; and the right hand side of the equation shows the sum of all considered forces, the hydraulic force ∇p, the viscous force $\eta \nabla^2 v$, the gravity ρg and the electrical force $\rho_{el}E$.

The dimensionless Navier-Stokes equation is written as:

$$\frac{\partial v^*}{\partial t^*} + (v^*.\nabla^*)v^* - \frac{\eta}{\rho V_0 L_0}\nabla^{*2}v^* = -\nabla^*p^* + g^* + (\rho_{el}E)^*$$

[Eq. VI.1.2]

where V_0 and L_0 are the characteristic velocity and length of the system.

The Reynolds number is defined as:

$$Re = \frac{\rho V_0 L_0}{\eta}$$

[Eq. VI.1.3]

For systems where $Re \ll 1$, then the viscous term $\nabla^{*2}v^*$ dominates, while for systems with $Re \gg 1$, the inertia term dominates $(v^*.\nabla^*)v^*$. In general, the flow in a microfluidic system is in low Reynolds number regime.

For a fiber-template device, the velocity characteristic is calculate as $V_0 = \Phi/S$, where Φ is the flow rate of unity $[\Phi] = [m^3/s]$, S the section area, with the flow rate of $1\ mL/h$ and a section of $1\ mm^2$, the characteristic velocity is $10^{-5}\ m/s$; the characteristic length is around $1\ cm$; with viscosity of water at 25^oC is $8.9\,.\,10^{-4}Pa.s$ and its density is $10^3 kg/m^3$, the Reynolds number of our system is around 10^{-2}, which satisfies the condition $Re \ll 1$. In consequence, the flow in our system can be considered in laminar regime, where the viscous term is the dominant force compared to inertia term.

At low Reynolds number, $Re \ll 1$, the equation [VI.1.2] becomes a linear differential equation, which can be solved analytically in relatively simple manners. In particular, the behavior of the fluids in microfluidic systems can be predicted because the flow is laminar, which is one of the reasons that makes microfluidics attractive.

On the other hand, laminar flow also represents a fundamental challenge for mixing in microfluidic systems, because only diffusion contributes to mixing while convection, which comes the non-linear part of the equation, is excluded. The diffusive mixing is a slow process, and the diffusion time for a pure diffusion mixing exceeds considerably the operating time of the device

[70,71]. Numerous approaches to decrease the mixing time has been proposed, for example by increasing the fluid interfaces [72] or introducing active mixers [73] or even creating turbulent flow and transverse flow across the channels [74][75]. These approaches rely either on new designs of the channels, that can only be achieved with adding further complexity and equipment to the fabrication process.

1.2.2 Mixing enhancement based on Twisted systems

Here we introduce a novel mixing approach based on the fiber-template fabrication of twisted channels. Experimental results, shown in Figure VI.1.5 and VI.1.6 demonstrated a good mixing of high viscosity liquids in single-twist and multiple-twist devices. In a typical experiment, two fluids were introduced into a main channel through a T-junction, and exhibited laminar flow from the beginning of the of the main channel (Figure VI.1.5 (a)) to right before the twist (Figure VI.1.5 (b)). At the position around the twist, geometry constraints would create turbulence or transvers flow that enhance the mixing effect. After the twist, image VI.1.5 (c) shows a good mixing of two initial fluids, that continued to the output (Figure VI.1.5 (d)). Further simulation and imaging of the fluid behavior at the level of twist will be presented in a future publication.

For fluids of higher viscosity (obtained by adding PEG solution into water), several twists
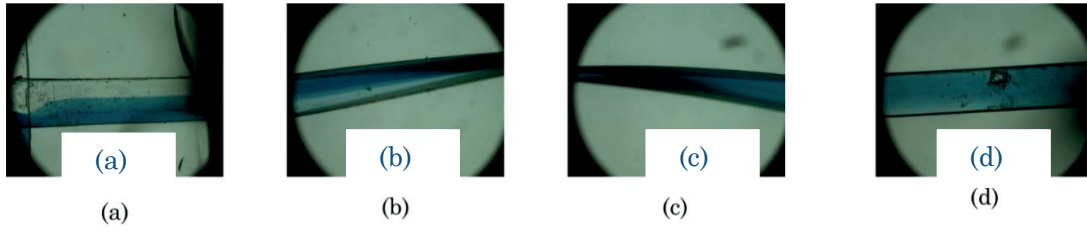
Figure VI.1.5: Images of fluid mixing in a single twist channel at different position (a) beginning of the channel, (b) right before the twist, (c) right after the twist, (d) near output.

could be made to enhance the mixing process. Images of flow near the output of a 3-twist channel are shown in Figure VI.1.6 (b-e), while the initial flow is shown in Figure VI.1.6 (a). The concentrations for each experiments corresponding to each images are (b) 10%wt of PEG in water, (c) 20%wt of PEG in water, (d) 30%wt of PEG in water, and (e) 40%wt of PEG in water, respectively.
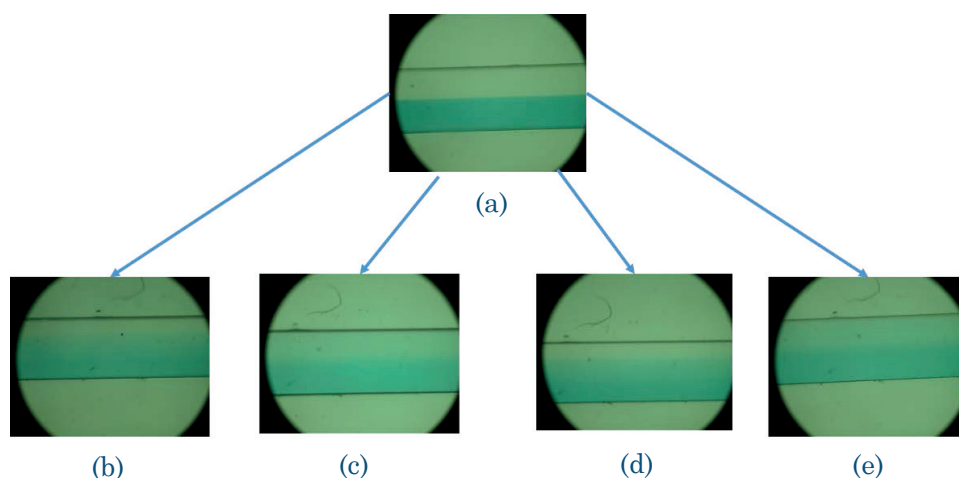
Figure VI.1.6: Images of mixing results of a 3-twist channel for PEG-water solution of different concentrations. (a) initial flow, (b) 20%wt PEG-water, (c) 20%wt, (d) 30%wt and (e) 40%wt.

The twisted channels clearly show an encouraging mixing enhancement features. A quantitative correlation of the level of mixture and the viscosity and diffusivity of fluids are expected in the future work on this project.

1.3   Summary and Perspectives

The fiber-template fabrication technique for microfluidic systems was introduced as an advanced assembly for thermally drawn fibers. It is utilized to create complex structures, both in 2D planar or in 3D configuration. The in-PDMS channels inherits directly the wide range of shapes and sizes of textured fibers developed in Chapter III and IV. We demonstrate a mixing enhancement device based on a low-cost and straight-forward fabrication process, as an example of the opportunities that this novel technique could bring. This work lays the ground for further developments of fiber-based fabrication technique, both on fundamental understanding of fluid behavior in textured and twisted channels, and on extending the scope of applications for the technique.

Furthermore, the use of multimaterial fibers besides the fiber-template microfluidic networks would add supplementary features such as local heating or electrophoresis sorting. These active microfluidic devices would enable the real time monitor and control of droplets and of continuous flow inside microfluidic channels. The developments of microfluidic devices based on multifunctional multimaterial fibers would indeed pave the way for promising supplementary approaches to address current limitations of soft-lithography based technique.

2. Multimaterial Fibers as Feeding Material for Filament Deposition Modeling Process

Conventional additive manufacturing technologies (AMs), commonly known as 3D printing, have attracted an increasing interest in a wide range of applications because of their efficiency and versatility. For instance, AMs have been employed for fast prototype fabrication from simple tools to airplane parts, or even in jewelry [76].

From the materials science perspective, the functionality of a 3D printed device comes solely from a structural assembly. It is true for radiation curable resin bath, metal powder bath, and filament deposition modeling. The feeding building block does not bring active functionality except offering bulk mechanical properties and adhesion as well as the specific shape. In addition, printing multi-material structure from materials of disparate properties, like metals, insulators and semiconductors, would add enormous complexity of AM systems.

In this regards, thermally drawn fiber brings a promising solution. Microstructured multimaterial fibers can indeed be designed to integrate a given functionality and separated domains that can insure adhesion to other similar fibers. By decoupling a functional domain and an assembling domain in a single fiber, one can create fiber-based constructs with complex features and nanoscale architectures. To implement this idea, we consider the filament deposition modeling (FDM), which stands out as one of the simplest and most relevant technique for our purpose.

Figure VI.2.1 shows the working mechanism of the FDM technique. A filament made of polymers is inserted into an oven by an extruder. Inside the oven, the filament is heated up to a molten state where its viscosity decreases significantly before being extruded out of the oven through a nozzle with shape and size that are precisely designed. This part of the machine is similar to an extruder. The molten polymer is deposited either directly on the substrate or on a heated bed or on previously deposited layers. The bonding of such molten polymers and its substrate is created through inter-diffusion of polymer chains at the interface. The nozzle and the feeding systems are positioned by a robotic system that can move precisely in three dimensions, gives the technique its common name "3D printing". In particular, the z-direction is sliced into planes, separated by a distance equal to the size of the extruded fiber, while the nozzle prints on each plan by moving in xy-direction.
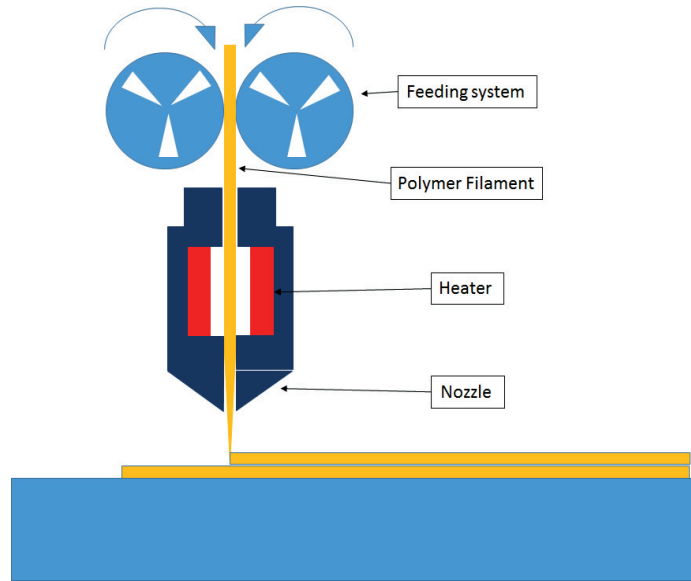
Figure VI.2.1: Schematic of a filament deposition modeling process, where a polymer filament is fed into a heater and extruded onto a substrate.

In this work, we demonstrate as a proof-of-concept a fiber composed of two distinguish parts: a capacitive touch-sensing architecture as well as a passive element for assembling. The fiber structure is described in the next section 2.1, and the assembly technique based on isothermal welding is introduced in section 2.2. Using this simple technique, which imitates loosely the assembly mechanism of a FDM process, a flexible touch sensing panel was created. Finally, we discuss future works that could consolidate the place of functional fibers in the dynamic development of additive manufacturing. This work is the subject of a manuscript that would be submitted in 2017.

2.1   Fiber Designs and Surface Assembling based on Isothermal Welding

The capacitive touch sensing technology is the most common in electronics nowadays, thanks to the popularity of touch screen in phones, TV, laptop etc. The mechanism of this technology is simply illustrated schematically in VI.2.1 (b): a single device consists of two electrodes and connects to a voltage source; when an electrical conducting material probe, for instance a human finger, approaches the device surface, it would interfere with the electrical field between the two electrodes, hence change the effective capacitance of the system. As a consequence, only by measuring the capacitance of the device, one could detect the touch.

With this simple mechanism, a fiber with two conducting plates along its length was made. Figure VI.2.2 (a) show the schematic of such a fiber and its cross-section. The conductive electrodes were made of cPC (black) and SnZn (grey), and the cladding material was PSu (brown). We employed two different materials as the electrodes because the composite allowed a large area electrode, while the metal increases the effective conductivity. This cross-sectional architecture was the same along the length of the fibers, which extended to hundreds of meters. A segment of around 50 *cm* was cut and two electronic contacts were added following the protocol established by Sorin in [63]. The capacitance of the fiber device was measured with a multimeter (Keysight U1733C). A clear increase of capacitance was observed with the fiber touch and without touch all along the fiber, as illustrated in Figure VI.2.2 (c). The change was more remarkable with the increase of the touch contact area. The device hence can detect a touch from a conductive surface, a finger in our case.

(a) (b) (c)
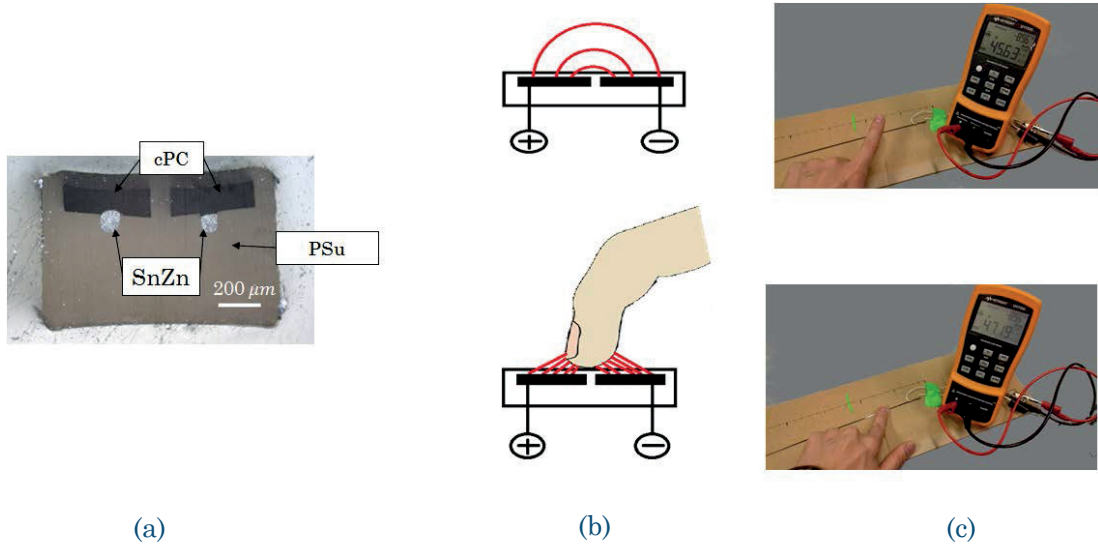
Figure VI.2.2: (a) an optical image of the cross-section of the 1st-generation capacitive touch-sensing (b) the electrical field (in red) between two electrodes when applied a voltage, the field is interfed when a conducting material, here a finger, touches the fiber surface. (c) a touch-sensing device of which the capacity change from 45 pF to 47 pF with the presence of a touch.

2.2   Assembly of Fiber using Thermal Welding

A capacitive touch-sensing fiber device could detect and in principle localize the touch, similarly to the MEMF device presented previously. However, here we exploited the use of a 2D panel to localize the touch. Such a panel was composed of a grid of the capacitive touch-sensing

fibers, illustrated in Figure VI.2.3 (a). When a conductive probe approaches the grid, it changed the capacity of two orthogonal fibers, one in the x-direction and the other in the y-direction. From the signal recorded in both directions, the panel can locate the touch.

(a)
(b)

(c)

(d)
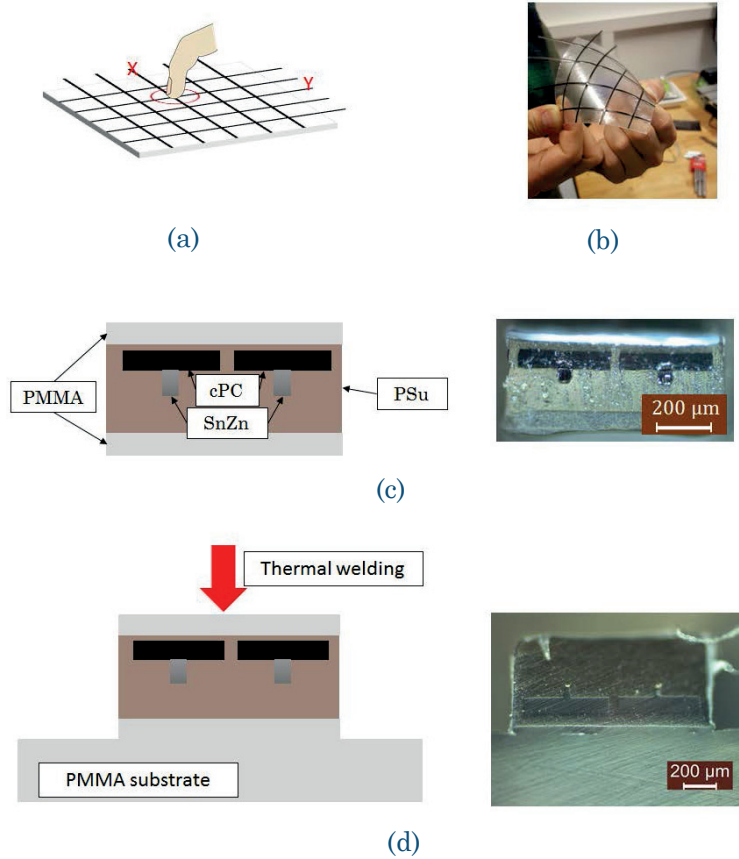
Figure VI.2.3: (a) schematic and image of the touch-sensing panel; (b) a flexible touch-sensing pannel made of the second generation touch-sensing fiber. (c) schematic and optical microscope image of the cross-section of the fiber, (d) schematic of the isothermal welding process of a second generation fiber on a PMMA substrate and a cross-sectional image of the interface obtained between the fiber and the substrate.

In order to utilize the AM technique for fiber assembly into functional panel, a second-generation touch-sensing fiber was fabricated, with additional elements dedicated to enable fiber-to-fiber assembly. These elements were made of a low T_g polymer compared to the T_g of the functional parts, in this instance, PMMA was used for a PSu cladding. Figure VI.2.3 (c) shows the schematic and optical microscopy image of the cross-section of this second-generation fiber. The PMMA elements were added both on top and bottom of the PSu functional structure. Here,

the assembly technique was substrate-assisted isothermal welding, illustrated in Figure VI.2.3 (d). A flexible film of PMMA was used as support, on to which the grid of fibers was welded at $120^{o}C$ in 30 minutes. After welding, we obtained a flexible panel with touch-sensing functionality. The different T_g of both polymers insure that the PMMA part could be wedded to the substrate while the functional part remained unaltered. This proof of concept shows that functional fibers with submicrometer feature sizes can be engineered to be assembled in larger 2D and 3D constructs. The assembling mechanism is the same as in conventional additive manufacturing systems., and further research will be done to use multimaterial fibers in AM processes.

2.3 Summary and Perspective

In this section, we introduced the notion of utilizing functional fibers for additive manufacturing, based on principle that the functionalization of a device could be decoupled from assembly process. A typical building-block filament consists of two distinctive parts, a functional core made and a polymer shell for assembly (see Figure VI.2.4). The fibers will be employed in an AD process in a temperature high enough to bond the outer shell on substrate, at the same time lower than the T_g or T_m of the materials in the functional core. As proof-of-concept, capacitive touch-sensing fibers were fabricated, with supplementary elements added to adapt with the AM process. With this architecture, we fabricated a flexible touch-sensing panel using isothermal welding. From these promising results multi-perspectives could be envisioned.

First, note that the functionalization of the fibers based on thermal drawing process was simple and low-cost, thanks to the scalability and efficiency of the technique. These fibers could easily be assembled using conventional techniques like weaving, which highlights once again the potential of thermal drawing technique for smart fabric and textile and for wearable electronics.

Regarding the development of thermally drawn fiber for AM process, and FDM in particular, further work will be done to address the main challenge of the FDM technique, which is the short welding time of the filament on the substrate before their interface cools down under the glass transition temperature. For example, materials and architecture of the fibers will need to be optimized for a typical non-isothermal welding in a FDM process. Nevertheless, the ultimate integration of multimaterial fibers into AM would offer a new way for a simple and inexpensive fabrication technique of complex 2D and 3D constructs.
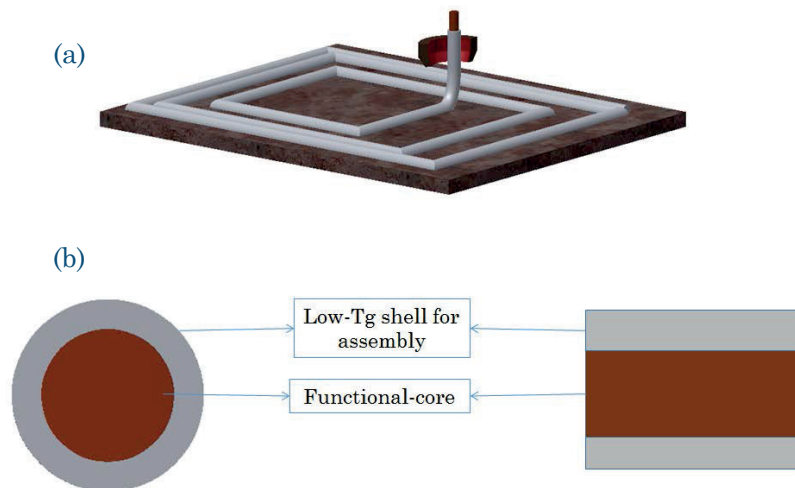

Figure VI.2.4: Schematic of a futuristic AM process using multimaterial functional fiber. (a) the printing of fiber on substrate; the red ring represents the heating nozzle. (b) the schematic of circular and rectangular fiber architectures for AM process.

Chapter VII.

Conclusion

The key contribution of this thesis is to establish the thermal drawing technique as a novel method for micro- and nano-patterning on large-area and flexible substrates, and within confined 3D hollow cavities. Beyond the simplicity and scalability of the fabrication process, we take advantages of its two distinguished and inter-dependent attributes, namely structure miniaturization and surface generation, to achieve unprecedented micro- and nano-scale structures over possibility kilometers of fiber length. The fiber surfaces' properties can be tuned depending on the feature-size of the physical pattern. To achieve such result, we identified the reflow of the structure driven by the surface tension of the textured polymer, as the main obstacle, and established a comprehensive theoretical description of the reflow behavior during the drawing process. This allowed us to propose a fundamental improvement in the preform fabrication and drawing process to dramatically reduce the surface/interface tension, hence to drastically diminish the reflow even with structures as small as 300 nm. We also outlined several applications that textured fibers could enable, especially in smart textiles, optics and bio-engineering.

The in-depth understanding of the reflow behavior provided us further insight on the drawing process, especially in the preservation of the cross-sectional geometry. In combination with the previous work on capillary break-up of structures, we established an empirical law that predicts the condition in which the cross-section shape could be maintained after undergoing the preform-to-fiber deformation. This law is based on a comparison between the processing time and the characteristic time constant associated with structure deformations. This simple approach could be a heuristic guide for future works involving the introduction of new materials or new architectures into fiber structures. As proof-of-concept, we verified this law on the drawing of preforms with freely movable domains into a new generation of micro electro-mechanical fibers for multipoint pressure-sensing with submillimeter resolution.

Finally, we presented two unconventional additive manufacturing techniques to exploit the potential of micro-textured and multimaterial fibers in microfluidic systems and in electronics.

The key feature is to decouple the functionality of the fiber-ink from the assembling step, which either simplifies the assembling procedure, or strengthens the functionalization of the assembled structure. The promising results of these two projects lay a strong foundation for further development of advanced additive manufacturing technique using functional multimaterial fiber.

Back to the Materials-Architecture-Processing diagram for thermal drawing introduced in Chapter I, I hope that this thesis contributes effectively to expand the fabrication capacity frontiers in the Architecture and Processing axis. We showed that sharp-edge, high-aspect ratio micro- and nano-scale structure could be simply made on the surface of thermally drawn fibers, and even on the internal surface of hollow core fibers. The application spectrum of these micro- and nano-textured fibers alone is broad, ranging from smart textile, optics, optoelectronics to biology and bio-engineering. Putting aside this work and others along the same line with the current stimulating development of the Materials axis, which allows more and more materials being incorporated in a single fiber, it is highly possible that the thermal drawing technique would be once again a main driving force behind a next technological revolution, the role it has already been playing in telecommunications.

A. Appendices

1. Surface Tension and Interfacial Tension of Polymers

1.1 Surface tension and surface energy:

The surface of a material is defined as the thin region in which the density, composition and energy vary continuously from air to the bulk material. The physical origin of the surface energy is the greater of cohesion interaction between molecules in bulk material compared to the adhesion interaction between the polymer molecules and air (Figure A.1.1).

As a consequence, a work is needed in order to create a unit surface area; this work is the quantitative measure of surface energy:

Figure A.1.1: Schematic of the creation of a surface.

$$\partial W = \gamma \, \partial S$$

[Eq. A.1.1]

This required work is also equal to the change of Gibbs free energy of the surface $\partial W = \partial G$. As the surface energy is positive, the polymer system in equilibrium tends to minimize its surface area to minimize the Gibbs free energy. At a curved surface, there is a drop of pressure from the bulk to air, perpendicularly across the surface, which is equal to the capillary pressure:

$$\Delta P = \gamma \, \kappa = \gamma \left(\frac{1}{R_1} + \frac{1}{R_2} \right)$$

[Eq. A.1.2]

where κ is the curvature of the surface, and R_1 and R_2 are the two principal radii of the curvature. This pressure drop is named Laplace pressure, after the French physicist Pierre-Simon Laplace who first gave the mathematical description of the phenomenon.
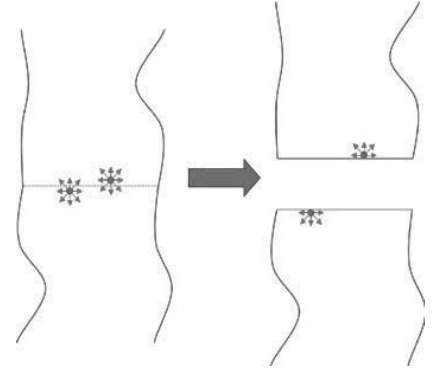
Under a constant pressure and volume condition, the general variations of the Gibbs free energy are given as $\partial G = -S\partial T$ with S the entropy of the surface. We define the specific surface energy and specific surface entropy as $G^s = \partial G/\partial A$ and $S^s = \partial S/\partial A$. Then the entropy for surface formation is given as:

$$S^s = -\frac{\partial\gamma}{\partial T}$$

[Eq. A.1.3]

The value of entropy is positive at any given temperature, hence the surface energy decreases when the temperature increases.

Note that there is a difference between surface energy and surface tension. Surface energy is defined above as the energy needed to create a unit of surface area, hence its dimension is energy per area [Joule/m^2]; while the surface tension relates to the force applied to a unit length of material surface [N/m]. This difference is obvious in the case of crystalline materials, where each direction of the crystalline structure has different surface tension, which eventually leads to non-spherical shape of the metal drop during a solidification process. However, in an isotropic material, such as amorphous polymers, or glass, or water, the value of its surface energy and surface tension are equal. In this thesis, only amorphous polymer is considered, hence we use uniquely the term surface tension and interface tension in our writing, but intentionally exchangeable with the concept of surface energy.

1.2 Contact Angle, Young Equation and Hydrophobicity

The surface tension determines the shape of a liquid drop on a solid surface through the contact angle θ (Figure A.1.2). The static contact angle is obtained when the droplet sits on the surface of a solid at equilibrium, and is given by the Young equation:

$$\gamma_{LV}\cos\theta_0 = \gamma_{SV} - \gamma_S$$

[Eq. A.1.4]

The equation is named after the British physicist Thomas Young, who first described the relation. The Young equation can be proven by considering the Gibbs free energy:

$$dG = \gamma_{LV}dA_{LV} + \gamma_{SV}dA_{SV} + \gamma_{SL}dA_{SL}$$

[Eq. A.1.5]

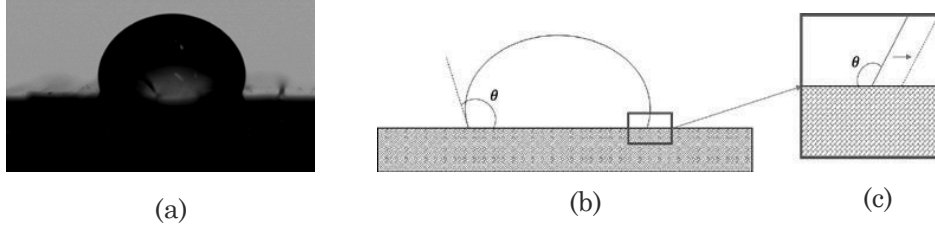<div align="center">(a)   (b)   (c)</div>

Figure A.1.2: (a) a water droplet on a surface of assembled fiber (b) a schematic of the cross-section view of such drop (c) the zoomed view of the solid-liquid-vapor interface.

At equilibrium, the variation of Gibbs free energy is null; and the advance of the liquid-solid area is created at the expense of the solid-vapor area: $dA_{SV} = -dA_{SL}$, at the same time, the increase of liquid-vapor area is given as: $dA_{LV} = \cos\theta_0 \ dA_{SL}$. The variation of Gibbs free energy is written as:

$$dG = 0 = (\gamma_{LV}\cos\theta_0 - \gamma_{SV} + \gamma_{SL})\,dA_{SL}$$

<div align="right">[Eq. A.1.6]</div>

Or

$$cos\theta_0 = \frac{\gamma_{SV} - \gamma_{SL}}{\gamma_{LV}}$$

<div align="right">[Eq. A.1.7]</div>

A hydrophobic surface is defined as a surface that repels water, i.e. the contact angle between water and the considered surface is higher than 90°; and a surface hydrophobicity enhancement is a treatment that increases the contact angles.

Due to roughness of the surface, however, the observed contact angle is different than the intrinsic contact angle θ_0. If we define r as the roughness factor (being the ratio of the real contact surface A to the projected apparent surface A', $r = \frac{A}{A'} > 1$) then the observed contact angle θ_r can be calculated from the Wenzel's equation:

$$\cos\theta_r = r\cos\theta_0$$

<div align="right">[Eq. A.1.8]</div>

From the equation above it is seen that an increase of roughness would lead to an increase of the contact angle, or an enhancement of surface hydrophobicity. In addition, in case of anisotropic roughness, such as a surface with an 1D pattern, the drop will exhibit as a consequence anisotropic contact angle.

1.3 Interfacial Tension between two Polymers

Although the direct measurement of the interfacial tension between two polymers is not available, several approaches can be employed to estimate this value.

The first common approach is based on the decomposition of the interaction at the interface into dispersive and polar interaction. The interfacial tension γ_{12} between two polymers of surface tension γ_1 and γ_2 respectively can be estimated using the following equation:

$$\gamma_{12} = \gamma_1 + \gamma_2 - 4\frac{\gamma_1^d \gamma_2^d}{\gamma_1^d + \gamma_2^d} - 4\frac{\gamma_1^p \gamma_2^p}{\gamma_1^p + \gamma_2^p}$$

[Eq. A.1.9]

with γ_i^d the dispersive component and γ_i^p the polar component [44]. In this equation, the interfacial tension of polymer with similar value of γ^d and γ^p would be much smaller than the surface tension of each component; for example, the interfacial tension of the pair PC/PMMA was estimated to be $2\frac{mN}{m}$.

Another way to estimate the interfacial tension is by taking into account the inter-diffusion across the interface, the interfacial tension between two immiscible polymers is calculate as:

$$\gamma_{ab} = \left(\frac{\chi}{6}\right)^{1/2} \rho_0 bkT$$

[Eq. A.1.10]

where ρ_0 is the number of monomers per unit volume, b the effective length per monomer unit, k the Boltzmann's constant, χ the Flory-Huggins interaction parameter; for instance, the value of interfacial tension of the pair PS/PMMA was estimated as $1\frac{mN}{m}$ at 140^oC using this approximation with $\chi = 0.01$, $b = 6.5\,\text{Å}$, $\rho_0 = 6.10^{27}\,cm^{-3}$ [77].

In general, these approaches could give simple guidelines for the selection of the second polymer for a system of two arbitrary immiscible polymers using value of each surface tension components for each material γ_i^d and γ_i^p or their interaction parameter.

2. Interface Strength Measurement

To measure the strength of the welded interface between cPE and PC, a cPE film was between two PC plates, and the sample was embossed by a hot-press (Thermal NanoImprinter EHN-3250) at temperature 150^oC and pressure $0.1\ MPa$. The mechanical strength was measured by a traction test (Mecmesin Multi-Test) to find the maximum force needed to separate the interface, which is defined in this study as the interface strength. Figure A.2.1 shows the samples and testing process for tensile and shear strength measurement. The result of this experiment is shown in Figure III.3.4 (b).
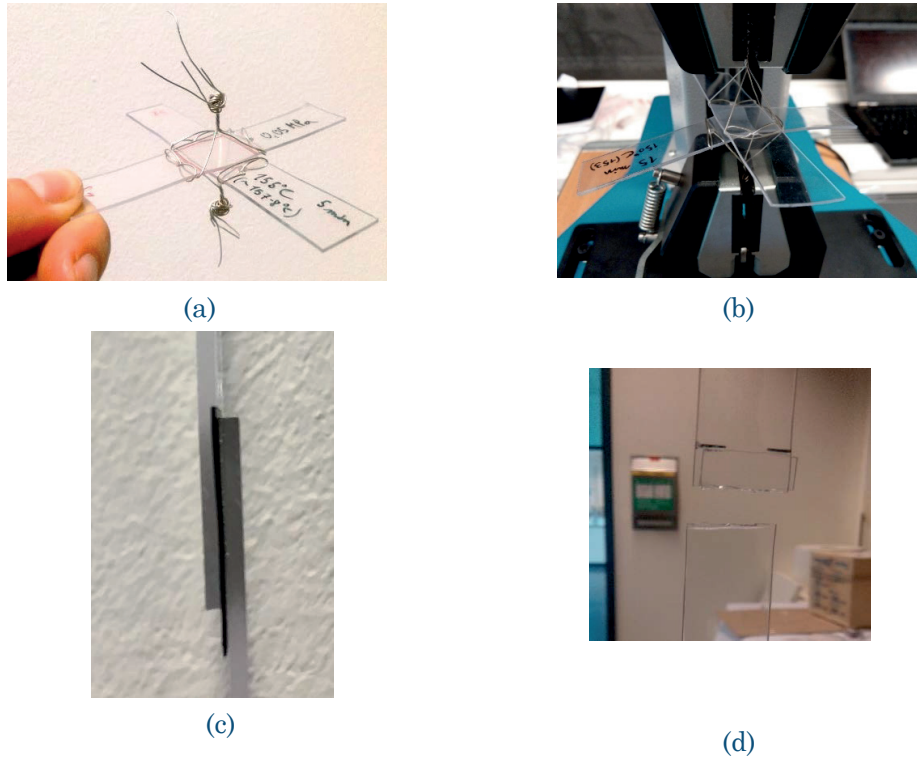

(a)

(b)

(c)

(d)

Figure A.2.1: Typical samples and tests for interface strength measurement. (a) and (b) tensile strength measurement; (c) and (d) shear strength measurement.

3. ASC Nucleus Grown on Patterned PC Fibers

Shape and orientation study of ASC nucleus grown on patterned PC fiber showed that Cell nuclei followed a similar trend as observed for the overall cell shape presented in section IV.3.3), being remarkably smaller (***p<0.001) on grooves in the range of $5 - 10\ \mu m$. Moreover, the larger the pattern, the more elongated were the nuclei, stretching along the groove direction. Bigger patterns ($5\ \mu m$ and $10\ \mu m$) resulted in more the nucleus was observed to "sit" inside grooves.
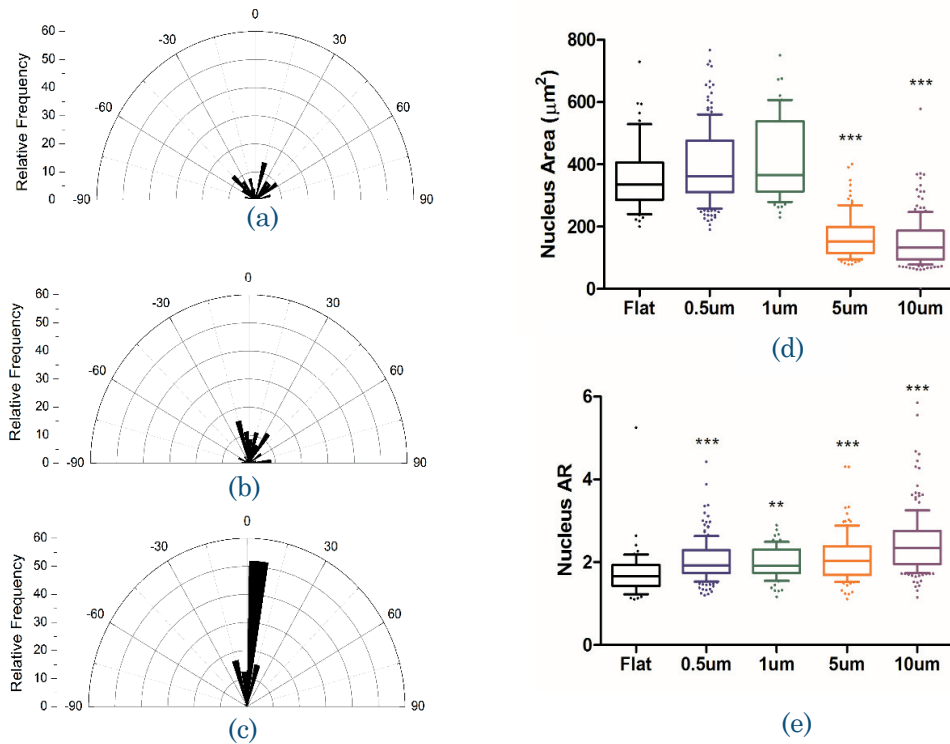

Figure A.3.1: Statistics of nuclei shape and orientation of cells grown on different fibers. (a) (b) (c) Relative frequency of nuclei orientation grown on flat fiber, $1\ \mu m$ patterned fiber and $10\ \mu m$ patterned fiber respectively. (d) (e) distribution of surface area and aspect-ratio of nuclei on fibers of different feature-size pattern.

B. Bibliography

[1] K. C. Kao, G. A. Hockham, *PROC. IEE.* **1966**, 1151.

[2] S. D. Personick, *IEEE J. Sel. Areas Commun.* **1983**, *1*, 373.

[3] Y. Koike, M. Asai, *Npg Asia Mater.* **2009**, *1*, 22.

[4] P. Russell, *Science* **2003**, *299*, 358.

[5] S. D. Hart, G. R. Maskaly, B. Temelkuran, P. H. Prideaux, J. D. Joannopoulos, Y. Fink, *Science* **2002**, *296*, 510.

[6] B. Temelkuran, S. D. Hart, G. Benoit, J. D. Joannopoulos, Y. Fink, *Nature* **2002**, *420*, 650.

[7] M. Bayindir, F. Sorin, A. Abouraddy, J. Viens, *Nature* **2004**, *431*.

[8] F. Sorin, O. Shapira, A. F. Abouraddy, M. Spencer, N. D. Orf, J. D. Joannopoulos, Y. Fink, *Nano Lett.* **2009**, *9*, 2630.

[9] F. Sorin, a. F. A. Abouraddy, N. Orf, O. Shapira, J. Viens, J. Arnold, J. D. Joannopoulos, Y. Fink, *Adv. Mater.* **2007**, *19*, 3872.

[10] M. Bayindir, A. F. Abouraddy, J. Arnold, J. D. Joannopoulos, Y. Fink, *Adv. Mater.* **2006**, *18*, 845.

[11] G. Lestoquoy, N. Chocat, Z. Wang, J. D. Joannopoulos, Y. Fink, *Appl. Phys. Lett.* **2013**, *102*, 152908.

[12] S. Egusa, Z. Wang, N. Chocat, Z. Ruff, *Nat. Mater.* **2010**.

[13] N. Chocat, G. Lestoquoy, Z. Wang, D. M. Rodgers, J. D. Joannopoulos, Y. Fink, *Adv. Mater.* **2012**, *24*, 5327.

[14] A. Gumennik, A. M. Stolyarov, B. R. Schell, C. Hou, G. Lestoquoy, F. Sorin, W. McDaniel, A. Rose, J. D. Joannopoulos, Y. Fink, *Adv. Mater.* **2012**, *24*, 6005.

[15] O. Shapira, K. Kuriki, N. D. Orf, A. F. Abouraddy, G. Benoit, J. F. Viens, A. Rodriguez, M. Ibanescu, J. D. Joannopoulos, Y. Fink, M. M. Brewster, *Opt. Express* **2006**, *14*, 3929.

[16] A. Stolyarov, L. Wei, O. Shapira, F. Sorin, *Nat. Photonics* **2012**, *6*, 229.

[17] J. F. Gu, S. Gorgutsa, M. Skorobogatiy, *Appl. Phys. Lett.* **2010**, *97*, 15.

[18] S. Gorgutsa, J. F. Gu, M. Skorobogatiy, *Smart Mater. Struct.* **2011**, *21*, 15010.

[19] R. He, T. D. Day, M. Krishnamurthi, J. R. Sparks, P. J. A. Sazio, V. Gopalan, J. V. Badding, *Adv. Mater.* **2013**, *25*, 1461.

[20] R. He, P. J. a. Sazio, A. C. Peacock, N. Healy, J. R. Sparks, M. Krishnamurthi, V. Gopalan, J. V. Badding, *Nat. Photonics* **2012**, *6*, 174.

[21] S. Danto, Z. Ruff, Z. Wang, J. D. Joannopoulos, Y. Fink, *Adv. Funct. Mater.* **2011**, *21*, 1095.

[22] F. Sorin, G. Lestoquoy, S. Danto, J. D. Joannopoulos, Y. Fink, *Opt. Express* **2010**, *18*, 24264.

[23] C. Hou, X. Jia, L. Wei, A. M. Stolyarov, O. Shapira, J. D. Joannopoulos, Y. Fink, *CLEO Sci. Innov. CLEO_SI 2013* **2013**, *1*, CTh1J.7.

[24] C. Hou, X. Jia, L. Wei, S.-C. Tan, X. Zhao, J. D. Joannopoulos, Y. Fink, *Nat. Commun.* **2015**, *6*, 6248.

[25] D. S. Deng, N. D. Orf, S. Danto, A. F. Abouraddy, J. D. Joannopoulos, Y. Fink, *Appl. Phys. Lett.* **2010**, *96*, 2010.

[26] S. Shabahang, J. J. Kaufman, D. S. Deng, A. F. Abouraddy, *Appl. Phys. Lett.* **2011**, *99.*

[27] D. Deng, J. Nave, X. Liang, *Opt. Express* **2011**, *19*, 219.

[28] J. J. Kaufman, G. Tao, S. Shabahang, E.-H. Banaei, D. S. Deng, X. Liang, S. G. Johnson, Y. Fink, A. F. Abouraddy, *Nature* **2012**, *487*, 463.

[29] T. Nguyen-Dang, A. C. de Luca, W. Yan, Y. Qu, A. G. Page, M. Volpi, T. Das Gupta, S. P. Lacour, F. Sorin, *Adv. Funct. Mater.* **2017**, 1605935.

[30] T. Nguyen-Dang, A. Page, Y. Qu, M. Volpi, W. Yan, F. Sorin, *J. Phys. D. Appl. Phys.* **2017**, *(in press).*

[31] N. Kooy, K. Mohamed, L. Pin, O. Guan, *Nanoscale Res. Lett.* **2014**, *9*, 320.

[32] A. Yildirim, M. Yunusa, F. E. Ozturk, M. Kanik, M. Bayindir, *Adv. Funct. Mater.* **2014**, *24*, 4569.

[33] R. A. Koppes, S. Park, T. Hood, X. Jia, N. Abdolrahim Poorheravi, A. H. Achyuta, Y. Fink, P. Anikeeva, *Biomaterials* **2016**, *81*, 27.

[34] A. F. Abouraddy, M. Bayindir, G. Benoit, *Nat. Mater.* **2007**, *6.*

[35] G. Tao, A. M. Stolyarov, A. F. Abouraddy, *Int. J. Appl. Glas. Sci.* **2012**, *3*, 349.

[36] S. Xue, R. Tanner, G. Barton, *J. Light. …* **2005**, *23*, 2255.

[37] S. Xue, R. Tanner, G. Barton, *J. Light. …* **2005**.

[38] U. C. Paek, R. B. Runk, *J. Appl. Phys.* **1978**, *49*, 4417.

[39] E. Pone, C. Dubois, N. Guo, Y. Gao, A. Dupuis, F. Boismenu, S. Lacroix, M. Skorobogatiy, *Opt. Express* **2006**, *14*, 557.

[40] H. M. Reeve, a. M. Mescher, a. F. Emery, *J. Heat Transfer* **2004**, *126*, 666.

[41] J. Teisseire, A. Revaux, M. Foresti, E. Barthel, *Appl. Phys. Lett.* **2011**, *98*, 13106.

[42] N. Sato, T. Yonehara, *Appl. Phys. Lett.* **1994**, *65*, 1924.

[43] H. Schift, C. Spreu, A. Schleunitz, J. Lee, *Microelectron. Eng.* **2011**, *88*, 87.

[44] S. Wu, *Polymer interface and adhesion*; Dekker, New York, 1982.

[45] S. Danto, F. Sorin, N. D. Orf, Z. Wang, S. A. Speakman, J. D. Joannopoulos, Y. Fink, *Adv. Mater.* **2010**, *22*, 4162.

[46]   M. Worgull, *Hot Embossing*; Elsevier, 2009.

[47]   R. D. Fields, J. M. Le Beau, F. M. Longo, M. H. Ellisman, *Prog. Neurobiol.* **1989**, *33*, 87.

[48]   L. H. Sperling, *Introduction to Physical Polymer Science*; John Wiley & Sons, Inc, 2006.

[49]   H. T. Pham, C. J. Carrierre, *Polym. Eng. Sci.* **1997**, *37*, 636.

[50]   G. Giancola, R. L. Lehman, J. D. Idol, *Powder Technol.* **2012**, *218*, 18.

[51]   B. L. Feng, S. H. Li, Y. S. Li, H. J. Li, L. J. Zhang, J. Zhai, Y. L. Song, B. Q. Liu, L. Jiang, L. Feng, S. H. Li, Y. S. Li, H. J. Li, L. J. Zhang, J. Zhai, Y. L. Song, B. Q. Liu, L. Jiang, D. B. Zhu, *Adv. Mater.* **2002**, *14*, 1857.

[52]   M. R. Lee, K. W. Kwon, H. Jung, H. N. Kim, K. Y. Suh, K. Kim, K. S. Kim, *Biomaterials* **2010**, *31*, 4360.

[53]   I. Tonazzini, E. Jacchetti, S. Meucci, F. Beltram, M. Cecchini, *Adv. Healthc. Mater.* **2015**, *4*, 1849.

[54]   M. Sun, M. McGowan, P. J. Kingham, G. Terenghi, S. Downes, *J. Mater. Sci. Mater. Med.* **2010**, *21*, 2765.

[55]   T. a Birks, J. C. Knight, P. S. Russell, D. M. Atkin, *Opt. Lett.* **1996**, *21*, 1547.

[56]   H. Lin, L. Li, F. Deng, C. Ni, S. Danto, J. D. Musgraves, K. Richardson, J. Hu, *Opt. Lett.* **2013**, *38*, 2779.

[57]   H. K. Tyagi, M. A. Schmidt, L. Prill Sempere, P. S. Russell, *Opt. Express* **2008**, *16*, 17227.

[58]   C. Markos, I. Kubat, O. Bang, *Sci. Rep.* **2014**, *4*, 6057.

[59]   E. Pone, C. Dubois, N. Guo, *Light. …* **2006**, *24*, 4991.

[60]   D. S. Deng, N. D. Orf, A. F. Abouraddy, A. M. Stolyarov, J. D. Joannopoulos, H. A. Stone, Y. Fink, *Nano Lett.* **2008**, *8*, 4265.

[61]   D. S. Deng, In-fiber Semiconductor Filament Arrays, Massachusett Institute of Technology, 2010.

[62]   J. Kaufman, G. Tao, S. Shabahang, D. Deng, *Nano Lett.* **2011**, 4768.

[63]   F. Sorin, A. F. Abouraddy, N. Orf, O. Shapira, J. Viens, J. Arnold, J. D. J. D. J. D. Joannopoulos, Y. Fink, *Adv. Mater.* **2007**, *19*, 3872.

[64]   V. Michaud, A. Mortensen, *Compos. - Part A Appl. Sci. Manuf.* **2001**, *32*, 981.

[65]   P. Yager, T. Edwards, E. Fu, K. Helton, K. Nelson, M. R. Tam, B. H. Weigl, *Nature* **2006**, *442*, 412.

[66]   S. Mondal, E. Hegarty, C. Martin, S. K. Gökçe, N. Ghorashian, A. Ben-Yakar, *Nat. Commun.* **2016**, *7*, 13023.

[67]   A. J. DeMello, *Nature* **2006**, *442*, 394.

[68]   G. M. Whitesides, *Nature* **2006**, *442*, 368.

[69]   Lee, Park, Whitesides, *Anal. Chem. Dc-* **2003**, *75*, 6544.

[70]   C.-Y. Lee, C.-L. Chang, Y.-N. Wang, L.-M. Fu, *Int. J. Mol. Sci.* **2011**, *12*, 3263.

[71]   Y. K. Suh, S. Kang, *Micromachines* **2010**, *1*, 82.

[72]   B. He, B. J. Burke, X. Zhang, R. Zhang, F. E. Regnier, *Anal. Chem.* **2001**, *73*, 1942.

[73]   K. Ahn, C. Kerbage, T. P. Hunt, R. M. Westervelt, D. R. Link, D. a. Weitz, *Appl. Phys. Lett.* **2006**, *88*, 1.

[74]   J. R. Votano, M. Parham, L. H. Hall, L. B. Kier, L. M. Hall, *Chem. Biodivers.* **2004**, *1*, 1829.

[75]   A. D. Stroock, S. K. W. Dertinger, A. Ajdari, I. Mezic, H. a Stone, G. M. Whitesides, *Science (80-.).* **2002**, *295*, 647.

[76]   I. Gibson, D. Rosen, B. Stucker, *Additive Manufacturing Technologies*; Springer, Ed.; 2th ed.; 2015.

[77]   E. Helfand, Y. Tagami, *Polym. Lett.* **1971**, *9*, 741.

C. Curriculum Vitae

Research and work experience

Dec 2012 – now	Ecole Polytechnique Fédérale de Lausanne, Lausanne, Switzerland. Laboratory of Photonic Fibers and Materials (FIMAP) of Prof. Fabien Sorin. Study on Micro- and Nano-fabrication by thermal drawing technique to create surface-patterned fiber and to deploy multimaterial fiber in microfluidics and in additive manufacturing.
Feb-Nov 2012	Saint-Gobain Glass, Aubervilliers, France International Technical Direction – Research Engineer. Study on the mechanism of debris generation in large-scale magnetron sputtering for a better understanding of debris-related phenomena. Result of the study led to the application of a new detecting system which increased the efficiency of several coater production lines in Europe.
Feb-Aug 2011	Saint-Gobain Research, Aubervilliers, France. Laboratoire Surface du Verre et Interfaces (SVI) – UMR 125 CNRS/Saint-Gobain National Institute for Materials Science, Ibaraki, Japan. Master thesis: "Defects in ZnO thin film prepared by DC sputtering". Study on the nanostructure of ZnO thin films sputtered on different substrates. The work was carried out in a collaborative program between Saint-Gobain and the National Institute for Materials Science of Japan (NIMS), with the fabrication of ZnO thin films at the Laboratory of Saint-Gobain in France and characterization performed in NIMS in Japan.
Apr-Aug 2010	Massachusetts Institute of Technology, Cambridge MA, United States of America. Photonic Bandgap Fibers and Devices Group of Prof. Yoel Fink. Bachelor thesis: "Distributed Multi-Material Fiber Sensors". Design of a one-dimensional sensing structure integrated within a multimaterial fiber. Demonstration of a laboratory prototype on glass substrate.

Education

2013 - now	Ecole Polytechnique Fédérale de Lausanne, Lausanne, Switzerland. PhD in Materials Science, Department of Materials Science, supervised by Prof. Fabien Sorin. Visiting student at MIT, spring term 2012-2013.
2011 - 2012	Master of Materials Science and Nano-Objects, Paris, France. Master program of the University of Paris VI Pierre and Marie Curie; jointly accredited with ENS, ESPCI and Ecole Polytechnique.
2007 - 2011	Ecole Polytechnique, Paris, France. Diploma of Engineer from the Ecole Polytechnique, specialization in Technological Innovation Visiting student at MIT, spring term of 2009-2010.
2002 - 2007	National University of Hanoi , Hanoi, Vietnam. High school and Preparation Program for Gifted students – Specialization in Physics.

Awards and Fellowships:

2011	Fellowship from NIMS Internship program
2010	Prize for the Best Report by the "Materials Science and Surface Active" program
2010	Internship Grant from the "Materials Science and Active Surface" program (chair X-ESPCI-Saint-Gobain
2007 - 2011	Eiffel Scholarship for excellent foreigner students
2004 - 2007	Odon Vallet Scholarship for excellent students
2003 - 2007	Prizes at the National Olympiad of Physics in four consecutive years

Language

English: Fluent.	French: Fluent.	Vietnamese: Native

Selected Publications:

- *Peer-reviewed papers:*
  - o "Controlled submicrometer hierarchical textures engineered in polymeric fibers and micro-channels via thermal drawing", <u>Tung Nguyen-Dang</u>, Fabien Sorin, et al., 2017, Advanced Functional Materials.
  - o "Multi-Material Micro-Electromechanical Fibers with Bendable Functional Domains", <u>Tung Nguyen-Dang</u>, Alexis Page, Fabien Sorin, *et al*, 2017, Journal of Physics D.
  - o "Thermal Reflow of Polymer Surface in Thermal Drawing Process", <u>Tung Nguyen-Dang</u>, Fabien Sorin *et al*, (in preparation)
  - o "Functional 2D and 3D construct via Multimaterial Fiber Additive Manufacturing", <u>Tung Nguyen-Dang</u>, Fabien Sorin *et al* (in preparation)
  - o "Novel fabrication method of large-scale, complex microfluidic devices from Multimaterial Fibers", <u>Tung Nguyen-Dang</u>, Fabien Sorin *et al*, (in preparation)
- *Conference:*
  - o "Recent development and perspective of multi-material optoelectronic fibers", <u>Tung Nguyen-Dang</u>, Wei Yan, Fabien Sorin, Progress in Electromagnetics Research Symposium (PIERS), Guangzhou, China, 2014.
  - o "Novel submicrometer patterning technique", <u>Tung Nguyen-Dang</u>, Fabien Sorin et al, EPFL Materials Science Day, Switzerland, 2015
  - o "Submicrometer patterning of curved surfaces via innovative viscous flow engineering", <u>Tung Nguyen-Dang</u>, Fabien Sorin et al, Junior-Euromat, Lausanne, Switzerland, 2016.
  - o "Multi-material Optical Fibers with Integrated Optoelectronic Devices" Wei Yan, <u>Tung Nguyen-Dang</u>, Fabien Sorin et al, Asia Communications and Photonics, Xi'an, China, 2016.
  - o "Novel Method for Micro/Nano Patterning using Fiber Thermal Drawing Technique", <u>Tung Nguyen-Dang</u>, Fabien Sorin et al, MRS Spring Meeting, Arizona, USA, 2017.
- *Patents*:
  - o "Multi-material stretchable optical, electronic and optoelectronic fibers and ribbons composites via thermal drawing", Patent application number P2993EP0P.
  - o "Novel fabrication method of micro/nano structure over large and flexible areas", Patent application number P2965EP0P.

Teaching experiments:

- "Introduction to Materials Science", Bachelor course, Teaching Assistant, language: French
- "Supervision of Research Project": since fall 2013 supervised 10 students for their semester research projects.

Scientific Expertise:

- **Material processing**: thin-film deposition techniques (thermal evaporation, magnetron sputtering, spin-coating), micro/nanotechnology (photolithography process, plasma etching, SU-8 processing, PDMS processing, nanoimprinting lithography), polymer processing (thermal drawing, extrusion, solution casting).
- **Material characterization**: electronic microscopy (SEM, TEM), optical microscopy, surface topography and chemical characterization (AFM, optical profiler, contact angle, XRD, XPS, SIMS), bulk properties (DSC, rheometer, ellipsometer).
- **Device characterization**: electronics (I-V, impedance spectroscopy), optics (integrating sphere, supercontinuum laser)
- **Simulation and Modelling**: good knowledge in Mathematica, COMSOL, Matlab and other languages such as Java, Python, Visual-Basic.

Personal Interests:

President of Dong-Hanh Association (2011-2012): managed a scholarship for students from disadvantaged background in Vietnam. Partner with the Foundation of France, Foundation Vallet, General Union of Vietnamese in France.

Sport: Fencing and Football; **Music**: Guitar and Harmonica (personal practice for 10 years).

Discover different work cultures over the world.